NASA/TM–20220017730

Reports from EXPORTS modeling and data-mining activities

Editors:
Ivona Cetinić and Inia Soto Ramos

Authors:
Brandi J. McCarty, Amala Mahadevan, Patricia Matrai, Dennis J. McGillicuddy, Jr., Cecile S. Rousseaux, David Siegel, James H. Churnside, Yongxiang Hu, David Nicholson, Andrew F. Thompson, Melissa M. Omand, Adrian Martin, Mathieu Dever, Zachary K. Erickson, Alexis Johnson, Lionel Arteaga, Ivona Cetinić and Ken Buesseler

January 2023

NASA STI Program ... in Profile

Since its founding, NASA has been dedicated to the advancement of aeronautics and space science. The NASA scientific and technical information (STI) program plays a key part in helping NASA maintain this important role.

The NASA STI program operates under the auspices of the Agency Chief Information Officer. It collects, organizes, provides for archiving, and disseminates NASA's STI. The NASA STI program provides access to the NTRS Registered and its public interface, the NASA Technical Reports Server, thus providing one of the largest collections of aeronautical and space science STI in the world. Results are published in both non-NASA channels and by NASA in the NASA STI Report Series, which includes the following report types:

- TECHNICAL PUBLICATION. Reports of completed research or a major significant phase of research that present the results of NASA Programs and include extensive data or theoretical analysis. Includes compilations of significant scientific and technical data and information deemed to be of continuing reference value. NASA counterpart of peer-reviewed formal professional papers but has less stringent limitations on manuscript length and extent of graphic presentations.

- TECHNICAL MEMORANDUM. Scientific and technical findings that are preliminary or of specialized interest, e.g., quick release reports, working papers, and bibliographies that contain minimal annotation. Does not contain extensive analysis.

- CONTRACTOR REPORT. Scientific and technical findings by NASA-sponsored contractors and grantees.

- CONFERENCE PUBLICATION. Collected papers from scientific and technical conferences, symposia, seminars, or other meetings sponsored or co-sponsored by NASA.

- SPECIAL PUBLICATION. Scientific, technical, or historical information from NASA programs, projects, and missions, often concerned with subjects having substantial public interest.

- TECHNICAL TRANSLATION. English-language translations of foreign scientific and technical material pertinent to NASA's mission.

Specialized services also include organizing and publishing research results, distributing specialized research announcements and feeds, providing information desk and personal search support, and enabling data exchange services.

For more information about the NASA STI program, see the following:

- Access the NASA STI program home page at http://www.sti.nasa.gov

- E-mail your question to help@sti.nasa.gov

- Phone the NASA STI Information Desk at 757-864-9658

- Write to:
  NASA STI Information Desk
  Mail Stop 148
  NASA Langley Research Center
  Hampton, VA 23681-2199

NASA/TM–20220017730

Reports from EXPORTS modeling and data-mining activities

Editors:
Ivona Cetinić
GESTAR II/Morgan State University, Baltimore, Maryland
Inia Soto Ramos
GESTAR II/ Morgan State University, Baltimore, Maryland

Authors:
Brandi J. McCarty, NOAA Chemical Sciences Laboratory, Boulder, CO
Amala Mahadevan, Woods Hole Oceanographic Institution, Woods Hole, MA
Patricia Matrai, Bigelow Laboratory for Ocean Sciences, East Boothbay, ME
Dennis J. McGillicuddy, Jr., Woods Hole Oceanographic Institution, Woods Hole, MA
Cecile S. Rousseaux, NASA Goddard Space Flight Center, Greenbelt, MD
David Siegel, University of California – Santa Barbara, Santa Barbara, CA
James H. Churnside, Cooperative Institute for Research in Environmental Sciences (CIRES), University of Colorado and NOAA Chemical Sciences Laboratory, Boulder, CO
Yongxiang Hu, NASA Langley Research Center, Hampton, VA
David Nicholson, Woods Hole Oceanographic Institution, Woods Hole, MA
Andrew F. Thompson, California Institute of Technology, Pasadena, CA
Melissa M. Omand, University of Rhode Island, Narragansett, RI
Adrian Martin, National Oceanography Centre, Southampton, UK
Mathieu Dever, Woods Hole Oceanographic Institution, Woods Hole, MA
Zachary K. Erickson, NOAA/Pacific Marine Environmental Laboratory, Seattle, WA
Alexis Johnson, University of Rhode Island, Narragansett, RI,
Lionel Arteaga, University of Maryland Baltimore County, Baltimore, MD
Ivona Cetinić, GESTAR II/Morgan State University, Baltimore, MD
Ken Buesseler, Woods Hole Oceanographic Institution, Woods Hole, MA

National Aeronautics and
Space Administration

Goddard Space Flight Center
Greenbelt, Maryland 20771

January 2023

Level of Review: This material has been technically reviewed by technical management.

Table of Contents

Introduction

EXPORTS -EXport Processes in the Ocean from RemoTe Sensing is NASA's large field campaign focusing on development of a predictive understanding of the export, fate and carbon cycle impacts of the global net primary production. This co-funded program (NSF, private funding[1], and international participation) was conceived in 2013, with EXPORTS Science plan published in 2016 (Siegel et al 2016, EXPORTS Writing Team 2015) and its implementation plan finalized in 2016 (EXPORTS Science Definition Team 2016). More details are presented in Siegel et al (2021).

EXPORTS campaign is structured as a multiyear effort (Figure 1). It started with "Pre-EXPORTS" modeling and data-mining activity followed by a first phase with two major field programs and a second synthesis and modeling phase. The "Pre-EXPORTS" projects, total of 6 of them (Table 1), funded under A.3 Ocean Biology and Biogeochemistry 2015 call, helped to plan the field campaign (Resplandy et al 2019, Rousseaux & Gregg 2017), and supporting further global synthesis with datasets mined from the literature (e.g. Bisson et al (2020), Bisson et al (2018), Kramer and Siegel (2019)), directly responding to objectives outlined in Science Plan (see section 6 in Team (2015)) and Implementation team (see Figure 1 in Team (2016)).

This document presents a compilation of the final reports of the Pre-EXPORTS funded projects, in hope of synthesizing the outcomes, and insuring the legacy of this program. Each of these reports contains a list of published papers, and reader should refer to them to see results in details.

Figure 1. Timeline for the NASA EXPORTS Field Campaign. Original NASA time line for the EXPORTS Field Campaign before postponement of the 2020 North Atlantic cruise due to the COVID-19 pandemic. The three boxes arranged vertically illustrate the planning, development and funding period (upper green), the Phase 1 field program (middle tan), and the planned Phase 2 data synthesis and modeling program (bottom blue). Taken from Siegel et al (2021). DOI: https://doi.org/10.1525/elementa.2020.00107.f4

[1] Twilight Zone project-https://twilightzone.whoi.edu/

Table 1. Pre-EXPORTS science team

Principal investigators	Project title
Churnside (NOAA)	Lidar data mining in support of EXPORTS
Mahadevan (WHOI), Nicholson (WHOI), Omand (URI)	Modeling studies for EXPORTS in a Dynamic Ocean Environment
McGillicuddy (WHOI), Lévy (Laboratoire d'Océanologie et de Climatologie), Resplandy (Princeton)	Mechanisms Controlling Mesoscale / Submesoscale Hotspots in Net Community Production/Export, with Simulation-Based Studies on how to Sample Them
Rousseaux (USRA/NASA GSFC), Cetinić (USRA/NASA GSFC), Gregg (NASA GSFC), Romanou (NASA GISS)	Observation-System Simulation Experiments (OSSEs) and Seasonal Forecasts to Support EXPORTS
Siegel (UCSB), Buesseler (WHOI)	Data Mining Global Ocean Ecosystem & Carbon Cycling Observations for EXPORTS Planning & Synthesis

References

Bisson K, Siegel DA, DeVries T. 2020. Diagnosing Mechanisms of Ocean Carbon Export in a Satellite-Based Food Web Model. *Frontiers in Marine Science* 7

Bisson KM, Siegel DA, DeVries T, Cael BB, Buesseler KO. 2018. How Data Set Characteristics Influence Ocean Carbon Export Models. *Global Biogeochem. Cycles* 32: 1312-28

Kramer SJ, Siegel DA. 2019. How Can Phytoplankton Pigments Be Best Used to Characterize Surface Ocean Phytoplankton Groups for Ocean Color Remote Sensing Algorithms? *Journal of Geophysical Research: Oceans* 124: 7557-74

Resplandy L, Lévy M, McGillicuddy Jr. DJ. 2019. Effects of Eddy-Driven Subduction on Ocean Biological Carbon Pump. *Global Biogeochem. Cycles* 33: 1071-84

Rousseaux CS, Gregg WW. 2017. Forecasting Ocean Chlorophyll in the Equatorial Pacific. *Frontiers in Marine Science* 4

Siegel DA, Buesseler KO, Behrenfeld MJ, Benitez-Nelson CR, Boss E, et al. 2016. Prediction of the Export and Fate of Global Ocean Net Primary Production: The EXPORTS Science Plan. *Frontiers in Marine Science* 3

Siegel DA, Cetinić I, Graff JR, Lee CM, Nelson N, et al. 2021. An operational overview of the EXport Processes in the Ocean from RemoTe Sensing (EXPORTS) Northeast Pacific field deployment. *Elementa: Science of the Anthropocene* 9

EXPORTS Science Definition Team. 2016. EXPORTS Implementation Plan

EXPORTS Writing Team. 2015. EXport Processes in the Ocean from RemoTe Sensing (EXPORTS): A Science Plan for a NASA Field Campaign

Lidar Data Mining in Support of EXPORTS – Final Report
NNH15ZDA001N

Brandi J. McCarty

University of Colorado Cooperative Institute for Research in Environmental Sciences (CIRES) at the NOAA Earth System Research Laboratory (ESRL) Chemical Sciences Division

James H. Churnside
NOAA Earth System Research Laboratory (ESRL) Chemical Sciences Division

Yongxiang Hu
NASA Langley Research Center

Abstract: The overall objective of this project was to investigate the usefulness of lidar as a remote sensing technique to support EXPORTS objectives. The emphasis was on the measurement of profiles of particulate backscattering coefficient, b_{bp}. Lidar is able to detect subsurface phytoplankton layers that are not detected by ocean color remote sensing. The investigation used three different lidars (the satellite lidar CALIOP, the NOAA airborne lidar, and the NASA airborne lidar) at five different geographical locations (Ocean Station Papa (OSP), the region around the North Atlantic Bloom Experiment (NABE), A Long-Term Oligotrophic Habitat Assessment (ALOHA) location at 23 N, the mid-latitude western Atlantic (SABOR), and the Arctic). CALIOP can detect subsurface layers under ideal conditions (clear water, deep layers), but not reliably enough to track an annual cycle, for example. The reasons are the poor depth resolution (22.5 m in water) of the sampling and the long detector fall time. CALIOP can provide surface values of the particulate backscattering coefficient, b_{bp} that compare well with MODIS estimates with values of the correlation coefficient, R, of 0.74 at OSP, 0.41 at ALOHA, 0.81 at NABE, and 0.1 in the Arctic. On the other hand, the NOAA airborne lidar can reliably detect subsurface layers about half the time in open water in the US Arctic. The prevalence decreased exponentially with increasing ice cover. The mean depth was around 20 m. The NASA airborne lidar uses a self-calibrating, high spectral resolution lidar (HSRL), that usesmost of the return energy for the calibration. The b_{bp} error with HSRL was around 5% near the surface. The error for the same SABOR data set without using the calibration channel was about 10%. A space-based oceanographic lidar would support studies like EXPORTS and monitor changes. The performance tradeoffs between HSRL and direct backscatter lidars have been quantified to aid in the design of such a lidar.

1. Introduction

EXport Processes in the Ocean from Remote Sensing (EXPORTS) is a large-scale NASA-led field campaign that will provide critical information for quantifying the export and fate of upper ocean net primary production (NPP) using satellite observations and state of the art ocean technologies. A conceptual diagram (Fig. 1.1) illustrates the complexity of interactions between the various components and the variety of platforms from which measurements will be made. It

is clear from the figure that depth-resolved measurements will be necessary to completely understand the export of carbon to the deep ocean. Current satellite instruments, however, are not designed to provide this information.

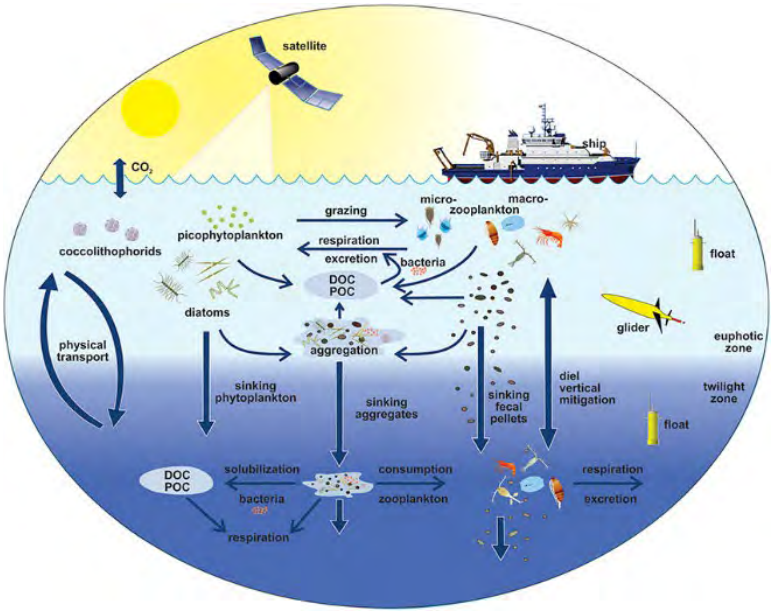

Figure 1.1. EXPORTS conceptual diagram illustrating the links among the ocean's biological pump and pelagic food web and our ability to sample these components from ships, satellites, and autonomous vehicles. Light blue waters are the euphotic zone (EZ), while the darker blue waters represent the twilight zone (TZ).

Lidar is a remote sensing technique that has the potential for depth resolved measurements from aircraft and spacecraft. The overall objective of this project was to compile a data set comprising lidar-derived profiles of inherent optical properties and the associated errors and uncertainties in the two regions described in the EXPORTS study plan. In addition, a similar data set was compiled for the Arctic and for a Pacific Ocean site at lower latitude, expanding the range of ecosystem states to these critical areas. In addition, we used the existing lidar data to investigate how reliably the inherent optical properties of the ocean can be measured with a space-based lidar.

For an unpolarized lidar with a broad beam, the signal can be expressed as (Churnside, 2008)

$$S(t) = A\beta(z)\exp\left(-2\int_0^z dz' K_d(z')z'\right), \tag{1.1}$$

where S is the lidar signal, t is time, A is a calibration coefficient that includes relevant lidar parameters (laser pulse energy, receiver telescope area, detector sensitivity, etc.), β is the volume scattering coefficient at the lidar scattering angle of π radians, z is the measurement depth, and K_d is the diffuse attenuation coefficient for the lidar incidence angle. With an appropriate inversion technique, this equation can be used to obtain depth profiles of β and K_d. Note that both of the

lidar parameters depend on the optical wavelength used. This proposal will consider data from three lidar systems, all of which operate at 532 nm and this wavelength will be assumed throughout.

The first parameter, β, is the sum of molecular and particulate contributions. The molecular contribution can be found from theoretical considerations and removed. The particulate contribution is the product of the particulate scattering coefficient, b_p, and the particulate phase function at the scattering angle of π radians. Petzold (Petzold, 1972) noticed that the particulate phase functions of waters with very different values of b_p were nearly the same. More recent studies have reached a similar conclusion, especially for scattering angles greater than 0.5π (Sullivan and Twardowski, 2009). The implication is that lidar profiles of β can be used to infer profiles of other inherent optical properties related to scattering, including b_p and the backscattering coefficient b_{bp}, which is the total particulate scattering at all angles greater than 0.5π. For example, published bio-optical models (Churnside, 2015) provide the relationship

$$\beta = 0.114 b_w + 0.151\left(b_b - \tfrac{1}{2} b_w\right), \tag{1.2}$$

where b_w is the scattering coefficient for pure sea water (2.22×10^{-3} m^{-1}) and b_b is the total backscattering coefficient. This proposal will determine the uncertainty in estimating these properties from lidar data.

Generally K_d is considered to be an apparent optical property rather than an inherent property, because it depends on the solar illumination angle. The attenuation measured by a broad-beam lidar does not depend on sun angle, of course, but has the same value as solar attenuation at the same incidence angle (Lee *et al.*, 2013). This parameter, essentially the attenuation of an infinite plane wave, can be considered to be an inherent optical property in the same way that beam attenuation, essentially the attenuation of an infinitesimally narrow beam, is considered an inherent optical property.

Since K_d includes contributions from absorption and scattering, it should be possible to retrieve absorption profiles from lidar data. The absorption from sea water has been precisely measured, so this component can be removed. The absorption from dissolved organic matter can be estimated if we can also remove the scattering component. From published bio-optical models (Churnside, 2015), we have

$$K_d = 1.054\left(a + b_b\right), \tag{1.3}$$

where a is the total absorption.

For polarization lidar, which is particularly effective at detecting layers (Churnside and Donaghay, 2009; Churnside and Marchbanks, 2015), there are two additional parameters (Churnside, 2008). The first is the depolarization coefficient for multiple forward scattering, and the other is the depolarization resulting from a single backscattering event. There are currently

no accepted bio-optical models for these parameters, but the data exist to develop them as part of the proposed work. Churnside (Churnside, 2008) found linear relationships between the two polarization parameters and the parameters for unpolarized lidar, K and $\beta(\pi)$, for which we have bio-optical models. This suggests that we can use these relationships to develop bio-optical models for the polarization parameters.

With the appropriate bio-optical model, it is possible to estimate profiles of chlorophyll concentration (Churnside, 2015; Churnside and Marchbanks, 2015; Churnside *et al.*, 2014) and primary productivity (Behrenfeld and Falkowski, 1997; Churnside and Marchbanks, 2015; Westberry *et al.*, 2008). That was beyond the scope of this project, but we will continue to work closely with Prof. Behrenfeld and his team at Oregon State University to ensure that the results of this work can be used in those studies.

2. CALIOP Data

2.1. Introduction

The Cloud-Aerosol LIdar with Orthogonal Polarization (CALIOP) is the primary instrument on the Cloud-Aerosol Lidar and Infrared Pathfinder Satellite Observations (CALIPSO) satellite. In 2006, the lidar began to measure profiles of aerosols and clouds in the atmosphere. It measures backscatter and depolarization at two wavelengths (1064 nm and 532 nm) with a vertical resolution of 30 m in the lower atmosphere. While it was designed for atmospheric measurements, there have been several investigations into the subsurface ocean return from the 532 nm channel (Churnside *et al.*, 2013; Lu *et al.*, 2014; Lu *et al.*, 2016). The 1064 nm channel only penetrates about 1 mm into seawater, and is not useful.

Two problems become evident when looking at the subsurface return from CALIOP. The first is the poor spatial resolution. A 30 m height resolution in air produces a 22.5 m depth resolution in seawater, and only about 10% of the incident light will survive a round trip pass through 22.5 m in the clearest waters. The second is problem is an artifact of the photomultipliers used to detect the 532 nm light. The signal does not go immediately to zero when the light on the photomultiplier goes to zero, but decays over time. This decay can be slower than the attenuation of light in water, so the signal is dominated by this artifact rather than subsurface scattering. This effect can be reduced by deconvolution (Lu *et al.*, 2014), but not entirely eliminated.

2.2. Materials and Methods

The CALIOP is one of three co-aligned nadir-viewing instruments aboard CALIPSO satellite. Selected calibrated and geolocated lidar profiles of total attenuated backscatter, β_{total}, and perpendicular attenuated backscatter, β_{perp} [km^{-1} sr^{-1}] were averaged spatially and temporally, where the CALIOP depolarization information is useful in bio-optical models.

Several criteria were considered, the first, limiting the lidar profiles to night time only. The CALIPSO team has divided the lidar data (by orbit) into day and night, where named files indicate start times, and also an extension, "ZN". Files with extension "ZD" are daytime files. The night time criteria removes consideration and removal of background signal in the data. Second, in order to ensure adequate signal at the surface and therefore subsurface, we specified a threshold value of 0.1 km^{-1} sr^{-1} on β_{surf}. A sufficiently large (maximum) signal at the surface indicates the atmosphere is free of cloud or aerosol contamination. Due to the non-ideal temporal response of the 532 nm detector, only bins where the surface is expected in β_{total} were inspected, including the last atmospheric bin, and three apparent subsurface bins.

As published in Data Quality Statement V1.10 Dec 2006, (https://www-calipso.larc.nasa.gov/resources/calipso_users_guide/data_summaries/CALIOP_transient_response.php), when a strong backscatter response from β_{total}, like the ocean surface, is observed, the CALIOP photo multiplier tubes exhibit a less than ideal recovery. This transient response, likely an afterpulsing artifact, is spread over several adjacent bins after observing a hard target, when a quick return back to zero is expected. Hunt *et al.* (2009) characterized the detector response using land surface return. Lu *et al.* (2014) extensively characterized the PMTs prior to launch, and demonstrated that surface reflectance from the ocean surface duplicate the response of land surface returns. Lu also pointed out that 90% of the surface return energy comes from the three 30 m vertical range bins (z_p, z_{p+1}, z_{p-1}) corresponding to the bin of peak return, as well as the one before and one after the peak return.

Locating the true surface signal using β_{total} is difficult due to the CALIOP non-ideal PMT response, but also tangled up with the satellite downlinking and data reduction processing. Onboard low pass filtering of the originating 15 m samples not only reduces the amount of data sampled and downlinked, but also has the effect that peak surface return is broadened to maintain the integral of, or area under, the pulse. The precise amplitude of the surface return is lost. The effective low pass smoothing of the signal makes the strength and the position in range of the β_{surf} difficult to discern.

Version 4, level 1b CALIOP β_{total} and β_{perp}, for the time period December 2008 – May 2017, were acquired through NASA's Earth Observing System Data and Information System, EOSDIS, using the CALIPSO subsetting tool (https://subset.larc.nasa.gov/calipso/login.php). Inspecting only data occurring over water surfaces (no land, coastal or shallow water profiles included) as identified using land/water mask provided in the level 1b data, a location and magnitude of β_{surf} was determined. Since the lidar is designed for atmospheric use, the range bins are labeled by their hight above the surface assuming a 30 m range resolution. We used five of those range bins, one in the atmosphere (22.8 m), one at the surface (-5.33 m) and two below the surface (-27.7 m and -50.1 m). For each set of five bins, the location and magnitude of the maximum β_{total} was found. If sufficient in magnitude, β_{surf} (greater than 0.1 km^{-1} sr^{-1} as in above

prescribed criteria), both the β_{total} and β_{perp} were shifted to vertically align the profiles, matching the strongest return (surface return) in the profiles to the -5.33 m bin.

Once the β_{total} and β_{perp} profiles were vertically aligned, a surface depolarization ratio, δ_{surf}, was calculated. A sea surface with no foam will produce a specular reflection with almost no depolarization, while foam on the surface will depolarize the reflected light. To remove these effects, only profiles identified with $\delta_{surf} < 0.01$ were included in the analysis, except at the deep-water Station ALOHA location, where a more stringent surface condition was imposed; only profiles where $\delta_{surf} < 0.005$ were included.

CALIOP β_{total} and β_{perp} profiles meeting all criteria were averaged to a 5° latitude by 5° longitude grid in space and monthly in time. Averaged vertical profiles from 52.7 m to -156.8 m ASL of β_{total} and β_{perp} from January 2008 – May 2017 were calculated. One final consideration in determining a more precise magnitude of CALIOP subsurface signal, comes back to the transient response of the PMT. Using the deconvolution technique employed by Lu *et al.* (Lu *et al.*, 2013; Lu *et al.*, 2014) and the receiver response profile obtained from Yongxiang Hu of the Climate Science Branch, NASA Langley Research Center, Hampton, VA, detector response corrected vertical profiles of β_{total} and β_{perp} were computed. This reduced and corrected CALIOP data set was used in further analysis.

The depolarization channels of the CALIOP permit detection of ocean signal. The perpendicular backscatter signal is due to the backscatter from particulate matter, while the total backscatter signal is dominated by the surface reflection. Using the CALIOP depolarization ratio and an estimate of β_{surf}, a column integrated β_{perp} was calculated (β_{w+}). Using these components, a diffuse attenuation coefficient, K_d, from passive sensors and equations in Behrenfeld *et al.* (2013), a hemispheric backscattering coefficient, b_{bp} ,was calculated.

Due to the subsampling of the CALIOP data prior to downlink, the precise magnitude of the total attenuated backscatter from the surface, β_{surf}, cannot be ascertained. Hu *et al.* (2008) demonstrated that ocean surface mean square wave slopes are inversely proportional to β_{surf}. Using mean wind speed, v, obtained from NCEP reanalysis products available at https://www.esrl.noaa.gov/psd/data/gridded/data.ncep.reanalysis.derived.surface.html monthly mean square wave slopes, $< s^2 >$ were computed using (Hu *et al.*, 2008)

$$\beta_s = \frac{0.0193}{4\pi \langle s^2 \rangle \cos^4 \theta} \exp\left[-\frac{\tan^2 \theta}{2\langle s^2 \rangle} \right], \tag{2.1}$$

where $<s^2> = 0.003 + 0.00512v$ (Cox and Munk, 1954; Hu *et al.*, 2008).

A column-integrated depolarization ratio, δ_T, was calculated using the CALIOP backscatter signals, β_{total} and β_{perp} by summing up backscatter signals from the apparent surface bin through three subsurface bins and taking the ratio, $\delta_T = \Sigma\beta_{perp} / \Sigma\beta_{total.}$ Armed with estimates of β_{surf} and

δ_T, the column integrated perpendicular backscatter, β_{w+} , was computed from (Behrenfeld *et al.*, 2013)

$$\beta_{w+} = \delta_T \frac{\beta_s}{1-\frac{\delta_T}{\delta_w}} \approx \delta_T \frac{\beta_s}{1-10\delta_T}. \quad (2.2)$$

where δ_w is the depolarization induced by scattering from pure seawater.

Data retrieved from https://oceancolor.gsfc.nasa.gov/cgi/l3 of the downwelling diffuse attenuation coefficient, K_d at 490 nm, provided values for determining particulate depolarization ratio, $\delta_{p,}$. Evaluating $K_{d,}$ scaled to 532 nm (Mobley, 1994), using two conditions, δ_p was found. $\delta_p = 0.1 + 2(K_d - 0.05)$ for water when $K_d < 0.15$ m^{-1} and $\delta_p = 0.3$ m^{-1} for $K_d > 0.15$, according to (Churnside, 2008). Finally, using estimates of $\beta_{surf,}$ $\beta_{w+,}$ K_d and δ_T, the hemispheric backscattering coefficient, b_{bp}, at 440 nm was calculated from (Behrenfeld *et al.*, 2013)

$$b_{bp}(440) = \frac{2K_d\beta_{w+}}{0.15\times 0.98^2}\frac{1+\delta_p}{\delta_p}\frac{532}{440}. \quad (2.3)$$

Note that this equation can be roughly approximated by

$$b_{bp}(440) \approx \frac{\beta_{w+}}{0.15\times 0.98^2}\frac{532}{440}, \quad (2.4)$$

so the errors in b_{bp} are dominated by the errors in β_{w+}, which, in turn, are dominated by errors in δ_T. The relative error in δ_T was estimated from the normalized standard deviation of $\Sigma\beta_{total}$ and $\Sigma\beta_{perp}$. The absolute value of the root-mean-square error (RMSE) in b_{bp} was then obtained by multiplying by the mean value in each case.

2.3 CALIOP Results

The particulate backscatter coefficient, $b_{bp,}$ [m^{-1}] is an indicator of the amount of suspended particles or matter in a water column. Using the 5° x 5° CALIOP estimates of column integrated depolarization ratio, δ_T, to compute column integrated perpendicular backscatter, β_{w+}, in Eq 2.2, b_{bp} was found using Eq 2.3 at four locations, Ocean Station Papa, deep water Station ALOHA (A Long-Term Oligotrophic Habitat Assessment), at the North Atlantic Bloom Experiment site, and the Arctic Ocean.

Retrievals of b_{bp}, using Generalized Inherent Optical Property, GIOP, models with measurements from the MODIS, Moderate Resolution Imaging Spectroradiometer, aboard NASA's Aqua and Terra satellites are available. The CALIPSO and Aqua satellites are both in the A-Train, crossing the equator in the afternoon, while Terra crosses in the morning. Both MODIS Aqua and MODIS Terra provided points to assess the CALIOP b_{bp} estimates. MODIS

particulate backscattering at 443 nm was acquired from https://oceancolor.gsfc.nasa.gov/cgi/l3 for both Aqua and Terra. Results for the period 2008 January to 2017 May are shown and discussed for each of the four locations.

2.3.1 Ocean Station Papa

Having one of the oldest data records (https://www.pmel.noaa.gov/ocs/Papa), the Ocean Station Papa surface mooring is important for research on ocean climate. This buoy is located in the Pacific Ocean at 50° N latitude and 145° W longitude, and has a monitoring radius of 1.25 km. Physical and biological properties are measured throughout the water column, it is an ideal northern latitude location for evaluating CALIOP determined ocean parameters. Figures 2.1 and 2.2 show the time series of b_{bp} as retrieved from satellite. The four lines represent b_{bp} as found using information from three instruments. The two black lines are b_{bp} as computed using CALIOP total and perpendicular attenuated backscatter and either MODIS Terra (Fig. 2.1) or MODIS Aqua (Fig. 2.2) diffuse attenuation coefficient, K_d. The different colored lines are b_{bp} from Terra and Aqua retrieved using the GIOP algorithm and the MODIS observations. A seasonal cycle is apparent with annual b_{bp} maxima in summer months and minima in winter months. The CALIOP estimated b_{bp} is within the uncertainty of the retrieved approximation.

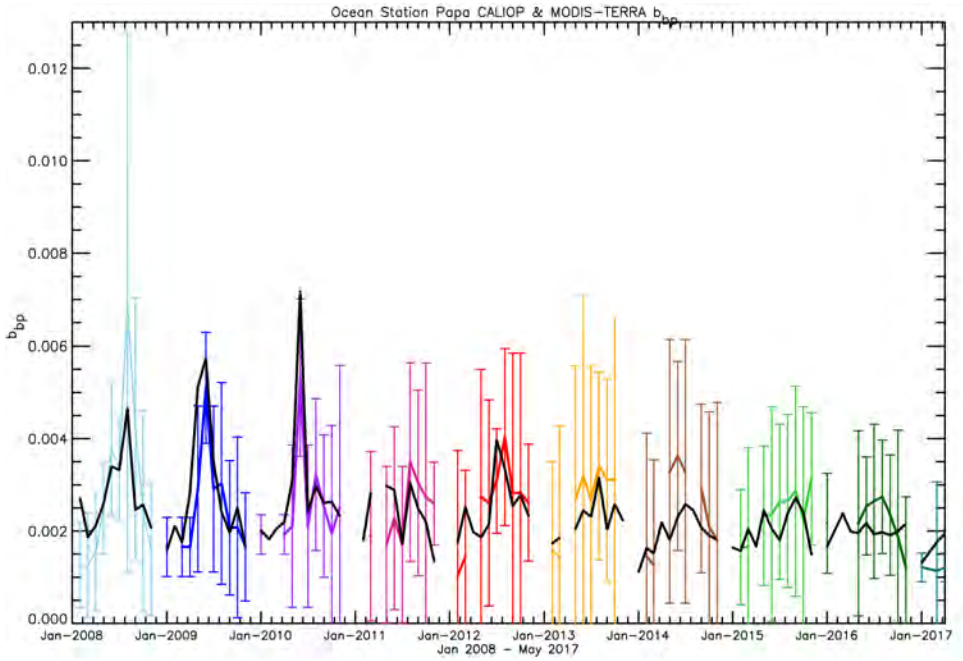

Figure 2.1 Particulate backscattering coefficient, b_{bp}, at Ocean Station Papa. CALIOP b_{bp} is retrieved using diffuse attenuation coefficient, K_d, from the MODIS measurements on Terra, black line, using Eq. 2.3. b_{bp} from the MODIS instrument are estimated using GIOP model retrievals, where MODIS Terra estimates are the colored lines with reported uncertainties. Each color represents a different year.

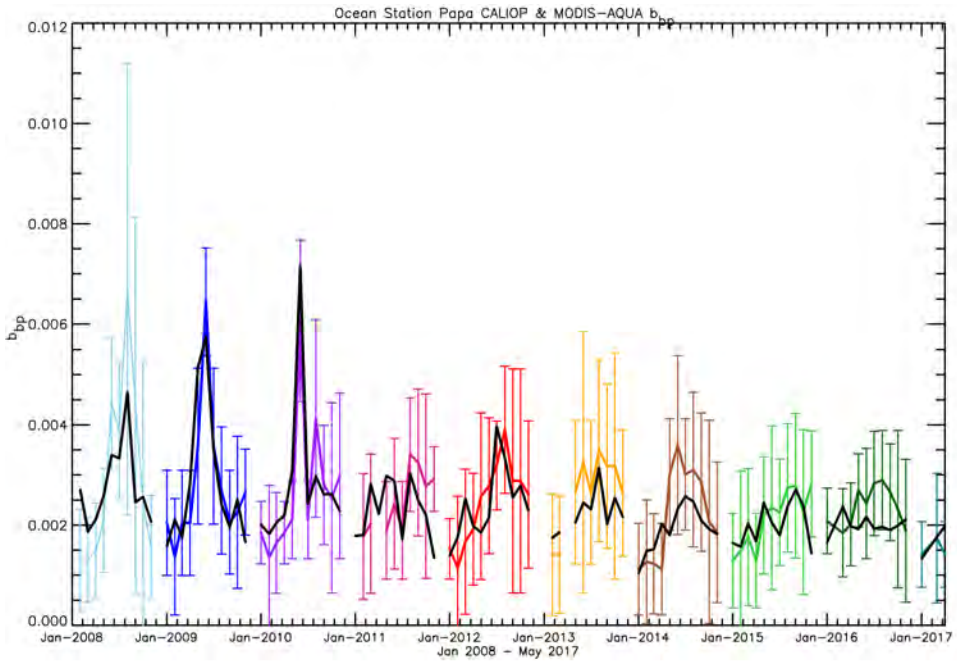

Figure 2.2 Particulate backscattering coefficient, b_{bp}, at Ocean Station Papa. CALIOP b_{bp} is retrieved using diffuse attenuation coefficient, K_d, from the MODIS measurements on Aqua, black line, using Eq. 2.3. b_{bp} from the MODIS instrument are estimated using GIOP model retrievals, where MODIS Aqua estimates are the colored lines with reported uncertainties. Each color represents a different year.

Using ordinary least squares (OLS) bisector regression, the satellite estimates of b_{bp} were compared. OLS bisector regression analysis was chosen as both the independent and dependent variables include measurement uncertainty (Isobe *et al.*, 1990). The scatterplots in Figures 2.3 and 2.4 show the MODIS estimates on the horizontal axis, and the CALIOP estimates on the vertical axis. Symbols are color coded by season, and the solid line shows the OLS-bisector fit. The seasonal color coding in the scatterplot of the b_{bp} data show that in winter (DJF) and spring (MAM) the CALIOP retrieved particulate backscatter coefficient is higher than other seasons. All points in winter, (DJF), are January and February; no December K_d data were available at this location.

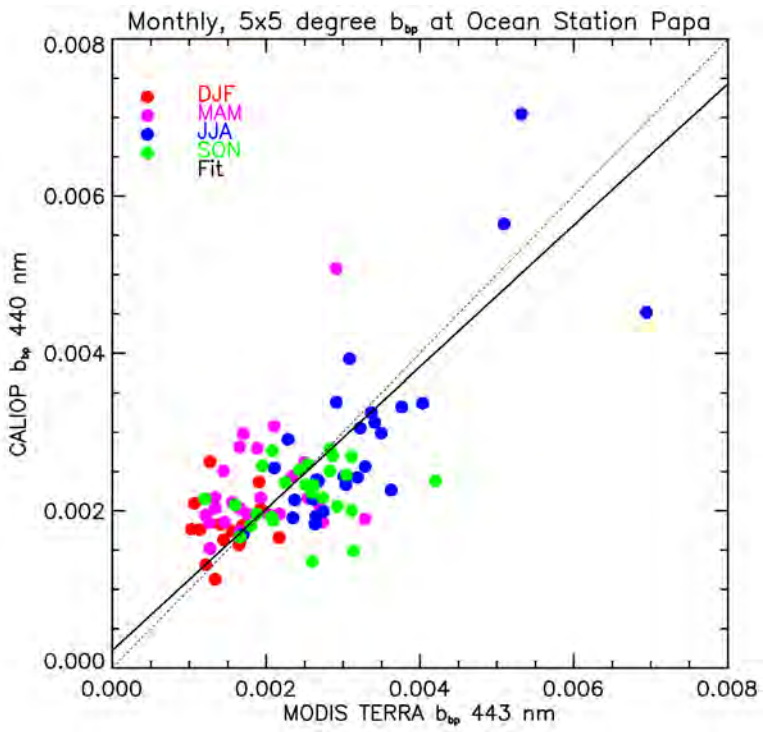

Figure 2.3 CALIOP estimated b_{bp} vs MODIS Terra model retrieved b_{bp}. Solid black line shows an OLS-bisector fit, while the dotted line is one-to-one.

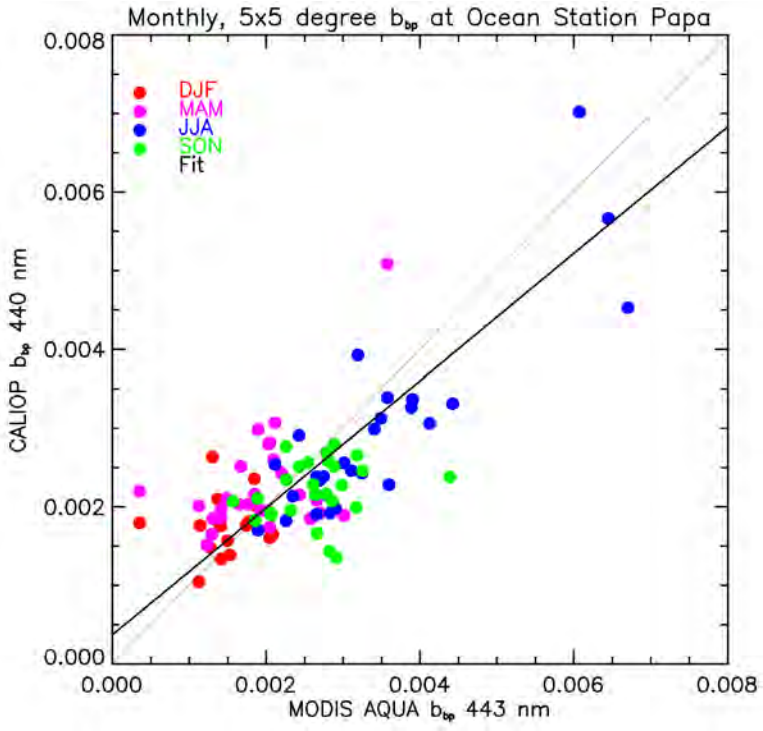

Figure 2.4 CALIOP retrieved b_{bp} vs MODIS Aqua model estimated b_{bp} Solid black line shows an OLS-bisector fit, while the dotted line is one-to-one.

The uncertainty in the CALIOP retrieved particulate backscattering coefficient can largely be attributed to the error in estimating column-integrated cross-polarized backscatter, β_{w+} [sr^{-1}]. This study used Eq. 2.2 and δ_T, the 5°x5° integrated depolarization ratio to compute β_{w+}. Figure 2.5 shows the CALIOP computed δ_T and σ estimates, where σ is the standard deviation of the mean values. With the addition of K_d from MODIS Aqua, these depolarization ratios provide direct estimates of the particulate backscattering b_{bp}, along with the associated errors (Fig. 2.6).

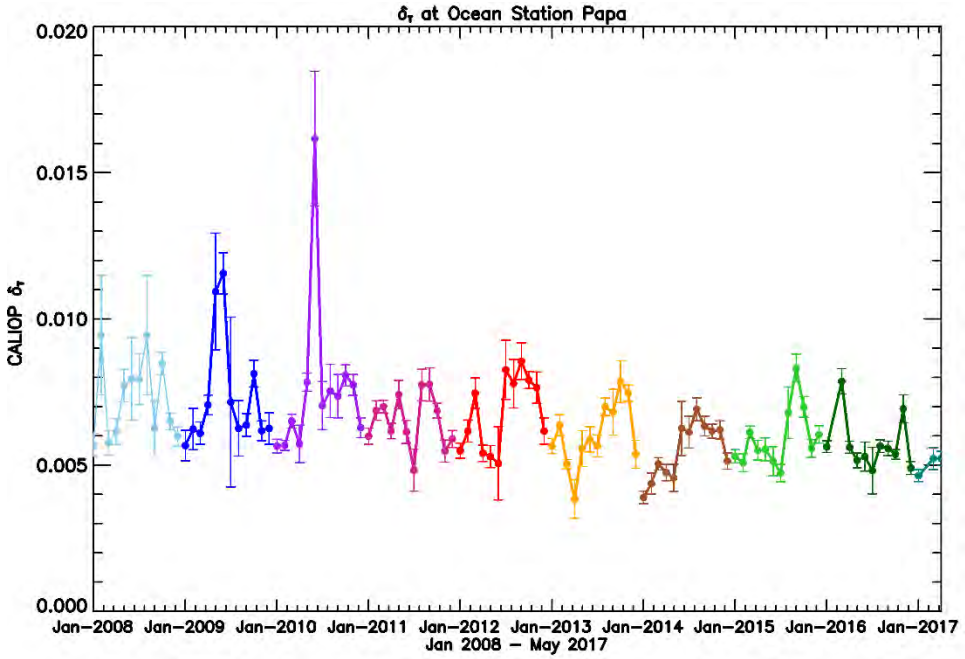

Figure 2.5 Monthly 5°x5° CALIOP column integrated depolarization ratio, δ_T, with standard deviation of the mean at Ocean Station Papa in the Pacific Ocean.

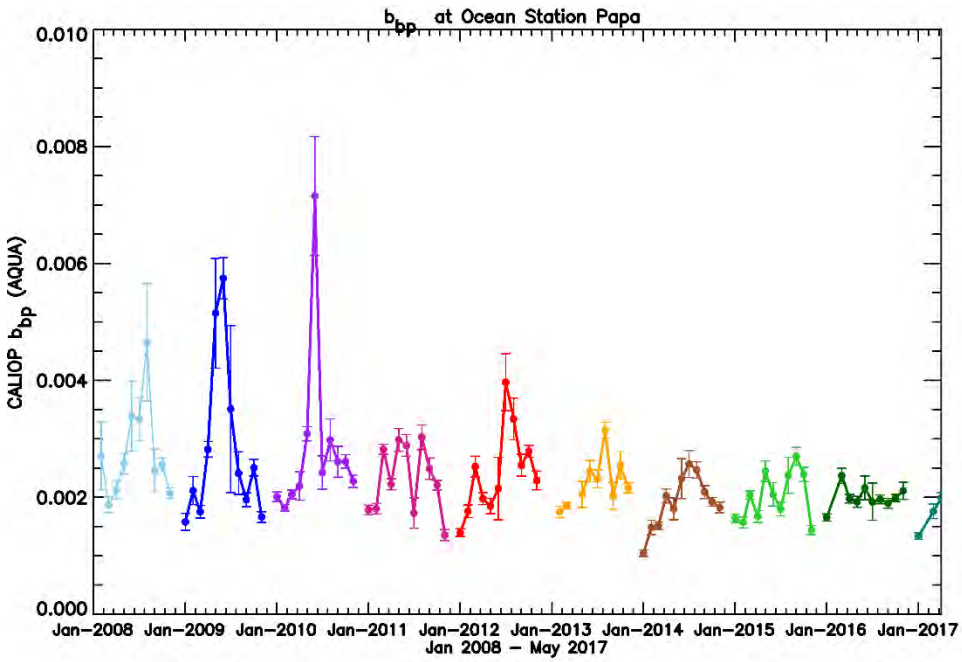

Figure 2.6. Particulate backscattering coefficient b_{bp} at OSP from CALIOP using K_d estimates from MODIS Aqua. Error bars represent the standard deviation of the mean.

Using the 9 year data set, the annual cycle in b_{bp} was revealed by computing the monthly mean, Figure 2.7 shows some agreement between the measurements. There is no information about December as for lack of diffuse attenuation coefficient measurements at this location, even though δ_T can be determined from CALIOP as shown in Figure 2.5.

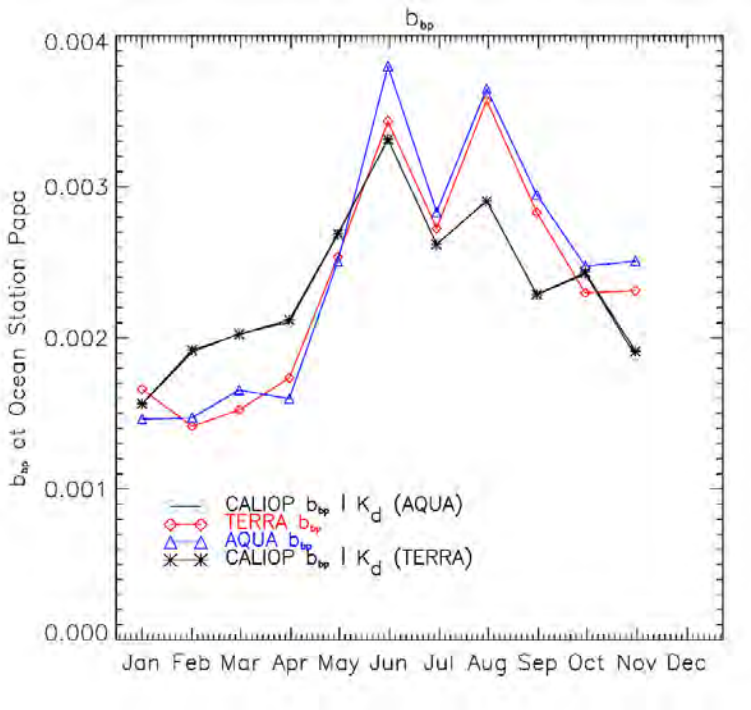

Figure 2.7 Monthly averaged b_{bp} over time period 2008 – 2016, black lines are CALIOP retrieved b_{bp} using MODIS Aqua K_d, and MODIS Terra K_d, (Aqua has circle symbols, Terra in star symbols, they are nearly identical). Blue (Aqua) and Red (Terra) lines are MODIS retrieved b_{bp}, No data values for December due to the lack of diffuse attenuation coefficient, K_d, for these months.

2.3.2 Atlantic Site – Near North Atlantic Bloom Experiment (NABE) location.

Plankton blooms in the North Atlantic Ocean are visible in satellite observations. The phytoplankton in this region play a role in the atmospheric carbon uptake by the ocean (http://www.apl.washington.edu/project/project.php?id=north_atlantic_bloom). Figures 2.8 and 2.9 show the time series of b_{bp} as retrieved from satellite at 61° N latitude, 26° W longitude. The four lines represent b_{bp} as found using information from three instruments. The two black lines are b_{bp} as computed using CALIOP total and perpendicular attenuated backscatter, β_{total} and β_{perp} and either MODIS Terra (Fig. 2.8) or MODIS Aqua (Fig 2.9) attenuated diffuse coefficient, K_d. The colored lines in both figures were retrieved using the GIOP algorithm and the MODIS observations. Only night-time data were used to compute b_{bp} using the CALIOP data. This northern location has little to no night time data in peak summer months (June and July).

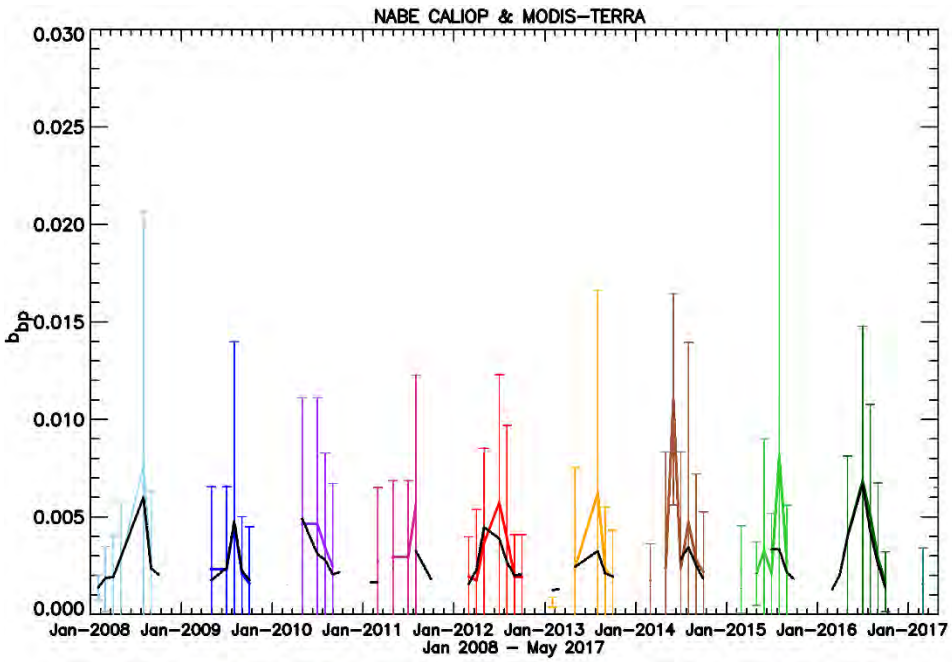

Figure 2.8 Particulate backscattering coefficient, b_{bp}, at the North Atlantic Bloom Experiment site.. CALIOP b_{bp} is retrieved using diffuse attenuation coefficient, K_d, from the MODIS measurements on Aqua, black line, using Eq. 2.3. b_{bp} from the MODIS instrument are estimated using GIOP model retrievals, where MODIS Aqua estimates are the colored lines with reported uncertainties. Each color represents a different year.

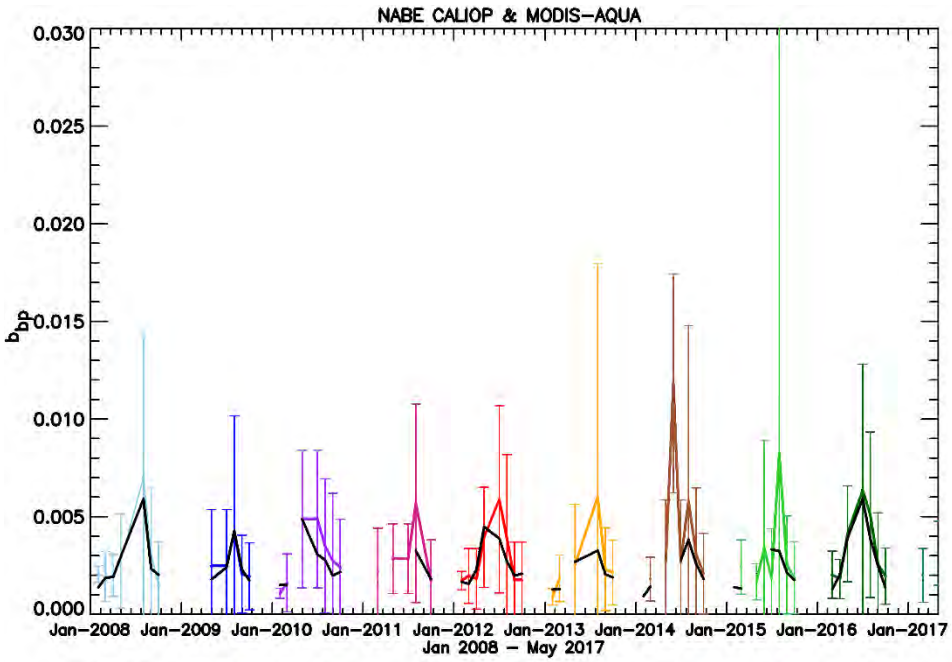

Figure 2.9 Particulate backscattering coefficient, b_{bp}, at the North Atlantic Bloom Experiment site. CALIOP b_{bp} is retrieved using diffuse attenuation coefficient, K_d, from the MODIS measurements on Aqua, black line, using Eq. 2.3. b_{bp} from the MODIS instrument are estimated using GIOP model retrievals, where MODIS Aqua estimates are the colored lines with reported uncertainties. Each color represents a different year.

Using OLS-bisector regression, the satellite estimates of b_{bp} were compared in the Atlantic Ocean. The scatterplots in Figures 2.10 and 2.11 show the MODIS estimates on the horizontal axis, and the CALIOP estimates on the vertical axis. Symbols are color coded by season, and the solid line shows the OLS-bisector fit line.

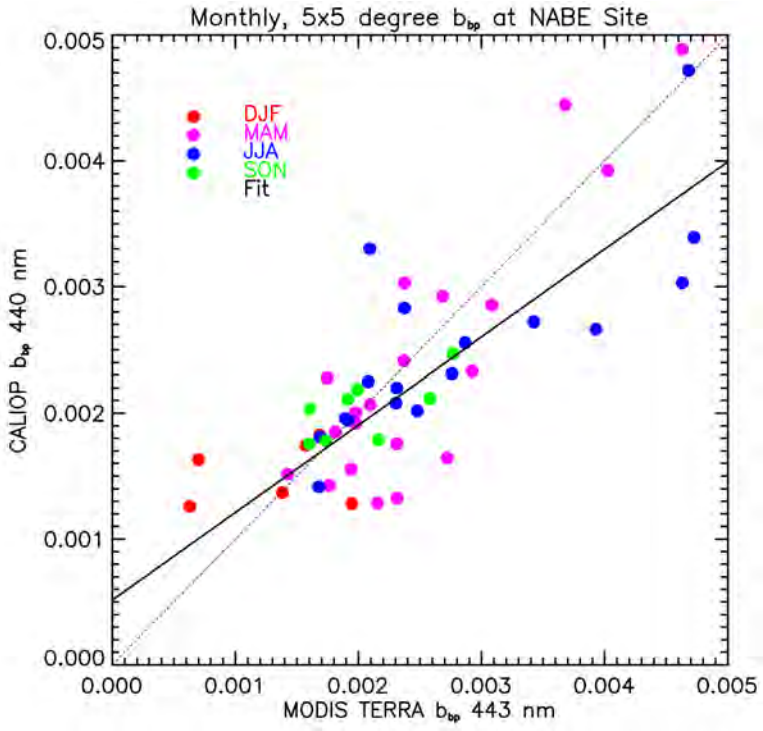

Figure 2.10 CALIOP retrieved b_{bp} vs MODIS Terra GIOP model estimated b_{bp}. Solid black line shows an OLS-bisector fit, while the dotted line is one-to-one.

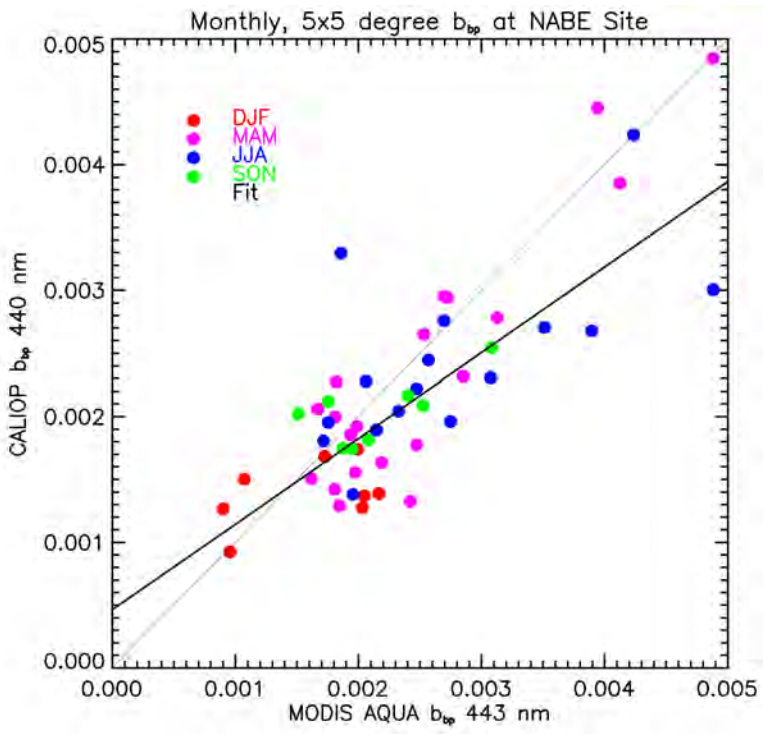

Figure 2.11 CALIOP retrieved b_{bp} vs MODIS Aqua GIOP model estimated b_{bp}. Solid black line shows an OLS-bisector fit, while the dotted line is one-to-one.

The uncertainty in the CALIOP retrieved particulate backscattering coefficient can largely be attributed to the error in estimating column-integrated cross-polarized backscatter, β_{w+} [sr^{-1}]. This study used Eq. 2.2 and δ_T, the 5°x5° integrated depolarization ratio to compute β_{w+}. Figure 2.12 shows the CALIOP computed mean δ_T and σ estimates at the North Atlantic Bloom Experiment site. With the addition of K_d from MODIS Aqua, these depolarization ratios provide direct estimates of the particulate backscattering b_{bp}, along with the associated errors (Fig. 2.13).

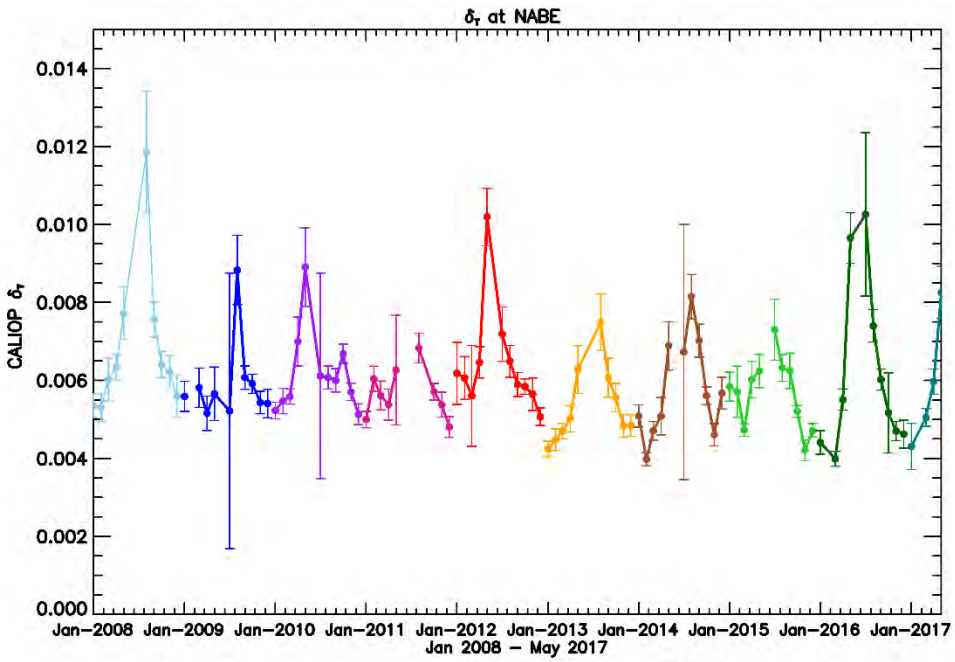

Figure 2.12 Monthly 5°x5° CALIOP column integrated depolarization ratio, $\delta_{T,}$,with uncertainty estimates at North Atlantic Bloom Experiment site.

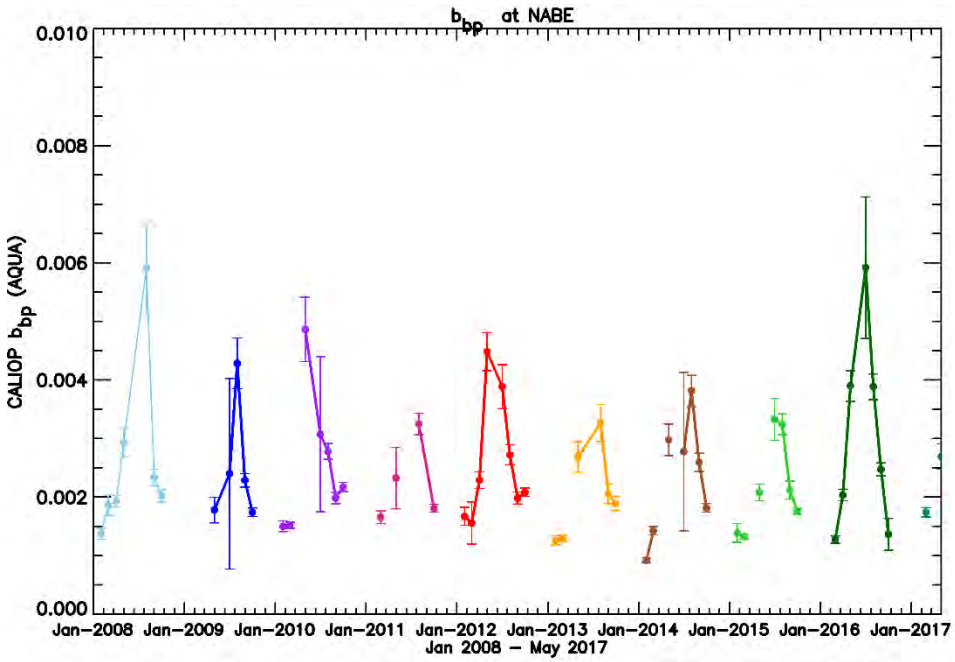

Figure 2.13. Particulate backscattering coefficient b_{bp} at NABE from CALIOP using K_d estimates from MODIS Aqua. Error bars represent the standard deviation of the mean.

Using the nine year data record, 2008 – 2016, seasonal averages of b_{bp} were computed and are shown for the lidar retrieved results in Fig 2.14 (black lines represent b_{bp} as calculated using CALIOP backscatter and MODIS Terra and Aqua K_d).

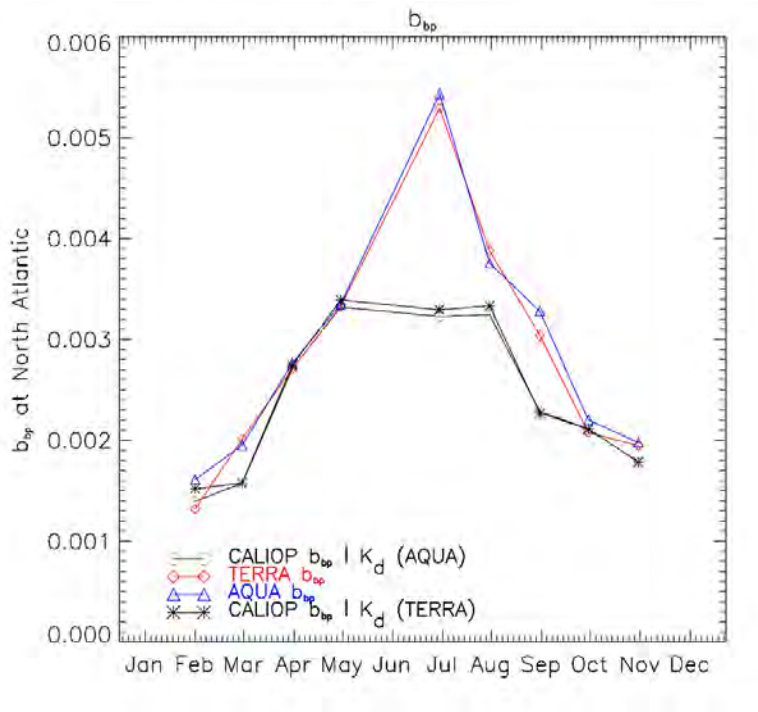

Figure 2.14 Monthly averaged b_{bp} over the period 2008 – 2016. Black line with circle symbols is CALIOP retrieved b_{bp} using MODIS Aqua K_d, Black line with star symbols is CALIOP retrieved b_{bp} using MODIS Terra K_d. Blue (Aqua) and Red (Terra) lines are MODIS retrieved b_{bp}, No values for months of January or December, no attenuated diffuse coefficient, K_d, for these months.

2.3.3 Deep-water Station ALOHA (Hawaiian Ocean Time Series, HOTS)

Measurements of various ocean parameters at deep-water station ALOHA (A Long-Term Oligotrophic Habitat Assessment) located near 22° N latitude and 158° W longitude have been ongoing since October 1988 (http://hahana.soest.hawaii.edu/hot/). The longevity, as well as the breadth of measurements, make this time series suitable for comparison of satellite observations. Figures 2.15 and 2.16 show the time series of b_{bp} as retrieved from satellite. The four lines represent b_{bp} as found using information from three instruments. The two black lines are b_{bp} as computed using CALIOP total and perpendicular attenuated backscatter, β_{total} and β_{perp} and either MODIS Terra (Fig. 2.15) or MODIS Aqua (Fig 2.16) attenuated diffuse coefficient, K_d. The colored lines in both figures were retrieved using the GIOP algorithm and the MODIS observations.

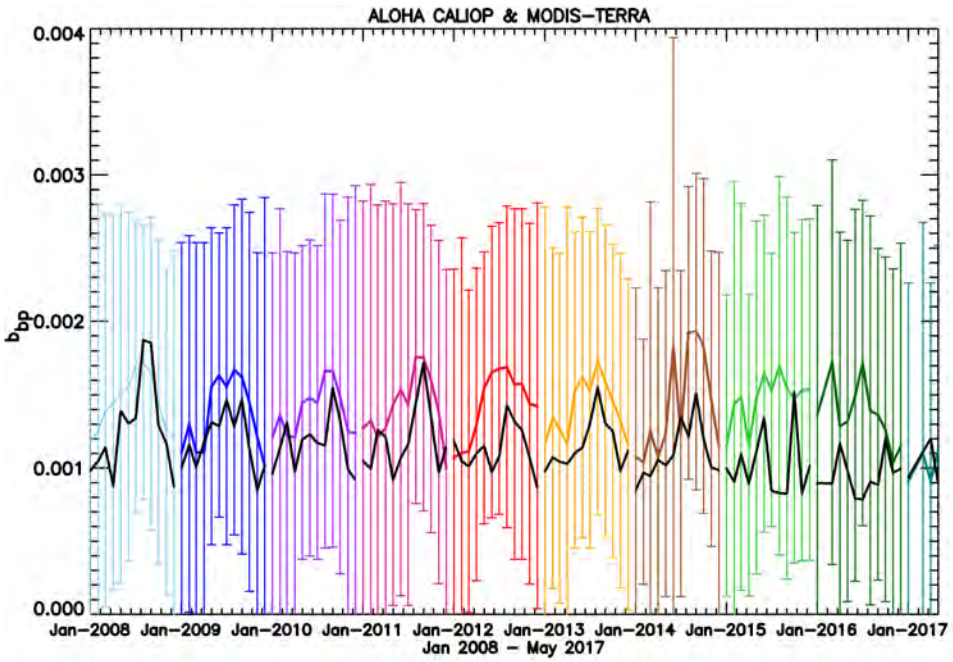

Figure 2.15 Particulate backscattering coefficient, b_{bp}, at ALOHA. CALIOP b_{bp} is retrieved using diffuse attenuation coefficient, K_d, from the MODIS measurements on Terra, black line, using Eq. 2.3. b_{bp} from the MODIS instrument are estimated using GIOP model retrievals, where MODIS Terra estimates are the colored lines with reported uncertainties. Each color represents a different year.

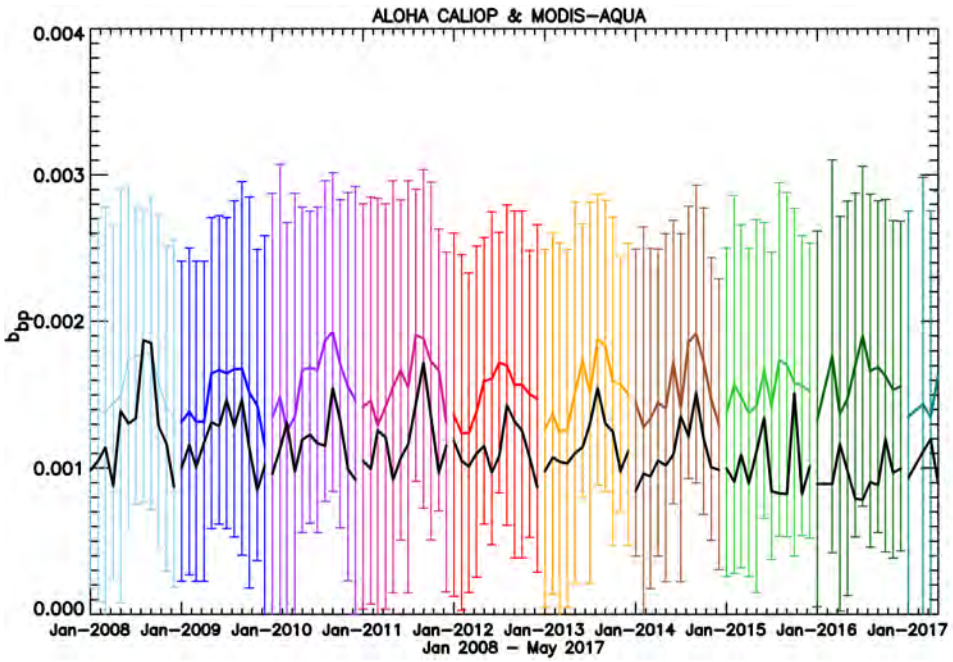

Figure 2.16 Particulate backscattering coefficient, b_{bp}, at ALOHA. CALIOP b_{bp} is retrieved using diffuse attenuation coefficient, K_d, from the MODIS measurements on Aqua, black line, using Eq. 2.3. b_{bp} from the MODIS instrument are estimated using GIOP model retrievals, where MODIS Aqua estimates are the colored lines with reported uncertainties. Each color represents a different year.

Using OLS-bisector regression, the satellite estimates of b_{bp} were compared in the Atlantic Ocean. The scatterplots in Figures 2.17 and 2.18 show the MODIS estimates on the horizontal axis, and the CALIOP estimates on the vertical axis. Symbols are color coded by season, and the solid line shows the OLS-bisector line. Similar to the results at Ocean Station Papa, winter and spring months show larger CALIOP values.

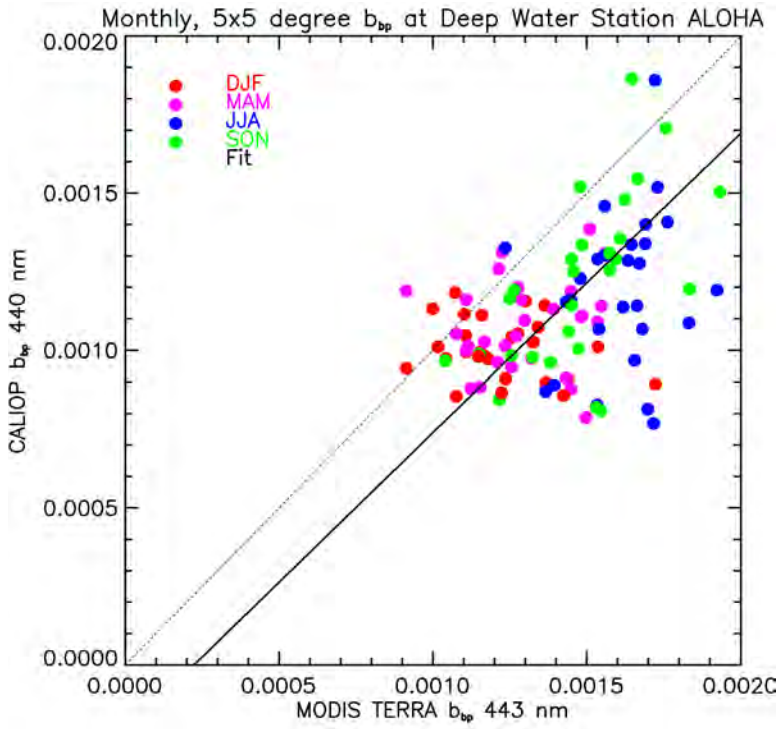

Figure 2.17 CALIOP retrieved b_{bp} vs MODIS Terra model estimated b_{bp}. Solid black line shows an OLS-bisector fit, while the dotted line is one-to-one.

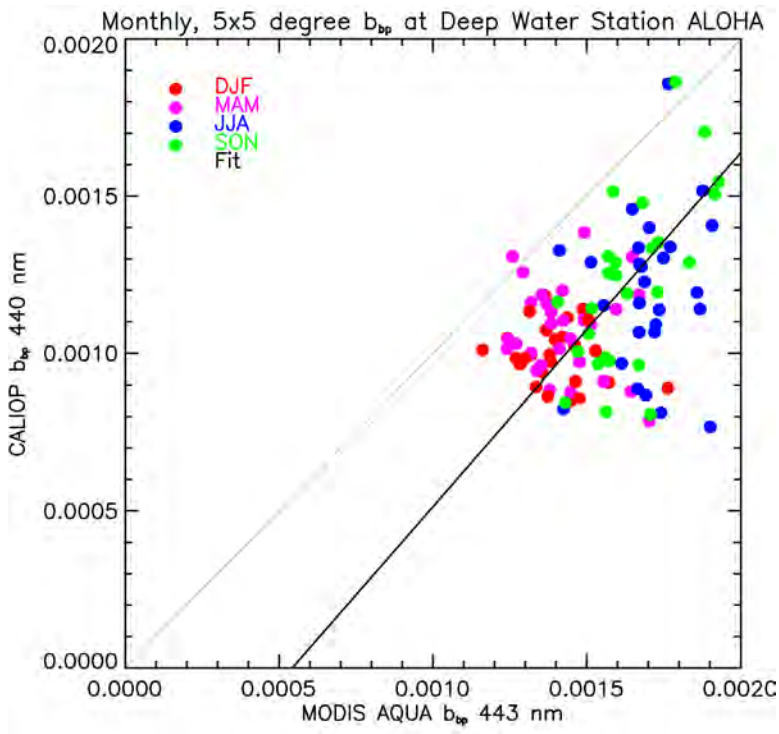

Figure 2.18 CALIOP retrieved b_{bp} vs MODIS Aqua model estimated b_{bp}. Solid black line shows OLS-bisector fit, while the dotted line is one-to-one.

The uncertainty in the CALIOP retrieved particulate backscattering coefficient can largely be attributed to the error in estimating column-integrated cross-polarized backscatter, β_{w+} [sr^{-1}]. This study used Eq. 2.2 and δ_T, the 5°x5° integrated depolarization ratio to compute β_{w+}. Figure 2.19 shows the CALIOP computed δ_T and σ estimates, where σ is the standard deviation of the mean values. With the addition of K_d from MODIS Aqua, these depolarization ratios provide direct estimates of the particulate backscattering b_{bp}, along with the associated errors (Fig. 2.20).

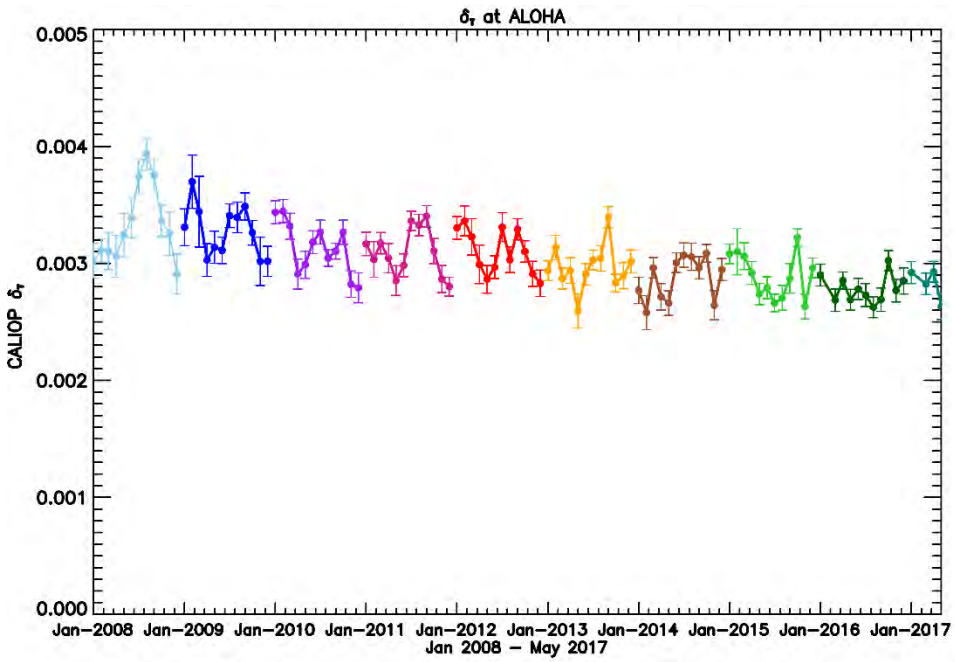

Figure 2.19 Monthly 5°x5° CALIOP estimated column integrated depolarization ratio, δ_T, with uncertainty estimates at deep-water station ALOHA. Each year represented in the data set is a different color.

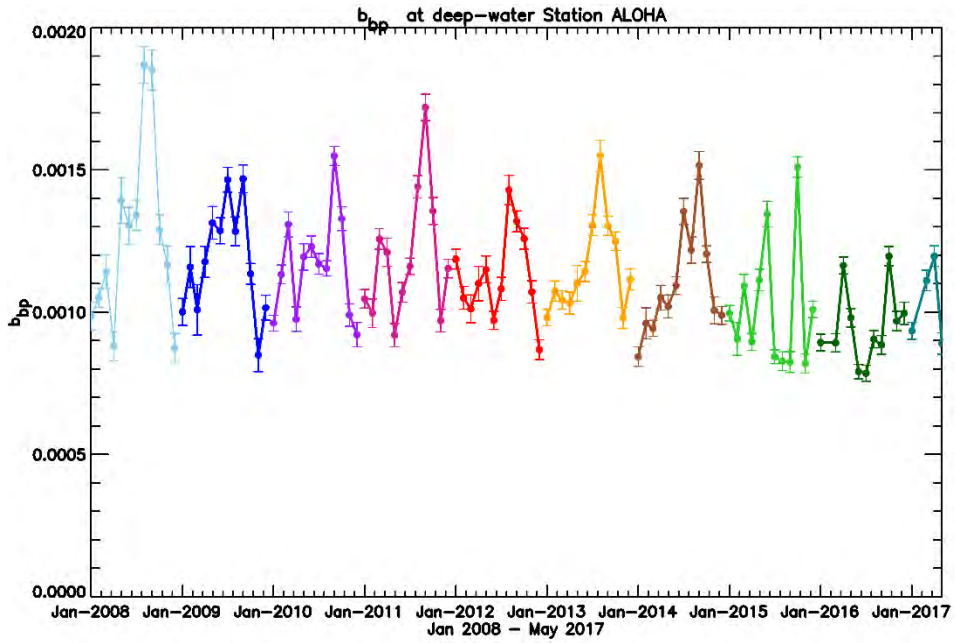

Figure 2.20. Particulate backscattering coefficient b_{bp} at ALOHA from CALIOP using K_d estimates from MODIS Aqua. Error bars represent the standard deviation of the mean.

Using the nine year data record, 2008 – 2016, seasonal averages of b_{bp} were computed and are shown for the lidar retrieved results in Fig 2.21 (black lines represent b_{bp} as calculated using

CALIOP backscatter with MODIS Terra K_d, or MODIS Aqua K_d). Despite noticeable differences in b_{bp} measured by the two MODIS instruments, the CALIOP estimates using the two different K_d values are nearly identical.

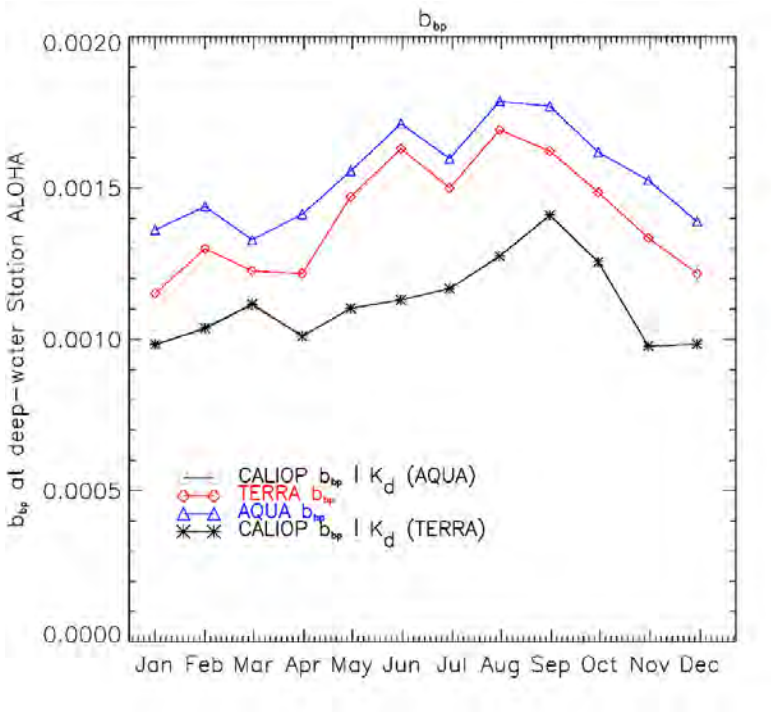

Figure 2.21 Monthly averaged b_{bp} over time period 2008 – 2016, black lines are CALIOP retrieved b_{bp} using MODIS Aqua K_d and CALIOP retrieved b_{bp} using MODIS Terra K_d. Blue (Aqua) and red (Terra) lines are MODIS retrieved b_{bp}.

2.3.4 Arctic

The melting and thinning of the sea ice in the Arctic has allowed more sunlight through and beneath the thin ice that allows for increased photosynthesis and plankton blooms. Figure 2.22 shows the time series of b_{bp} as retrieved from satellite in the Arctic (defined here as the ocean north of 65° N latitude). The four lines represent b_{bp} as found using information from three instruments. The two black lines are b_{bp} as computed using CALIOP total and perpendicular attenuated backscatter, β_{total} and β_{perp} and either MODIS Terra (Fig. 2.22) or MODIS Aqua (Fig. 2.23) diffuse attenuation coefficient, K_d. The red (Terra) and blue (Aqua) lines were retrieved using the GIOP algorithm and the MODIS observations.

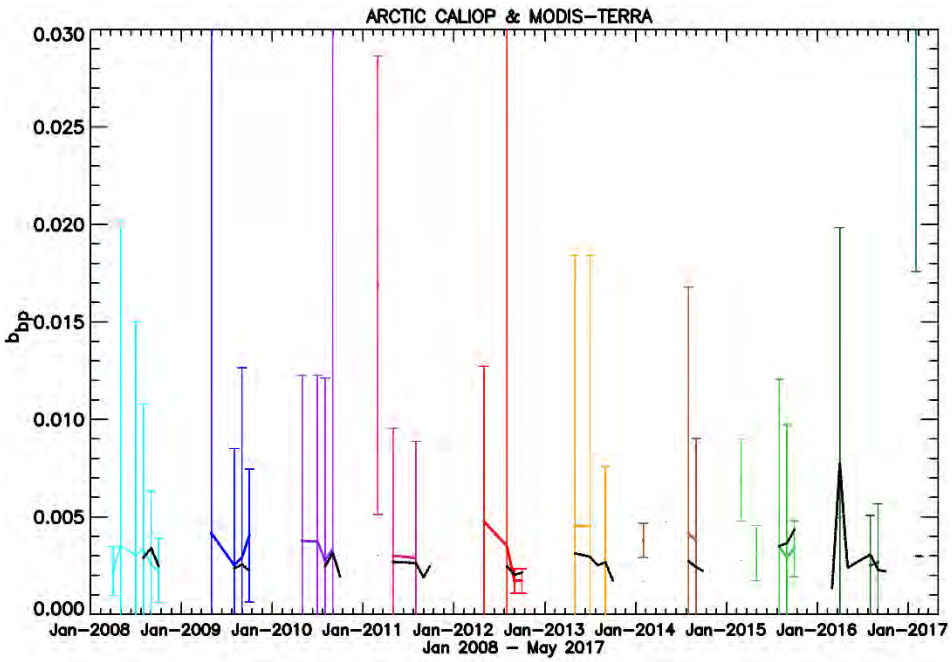

Figure 2.22 Particulate backscattering coefficient, b_{bp}, in the Arctic. CALIOP b_{bp} was retrieved using diffuse attenuation coefficient, K_d, from the MODIS measurements on Terra, black line, using Eq. 2.3. b_{bp} from the MODIS instrument was estimated using GIOP model retrievals, where MODIS Terra estimates are the colored lines with reported uncertainties. Each color represents a different year.

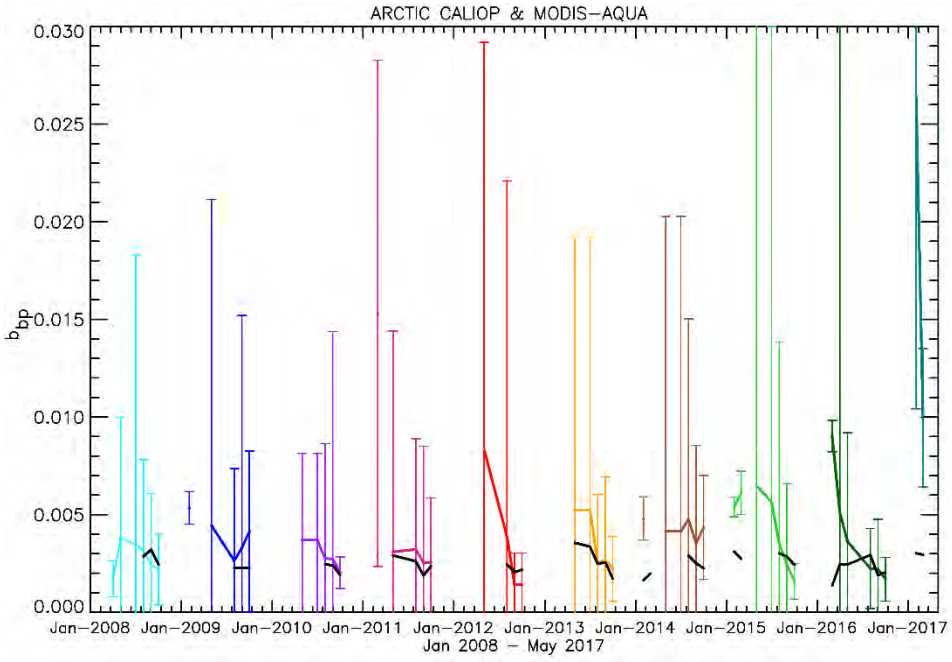

Figure 2.23 Particulate backscattering coefficient, b_{bp}, in the Arctic. CALIOP b_{bp} was retrieved using diffuse attenuation coefficient, K_d, from the MODIS measurements on Aqua, black line, using Eq. 2.3. b_{bp} from the MODIS instrument was estimated using GIOP model retrievals, where MODIS Aqua estimates are the colored lines with reported uncertainties. Each color represents a different year.

Using OLS bisector regression, the satellite estimates of b_{bp} were compared in the Arctic Ocean. The scatterplots in Figures 2.24 and 2.25 show the MODIS estimates on the horizontal axis, and the CALIOP estimates on the vertical axis. Symbols are color coded by season, and the solid line shows the OLS-bisector regression estimated fit.

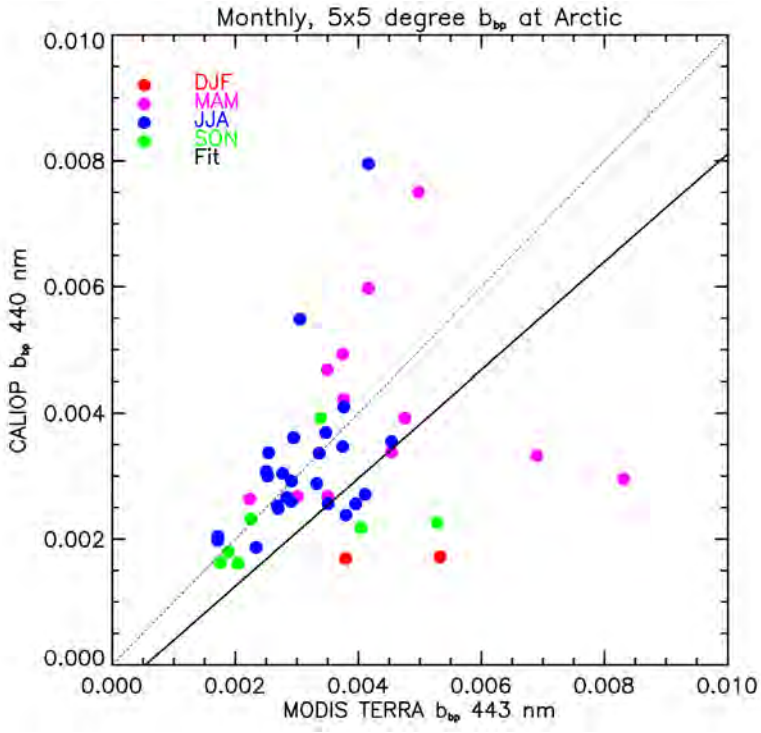

Figure 2.24 CALIOP retrieved b_{bp} vs MODIS Terra model estimated b_{bp}. Solid black line shows an OLS-bisector fit, while the dotted line is one-to-one.

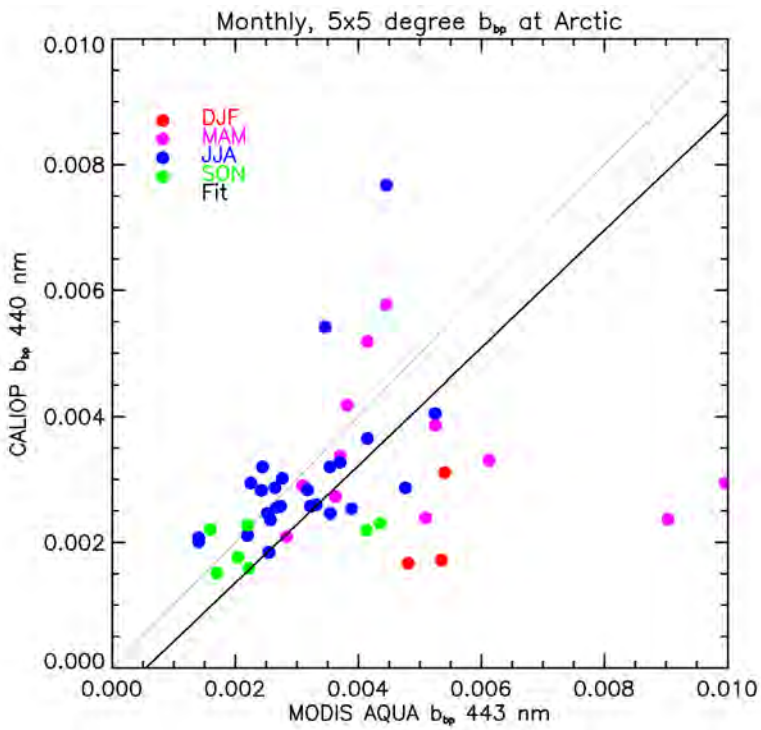

Figure 2.25 CALIOP retrieved b_{bp} vs MODIS Aqua model estimated b_{bp}. Solid black line shows an OLS-bisector fit, while the dotted line is one-to-one.

The uncertainty in the CALIOP retrieved particulate backscattering coefficient can largely be attributed to the error in estimating column-integrated cross-polarized backscatter, β_{w+} [sr^{-1}]. This study used Eq. 2.2 and δ_T, the 5°x5° integrated depolarization ratio to compute β_{w+}. Figure 2.26 shows the CALIOP computed δ_T and σ estimates, where σ is the standard deviation of the mean values. With the addition of K_d from MODIS Aqua, these depolarization ratios provide direct estimates of the particulate backscattering b_{bp}, along with the associated errors (Fig. 2.27).

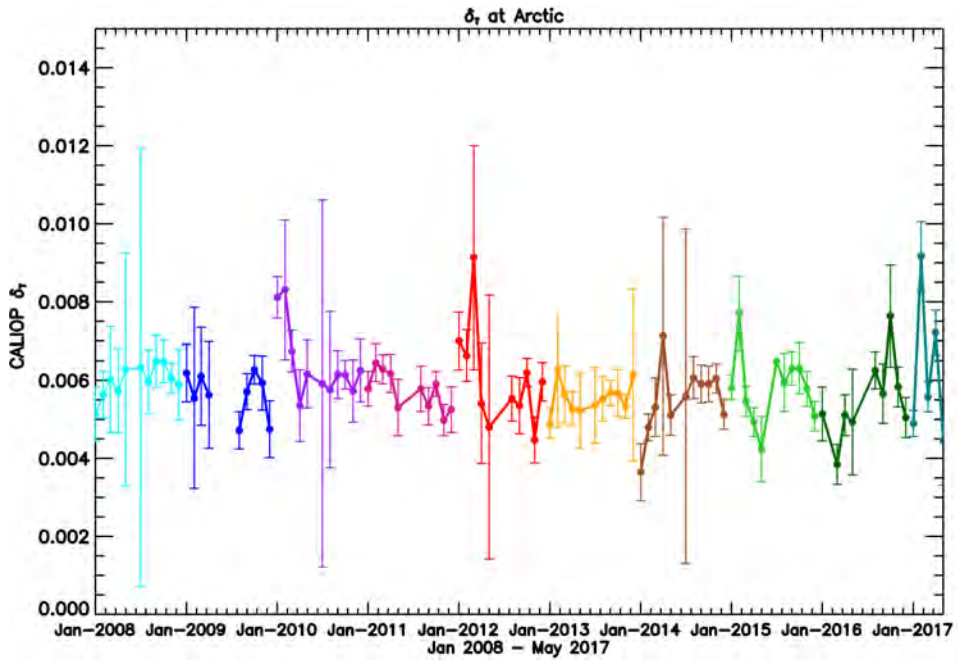

Figure 2.26 Monthly 5°x5° CALIOP estimated column integrated depolarization ratio, $\delta_{T,}$ with standard deviation of the mean in Arctic Ocean. Each year represented in the data set is a different color.

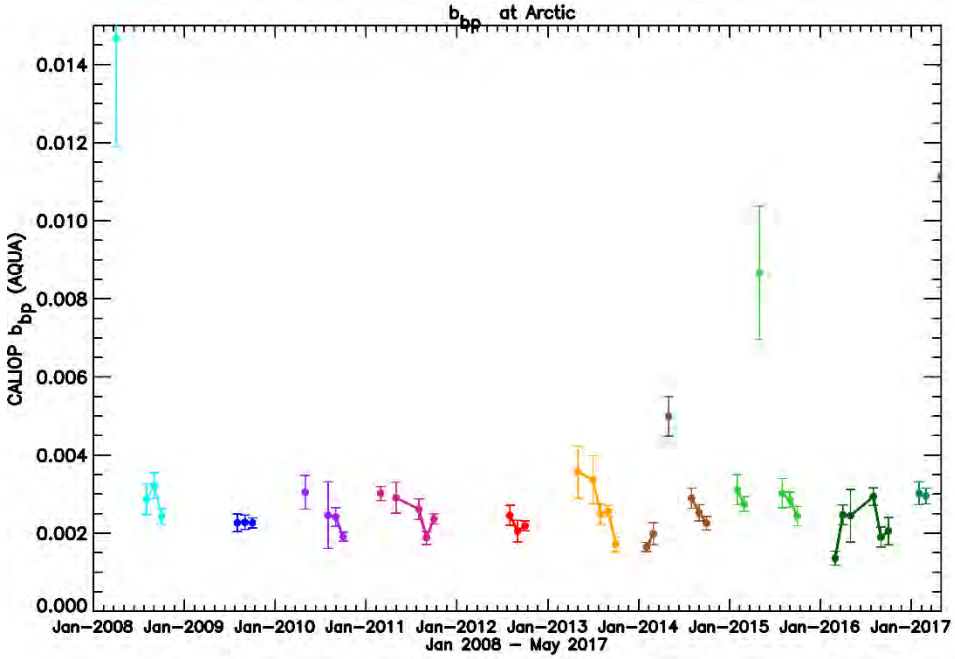

Figure 2.27. Particulate backscattering coefficient b_{bp} in the Arctic Ocean from CALIOP using K_d estimates from MODIS Aqua. Error bars represent the standard deviation of the mean.

Using the nine year data record, 2008 – 2016, seasonal averages of b_{bp} were computed and are shown for the lidar retrieved results in Fig 2.28 (black lines represent b_{bp} as calculated using CALIOP backscatter with MODIS Terra K_d, or MODIS Aqua K_d). There are no retrieved values

for November – January, because there was no diffuse attenuation coefficient, K_d, for these months.

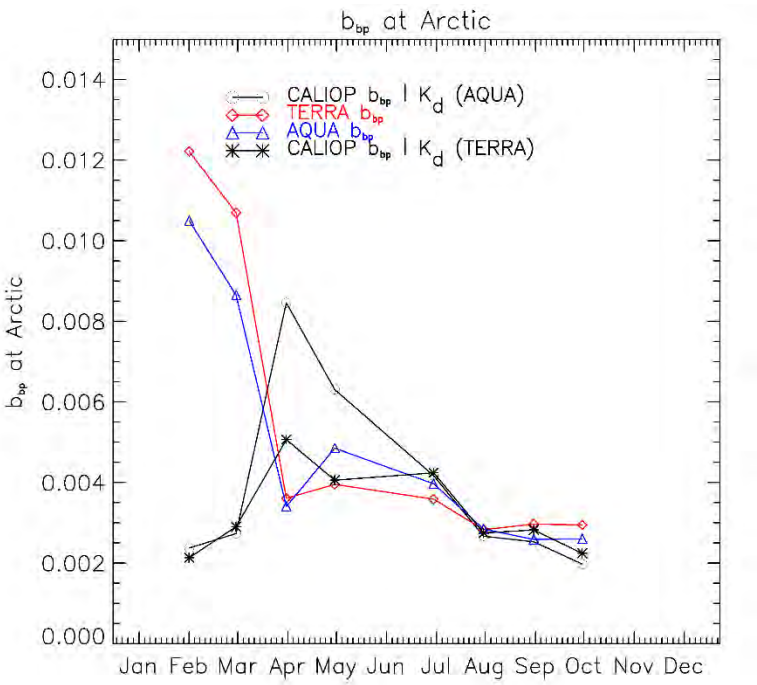

Figure 2.28 Monthly averaged b_{bp} over time period 2008 – 2016. The black lines are CALIOP retrieved b_{bp} using MODIS Aqua K_d, MODIS Terra K_d. Red (Terra) and blue (Aqua) lines are MODIS retrieved b_{bp}.

2.4 Discussion

Analysis results for the b_{bp} comparisons at all four locations are tabulated in Table 2.1. Ordinary least squares bisector regression results are shown. The RMSE values are similar for the north Pacific (OSP) and north Atlantic (NABE) sites. They are lower at the more tropical location, but much higher in the Arctic. The biases are all rather small, but in all cases, MODIS values are greater than CALIOP values. The standard deviation of the difference between the mean values from MODIS and CALIOP, σ, are similar to the RMSE. The regression generally produced slopes that are within 20% of the ideal value of unity, with the notable exception of the NABE site, where they were noticeably lower. It is not clear why this site should be so different in this regard. The correlations between MODIS and CALIOP b_{bp} values were consistent with the RMSE data – similar for the north Pacific (OSP) and north Atlantic (NABE) sites, higher at the more tropical location, and much lower in the Arctic. All correlations were significant at the 1% level, except for the Arctic cases.

Table 2.1 Results of a statistical comparison of b_{bp} from MODIS Aqua (A) and Terra (T) and CALIOP for the four geographical areas investigated. Values are provided for Root-Mean-Square-Error (RMSE), overall bias (MODIS-CALIOP), standard deviation of the difference between the mean values from MODIS and CALIOP, σ, slope and intercept from the Ordinary-Least-Squares Bisector regression, Pearson correlation coefficient, *R*, the statistical significance of the regression, *p*, and the number of monthly averages used in the regression, *N*.

		OSP	ALOHA	NABE	Arctic
RMSE	A	6.0×10^{-4}	2.7×10^{-4}	6.4×10^{-4}	2.7×10^{-3}
	T	6.8×10^{-4}	2.2×10^{-4}	6.7×10^{-4}	4.4×10^{-3}
Bias	A	1.0×10^{-4}	4.2×10^{-4}	4.6×10^{-4}	7.8×10^{-4}
	T	1.4×10^{-5}	2.8×10^{-4}	3.6×10^{-4}	3.1×10^{-4}
σ	A	7.2×10^{-4}	2.1×10^{-4}	9.5×10^{-4}	4.7×10^{-3}
	T	7.5×10^{-4}	2.3×10^{-4}	9.7×10^{-4}	4.5×10^{-3}
Slope	A	0.80	1.12	0.68	0.93
	T	0.90	0.95	0.69	0.90
Intercept	A	3.7×10^{-4}	-6.1×10^{-4}	4.6×10^{-4}	-4.9×10^{-4}
	T	2.3×10^{-4}	-2.1×10^{-4}	5.1×10^{-4}	-2.1×10^{-4}
R	A	0.74	0.41	0.81	0.10
	T	0.67	0.43	0.81	0.03
p	A	< 0.01	< 0.01	< 0.01	0.45
	T	< 0.01	< 0.01	< 0.01	0.84
N	A	98	111	60	53
	T	93	111	58	48

The lidar retrieved particulate backscattering coefficient over the 9-year period presents seasonal patterns, as expected, at each of the four regions. For example, larger b_{bp} values were generally found, as expected, in summer months when biological production is higher (Figs. 2.7, 2.14, 2.21, and 2.28). The notable exception is the Arctic, where the MODIS values are very high in February and March. These high values may be caused by contamination from sea ice.

Also as expected, the magnitude of the annual cycle was greater at the midlatitude OSP and NABE sites than the subtropical ALOHA site.

The number of data points available, *N*, also depended on latitude, with the most at ALOHA and the fewest in the Arctic. Most of the effect is a result of the use of the passive MODIS data. At high latitudes, these data are limited by low sun angles and by the limited number of daylight hours and by ice cover in the winter. By using only nighttime CALIOP data, we further limited the amount of data in the Arctic summer. In the future, we hope to investigate ways to better use daytime CALIOP data, despite the higher background light levels.

2.5. Conclusions

We were able to extract some profiles of backscattering from the CALIOP data. These were not reported, because we could not do this reliable enough for statistical analysis. The surface values obtained were reliable, and compared well with MODIS estimates of the same quantity.

3. NASA High-Spectral-Resolution Lidar Data

3.1. Evaluation of HSRL Error from SABOR Data

3.1.1. Introduction

Two different lidar configurations have been used to obtain profiles of optical properties of the upper ocean from aircraft (Churnside, 2014). The earliest measurements used a simple polarized backscatter lidar (Churnside and Wilson, 2001; Hoge *et al.*, 1988; Vasilkov *et al.*, 2001). This configuration has the advantage of simplicity and lower cost, but an inversion must be applied to the data to infer two quantities from a single measurement. In addition, obtaining quantitative information on scattering requires absolute radiometric calibration of the system. More recently, the High Spectral Resolution Lidar (HSRL) configuration, original developed for atmospheric applications (Grund and Eloranta, 1991; Shipley *et al.*, 1983), has been used in the ocean (Hair *et al.*, 2016; Moses *et al.*, 2016; Schulien *et al.*, 2017; Zhou *et al.*, 2017). This configuration is more advanced and complex, but provides an additional piece of information to the inversion, and importantly does not require absolute calibration.

In its simplest form, the signal from a single channel of a profiling lidar can be expressed as (Churnside, 2008)

$$S(z) = A\beta(\pi,z)\exp\left[-2\int_0^z dz'\alpha(z')\right], \tag{3.1}$$

where z is depth, A is a calibration factor that includes system parameters and measurement geometry, $\beta(\pi,z)$ is the volume scattering function for both seawater and hydrosols at the lidar scattering angle of π radians, and $\alpha(z)$ is the lidar attenuation coefficient. The objective is to measure the profiles $\beta(\pi,z)$ and $\alpha(z)$. For typical airborne lidar geometries, α is nearly equal to the

diffuse attenuation coefficient, K_d, and β can be used to estimate the backscattering coefficient, b_b (Churnside *et al.*, 2017; Schulien *et al.*, 2017). These parameters are important because they can be used to estimate vertically-resolved carbon and primary productivity in the upper ocean (Schulien *et al.*, 2017).

For the backscatter lidar, some method must be found to derive both $\beta(\pi,z)$ and $\alpha(z)$ from a single signal. There are several approaches available, depending on the ocean optical conditions. If the water column is well mixed, both α and β will be constant over the profile. In this case, α can be found from the slope of the logarithm of the signal and this can be used to estimate β. If the type of particles in the water does not change with depth, the profile of the optical properties will depend only on the profile of the number density of those particles. In this case, the lidar ratio (α_p/β_p) of those particles can be used, along with the known values for seawater, to resolve the ambiguity (Churnside *et al.*, 2014). If changes in the depth profile of the optical properties are not too extreme, they can be represented by the sum of their depth-averaged values and a depth-dependent perturbation. In this case, the integral of the perturbation of the attenuation will be small and can be neglected. With this approximation, the depth profile of the scattering can be found (Churnside and Marchbanks, 2017). That study showed that $\beta(z)$ could be determined to within about 10% for thin plankton layers, assuming that the lidar profile was accurately calibrated against satellite-based chlorophyll estimates.

For HSRL, an additional receiver channel removes the backscattered light from particulate scattering by spectral filtering (Hostetler *et al.*, 2018). Since the volume scattering function from seawater is known (Shifrin, 1988), this channel provides the profile of α directly. Independently, the ratio of the two channels provides the profile of β. A further advantage of HSRL is that absolute calibration is not necessary as long as the relative calibration of the two channels is known. The calibration of the relative gain between the channel is performed during each flight and has been assessed to be stable within a few percent (Hair *et al.*, 2008).

In this paper, we directly compare backscatter and HSRL techniques. Data from an HSRL are processed in the normal way. In addition, a perturbation expansion is applied to the primary seawater-plus-particulate channel, and the results are compared.

3.1.2. Materials and Methods

The data used in this study were collected using the NASA HSRL-1 during the Ship-Aircraft Bio-Optical Research Experiment (SABOR). SABOR took place in the NW Atlantic Ocean (Fig. 3.1) between 18 July and 5 August, 2014, covering both open ocean and coastal regions. The flights were made at a nominal altitude of 9000 m and speed of 100 m s^{-1}. The lidar has been described in previous publications (Hair *et al.*, 2016; Hair *et al.*, 2008), but the salient features are repeated here.

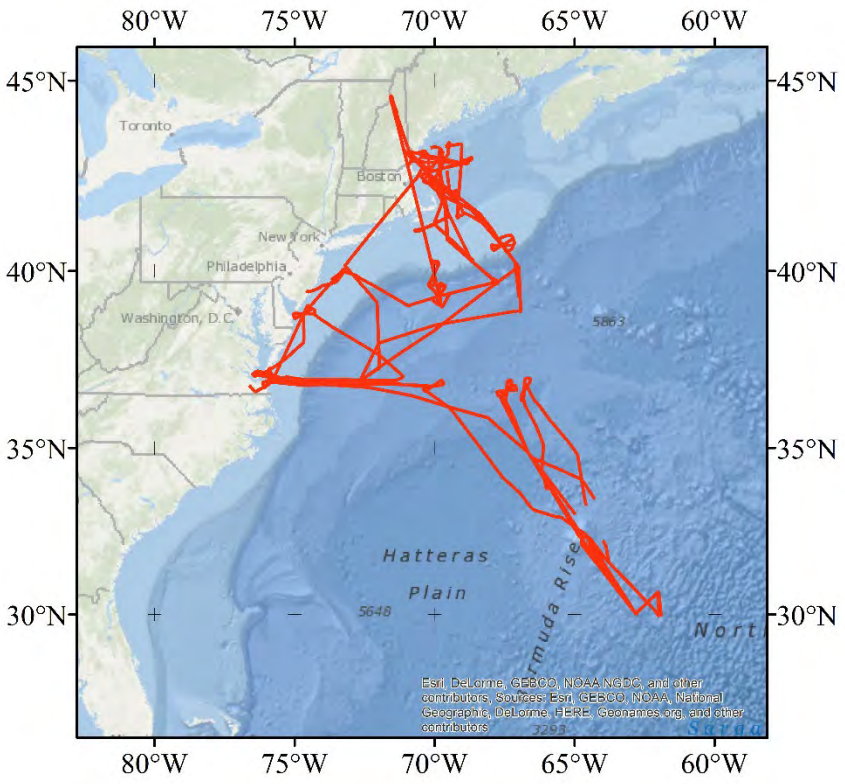

Fig. 3.1. SABOR flight tracks (red lines).

The laser produced linearly polarized light at 1064 nm and 532 nm, but only the latter is used for profiling of the ocean. The pulse repetition rate is 4 kHz, the pulse width is 6 ns, and the pulse energy is 2.5 mJ. The transmitted beam divergence is 0.8 mrad, which produces a spot diameter of about 7 m on the surface from the normal flight altitude of 9000 m. The laser light has a narrow frequency spectrum (~50 MHz) with a center frequency that is locked to the center of an iodine absorption line.

The 532 nm receiver comprised three channels – light that is co-polarized with the transmitter, light that is cross-polarized with respect to the transmitter, and co-polarized light that is filtered to pass only the frequency-shifted Brillouin component. The latter was accomplished with an iodine filter that only passes light that has been Doppler shifted by 7-9 GHz by Brillouin scattering. Each of the three channels is independently detected using a photomultiplier tube (PMT) and a hybrid photodetector (HPD) that combines a photocathode with an avalanche diode for photoelectron multiplication. Each of the resulting six signals is digitized at 120 MHz and averaged for 2000 pulses to produce each recorded profile. The 120 MHz sample rate produces a depth resolution of 0.9 m in water. The pulse averaging produces a horizontal resolution of about 50 m.

Several quality control filters were applied to the profiles. To remove profiles where the surface return was blocked by clouds under the aircraft, profiles were not used if the surface

return in the HPD Brillouin signal was below 1000 digitization levels. Also, profiles were occasionally affected by a rapid change in the surface position during the 0.5 s averaging periods. These were removed by requiring that the full width at half maximum of the ocean surface return be five samples (4.7 m) or less.

The sea surface in each profile was identified as the sample where the HPD Brillouin return was maximum. The other signals were then shifted to align with this signal. The depth penetration for each profile was inferred by comparing the value of each sample to those of the deepest 100 samples in the profile, for which the ocean scattering signal is negligible due to attenuation. Specifically, the depth penetration was defined as the shallowest sample for which either the Brillouin or co-polarized signal was less than five standard deviations above the mean of those 100 samples.

The profile of the total volume scattering function, β, at the lidar scattering angle of 180° was calculated using two different techniques. Hereafter, we will refer to this quantity as the volume backscattering, and drop the explicit dependence on scattering angle. The first was the standard HSRL technique,

$$\beta(z) = \frac{S(z)}{S_B(z)}\beta_B, \tag{3.2}$$

where z is depth, S is the signal in the co-polarized channel, S_B is the signal in the Brillouin channel and β_B is the volume backscattering of seawater.

The second technique did not use the information in the Brillouin channel. Instead, it used the inversion technique described in (Churnside and Marchbanks, 2017). In this technique, we defined a linear regression to the logarithm of the signal for each profile to obtain

$$\ln\left[S_0(z)\right] = \ln\left(A\beta_0\right) - 2\alpha_0 z, \tag{3.3}$$

where A is a calibration coefficient relating the signal to β, β_0, which does not vary with depth, was obtained from the intercept of the linear regression, and α_0, which does not depend on depth, was obtained from the slope of the regression. The depth range of the regression was from 5 m to the depth at which the signal fell below a threshold that was set at five standard deviations of the noise above the background level. The profile of β was then approximated by

$$\beta(z) = \frac{S(z)}{S_0(z)}\beta_0(z). \tag{3.4}$$

Note that the absolute calibration is required for this technique. In (Churnside and Marchbanks, 2017), this was obtained from a comparison with satellite chlorophyll estimates using a bio-optical model. In this work, a calibration coefficient was estimated using the HSRL values. To allow for the possibility of the calibration changing from flight to flight, the calibration

coefficient was chosen for each flight such that the mean value of β for the flight was the same for both techniques.

Another difference is that the data used in this paper were more affected by noise than in (Churnside and Marchbanks, 2017). As a result, the linear regression used a weighting function to reduce the effects of decreasing signal to noise ratio with increasing depth. It is straightforward to show that, for Gaussian noise, the variance of the logarithm is approximately

$$\sigma_{\ln(S)}^2 \approx \frac{\sigma_S^2}{\langle S \rangle^2} + \frac{5\sigma_S^4}{2\langle S \rangle^4}, \tag{3.5}$$

where the noise variance in the signal, σ_S^2, was estimated from the last 100 samples of each signal profile, and the mean was approximated by the measured value at each depth to obtain weighting factors for the regression. At the limit of depth penetration defined above, the second term is 10% of the first term, and the second term was ignored in the calculation.

For the HSRL technique, the attenuation coefficient was estimated from the Brillouin channel. At each depth below the surface, the slope of the logarithm of the signal was calculated using the sample just before and the sample just after the sample under consideration. For the surface value, Lagrangian interpolation of the surface sample and the first two sub-surface samples was used to obtain a quadratic polynomial, and the derivative of this was evaluated at the surface. To reduce the effects of noise, these values were averaged using a five sample (4.7 m) sliding window. For the surface and first subsurface sample, this average would normally include values above the surface; these were replaced by the surface value in the average.

3.1.3. Results

Typical profiles (Fig. 3.2) show good agreement between the HPD and PMT data. The notable exception occurs when the attenuation is high, as in the left panel of the figure where the lidar attenuation between 5 and 15 m is about 0.18 m^{-1} for all signals. In these cases, the PMT data are higher than the HPD data at low signal levels. This is caused by afterpulsing in the tubes and was the motivation for using the HPD detectors. It is not seen when the lidar signal drops off more slowly, as in the right panel where the lidar attenuation (between 5 and 30 m) is about 0.068 m^{-1}. Because of this effect, the following analyses will use the HPD data. The uncertainty in the returns is greater for the co-polarized channel than for the Brillouin channel, despite the lower volume backscattering of the latter, because the collected light is split so that 90% goes into the Brillouin channel and 10% into the co-polarized channel.

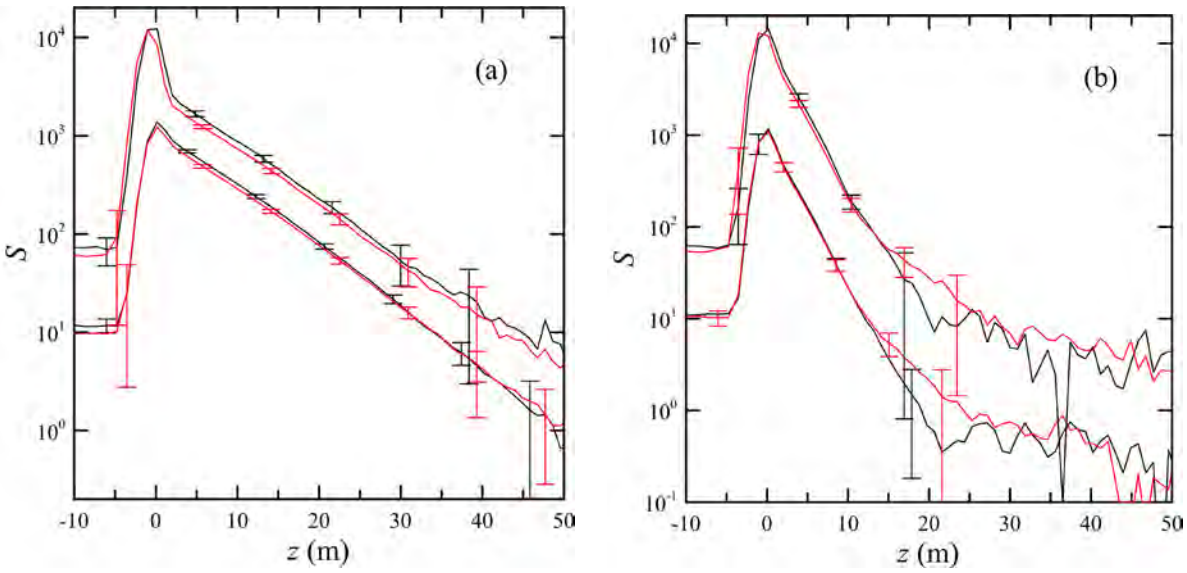

Fig. 3.2. Examples of lidar signal *S* as a function of depth *z* from (a) open ocean and (b) coastal regions. Curves are average of 100 profiles. Error bars represent the standard deviation of the 100 samples at selected depths. Black curves are HPD and red curves are PMT data. Lower pair of curves are the Brillouin channel and upper pair are the co-polarized channel.

Examples of single profiles and the corresponding retrieved parameters (Fig. 3) illustrate the differences between the two methods. On the left is an open-ocean case (65.65° E, 33.58° N), where the optical properties of the water are relatively constant in the upper 30 m, except right at the surface. The surface enhancement in the Brillouin channel is a result of enhanced backscatter induced by surface waves. In the co-polarized channel, it is a combination of enhanced backscatter and specular reflections from surface wave facets at the lidar incidence angle of 15°. Because of the enhancement in the Brillouin channel, the HSRL attenuation coefficient is probably too large near the surface. At depths from 5-30 m, however, the HSRL-derived profile of attenuation is close to the value obtained from the perturbation technique, with an average value that is about 8% higher. Because the surface-wave enhancement affects both HSRL channels, the inferred value for β at the surface is an accurate estimate of the combined specular surface return and near-surface volume backscattering. In this example, a calibration factor was applied to the values for β inferred from the perturbation technique to get good agreement at 10 m. With this correction, the perturbation technique overestimates this value by 50% in this case. The corrected values for β agree fairly well from 5-30 m, with the perturbation technique underestimating β by an average of 8%. This increases at greater depths, so the average between 20 and 30 m is 16%.

On the right of Fig. 3.3 is a typical near-shore profile (75.40° E, 36.91° N), where the optical properties of the water are more variable. The water depth at this location is about 28 m, and there is a noticeable change in both attenuation and scattering at a depth of about 13 m. In this example, the enhanced backscatter effect is smaller and the specular reflection is larger. The result is that the HSRL technique does not overestimate the attenuation at the surface, and in fact,

may underestimate is somewhat because of the averaging process. Both techniques produce the high surface β values in this case, with a difference of about 12%. Between 2 and 12 m, the techniques produce β values that are within 4% of each other. The perturbation technique does not perform as well below the change in water properties, however. The derived values for β are too low by as much as 76%.

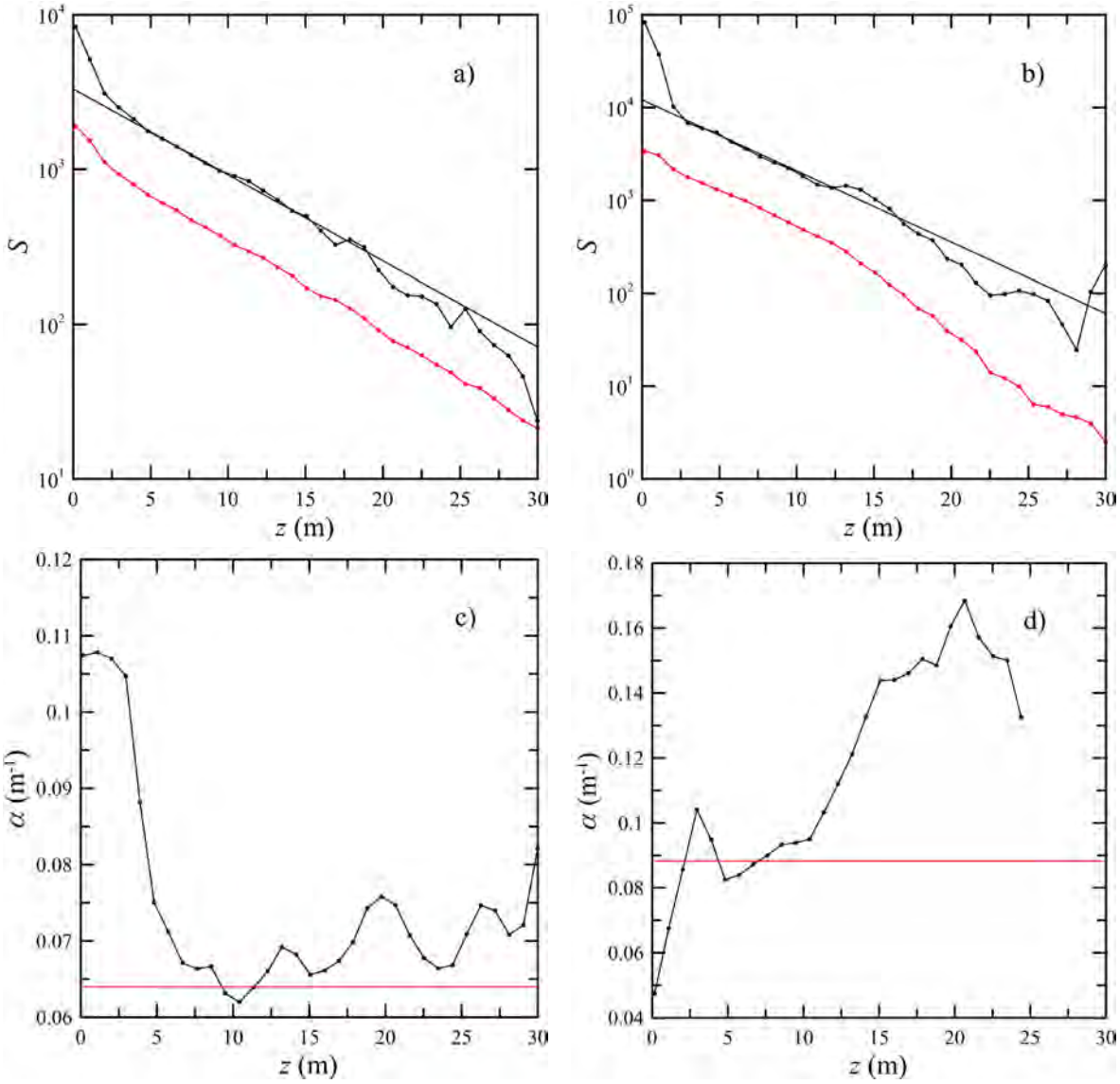

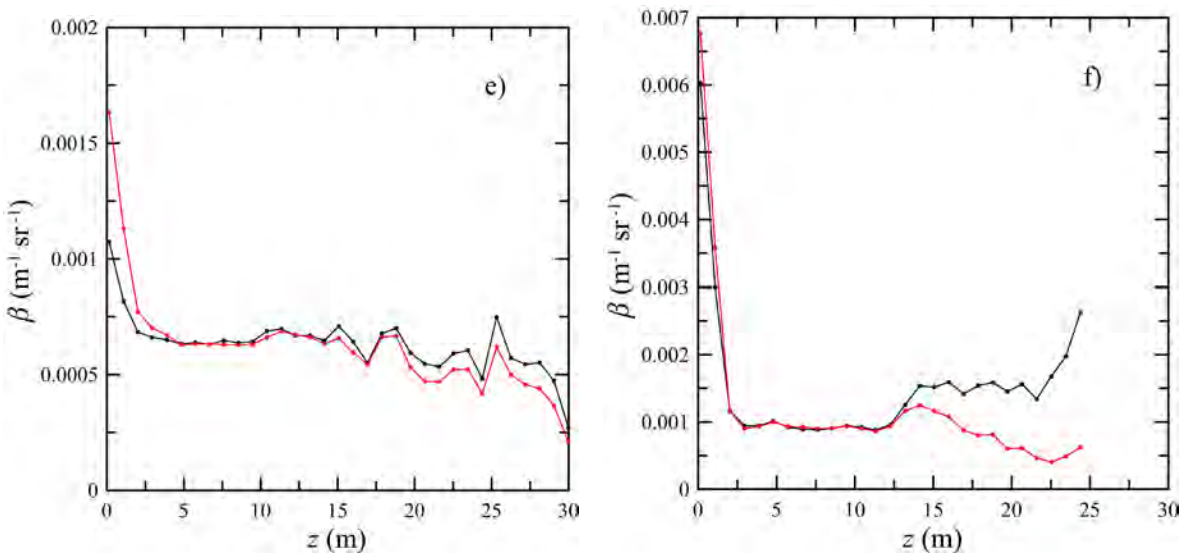

Fig. 3.3. Single profile results for off-shore and near-shore cases. (a) Signals, *S*, vs. depth, *z*, for off-shore case. Red line is Brillouin signal with sample depths marked by small circles. Black line is co-polarized signal, and straight black line is linear regression. (b) Signals for near-shore case. (c) Attenuation, α, vs z for off-shore case. Red line is perturbation result and black line is HSRL result. (d) Attenuation for near-shore case. (e) Volume backscattering, β, vs z for off-shore case. (f) Volume backscattering for near-shore case.

The rest of this section considers statistics of all of the data from the SABOR mission that passed the quality-control measured described above. For example, Fig. 3.4 presents a scatter plot of ocean attenuation coefficients obtained from the two different processing techniques. The total number of data pairs in this plot was 1799238. The correlation between them was 0.70. While the points are clustered near the one-to-one line, there also numerous points where the PE value is below the HSRL value. Overall, the mean value derived from the PE was 0.079 m^{-1}, and the mean value derived from the HSRL was 0.089 m^{-1}, which represents a relative bias of 11%. The root-mean-square difference of the two quantities was 0.022 m^{-1}.

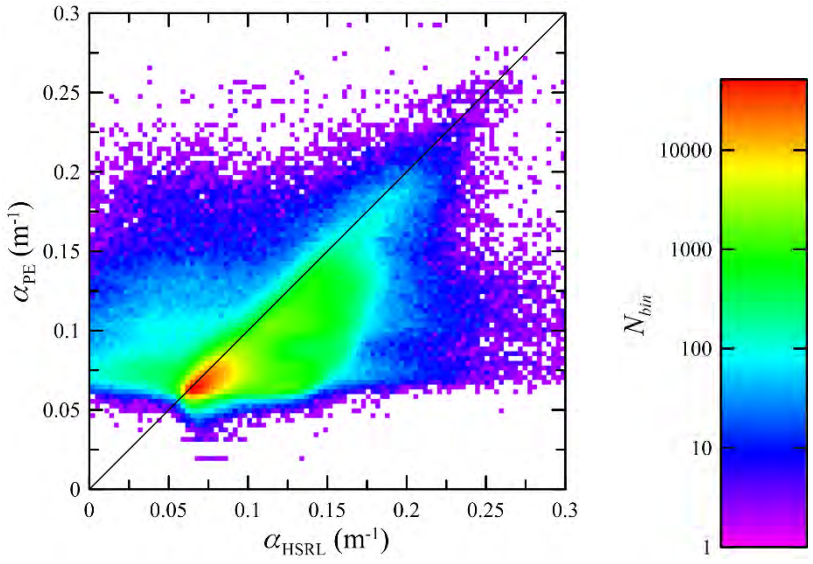

Fig. 3.4. Scatterplot of attenuation coefficients derived by the two methods on a log scale. The number in each 0.003 m^{-1} square bin is color coded according to the scale on the right. The black line is the ideal one-to-one relationship.

The correlations between the volume backscattering derived from the HSRL processing and derived from the inversion of the co-polarized channel (Fig. 3.5) were calculated at 2.5 m depth intervals down to a depth of 30 m, which was the average penetration depth for the data set. The surface was not included, because of the effects of the Fresnel reflection on the co-polarized channel. Near the surface, where the signal-to-noise ratio is large, the correlation is high. It starts to drop off at about 10 m. Below about 20 m, the correlation begins to increase as a result of noise in the co-polarized channel that is common to the results of both processing techniques.

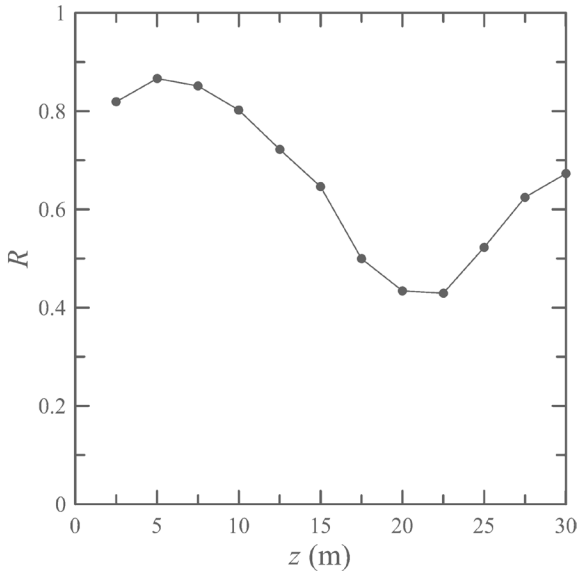

Fig. 3.5. Depth dependence of correlation coefficient R as a function of depth, z for volume backscattering , β.

Because of the way the retrieval data were calibrated, the average value for β over all depths was the same for both techniques, although there are differences at different depths (Fig. 3.6). The error bars in the figure represent the standard deviation of data. The relative difference in the means was 13% or less, except for the value at 2.5 m depth. The volume backscattering decreases at depths greater than about 15 m, because regions with very high scattering also had high attenuation, and the penetration depth was less. The low bias in the attenuation coefficient implies that the attenuation correction in the perturbation estimate of β is generally too low; this produces a bias in the perturbation estimate of β that is increasingly negative with depth.

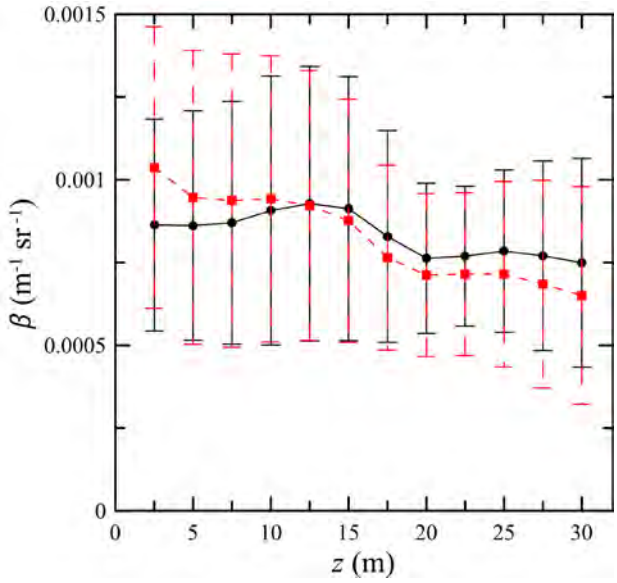

Fig. 3.6. Mean volume backscattering, β, as a function of depth, z for HSRL processing (black circles with solid line) and the perturbation retrieval (red squares with dashed line). Error bars represent ± 1 standard deviation.

To estimate the relative errors of the two techniques, we calculated the mean and standard deviation of segments of the data comprising 100 consecutive profiles. We will consider the coefficient of variation, *CV*, which is the ratio of the standard deviation to the mean for each quantity at the same 2.5 m depth intervals as before. The 100 profiles correspond to about 50 s of data, or 5 km along the flight track. Ideally, the number of profiles used would be enough to get a good estimate of the variability, but the distance would be smaller than the scale of changes in oceanographic conditions. In practice, variability in the ocean occurs over a wide range of scales. In a study using the same data set as this paper, characteristic scales between 200 m and 600 m were inferred (Moses *et al.*, 2016). However, previous lidar measurements found a power-law spectrum with a slope of -1.5 and no characteristic scale between 5 m and 200 km (Churnside and Wilson, 2006). While the CV at the shallow depths may include contributions from oceanographic variability, the increase with increasing depth (Fig. 3.7) suggests that the deeper values are dominated by noise effects. The errors in shallower, more turbid waters on the continental shelf are larger than those in deeper waters off shore. Note that there is a local peak

in the coastal values at a depth of 20 m. Deeper than this, some of the noisier data are removed from the average, because they are deeper than the local penetration depth.

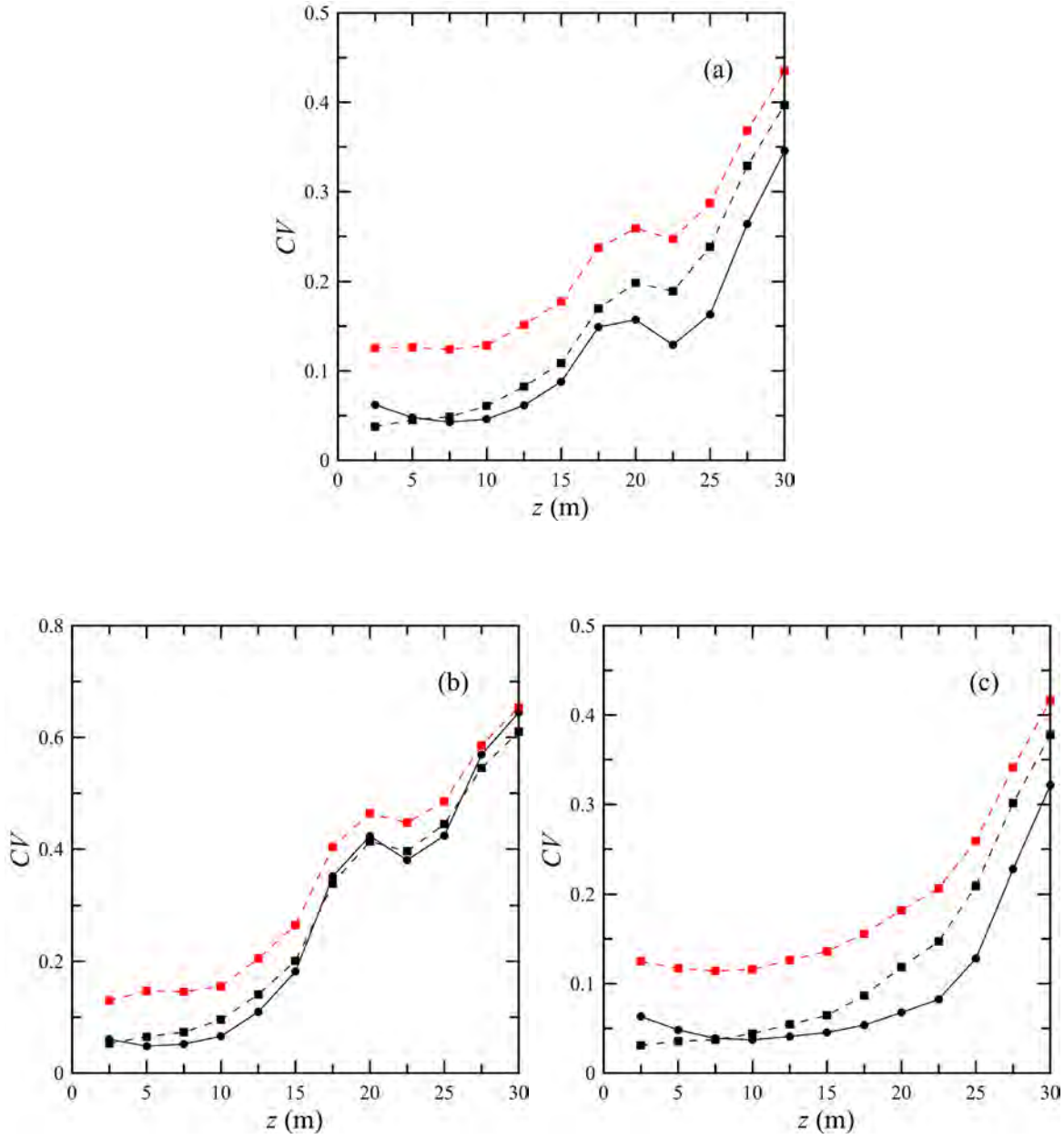

Fig. 3.7. Coefficient of variation, *CV*, as a function of depth, *z*, for α (solid lines with circles) and β (dashed lines with squares) processed using the HSRL technique (black) and the perturbation technique (red). (a) all data, (b) values where water depth < 200 m, and (c) values where water depth > 1000 m.

3.1.4. Discussion

One interesting feature of these data is the difference in both α and β near the surface. The explanation is that surface waves produce an enhanced scattering near the surface at a scattering angle of 180° (Bliokh and Kravtso, 2004; Kokhanenko *et al.*, 2005; McLean and Freeman, 1996). The HSRL technique using iodine filters and a laser that has high spectral purity, enables a direct measure of the expected enhanced backscatter near the ocean surface (0-10m) by removing the ocean surface reflection. The mean enhancement of the Brillouin channel, estimated by comparing the peak return in the channel with the return that would be expected by extrapolating deeper returns back to the surface, was 40%. This is consistent with the results of McLean and Freemen (McLean and Freeman, 1996), where an enhancement of up to 50% was predicted at a depth of 1 m. Because the enhancement is the same for the Brillouin and co-polarized channels, the HSRL technique is not affected, while the perturbation technique overestimates β at 2.5 m as expected. On the other hand, the enhancement affects the HSRL retrieval of attenuation near the surface, while the perturbation technique is less affected due to the assumption of a constant attenuation at all depths and because the fit does not use the data near the surface for the regression. This suggests that a more accurate estimate of α at the surface can be obtained from HSRL data by extrapolation from near-surface values not affected by enhanced backscatter. Potentially, this can be improved using an assumed extinction-to-backscatter ratio and the backscatter to get a better estimate.

This analysis does not consider the fact that radiometric calibration of the lidar is required if the HSRL technique is not used. Calibration of atmospheric lidar has been an issue for some time (Bilbro *et al.*, 1986; Hall and Ageno, 1970; Kavaya and Menzies, 1985), and is an area of ongoing research. For airborne or space-based oceanographic lidar, the use of known targets like homogeneous land surfaces (Cutten *et al.*, 2002) or the sea surface (Hu *et al.*, 2008) has been suggested, but these approaches add additional constraints on the lidar system to be used in practice. For the sea surface approach, a satellite measurement of surface winds with an accuracy of 1 m s^{-1} should be sufficient to provide a calibration to within 10% (Hu *et al.*, 2008). Laboratory calibrations rely on the stability of the calibration when the system is deployed along with careful monitoring the absolute value of the laser energy.

Note that the effects of atmospheric attenuation by aerosols must be considered in the PE retrieval, except at low flight altitudes. For HSRL, this can be accurately estimated using the molecular channel, but is not required to obtain the oceanic parameters. For example, Figure 3.9 presents the two-way transmission from the aircraft to the surface and back for the first flight. Without the HSRL atmospheric profile, however, estimation of this transmission is generally not possible. For an aircraft at an altitude of 9000 m, the calibration error that would be introduced by neglecting aerosol extinction would be > 10% for this entire flight and varying up to 25%. In general the attenuation will depend on the attenuation down to the surface including aerosol and tenuous clouds (e.g. cirrus clouds). However, for an aircraft flight altitude of 300 m, the calibration error would have been generally < 3%, and < 10% for an altitude of 1000 m.

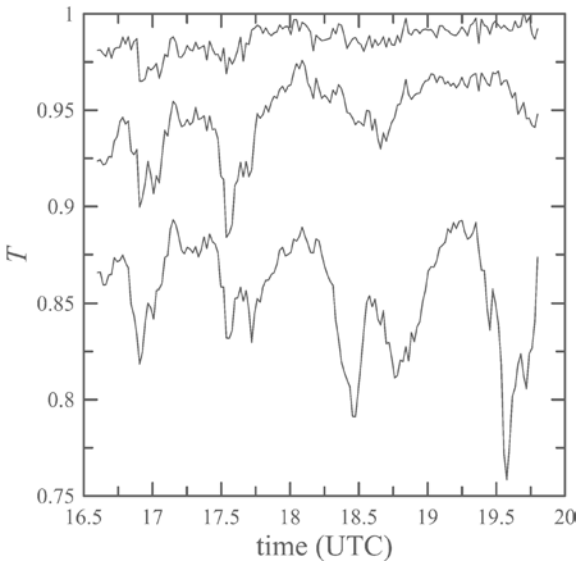

Fig. 3.9. Two-way atmospheric transmission, *T*, as a function of time for the first flight. From top to bottom, curves represent aircraft altitudes of 300 m, 1000 m, and the actual altitude of the flight at about 9000 m.

3.1.5. Conclusions

A perturbation retrieval was compared with HSRL processing to derive a profile of the volume backscattering. For the data set considered, we found that the perturbation technique performed better when the water properties were more vertically uniform, as in the oligotrophic waters, than it did near shore where the water tends to be more variable, as expected due to the retrieval assumptions. For the data set investigated, the attenuation coefficient inferred using the perturbation method was biased low compared with that from the HSRL. A negative bias in the scattering parameter increased as the depth increased on average. Near the surface, the coefficient of variability in both estimates of attenuation and in HSRL estimates of scattering were around 5%, but that in the perturbation estimate of scattering was over 10%. At greater depths, the variability increases for all of the profile parameters. This reflects the effects of increased shot noise at greater depths.

The comparisons were based on data from the same lidar, therefore these results show the improvements in performance that can be expected from the HSRL method in a way that does not depend on the specific characteristics of the lidar. These improvements include reduced bias, reduced sensitivity to noise, and reduced sensitivity to gain variations. Another key advantage is that only relative calibrations between the channels are required, and these can be done within the lidar itself. A standard backscatter lidar requires an estimate of atmospheric attenuation below the aircraft to avoid bias in the ocean retrievals, although these effects can be reduced by operating at lower flight altitudes. The HSRL technique accounts for the effects of atmospheric attenuation directly. The primary disadvantage to the HSRL technique is the requirement for a

single-frequency laser and inclusion of an optical filter in the receiver. Another disadvantage is that the returned light has to be separated into two channels, which decreases the signal to noise ratio. Both techniques are affected by surface roughness, and our results show that the HSRL estimate for attenuation near the surface needs to account for these effects. We showed that the effect can be evaluated using the constant attenuation profile retrieval when conditions are well mixed with depth. This effect may also provide information on the sea surface state given further evaluation.

3.2. Monte-Carlo Analysis of Enhanced Backscatter

3.2.1. Introduction

In working with the HSRL data, we noticed a persistent enhancement of the Brillouin return near the surface. The average enhancement for each flight varied from 30% to 50%, with an overall average of 41%. There are a number of reasons for an increased surface return in the total lidar return. These include specular reflections from surface wave facets normal to the incident beam, scattering from floating objects like foam or seaweed, and enhanced backscattering because of focusing by surface waves. Because the filter in the Brillouin channel will block specular reflections and scattering from floating objects, it seems that the explanation for the enhancement in that channel would be enhanced backscattering. This hypothesis is investigated here using a Monte-Carlo approach.

3.2.2. Monte-Carlo Model

The basic geometry of the problem is shown in Figure 3.10. Parallel rays are incident on the surface over some area. For this calculation, we used an array of 201 rays in each horizontal dimension on the surface. These were distributed over a region 7 m square to match the normal HSRL spot diameter of 7 m on the surface. The HSRL spot on the surface has a truncated circular Gaussian irradiance distribution. Our use of a square spot with uniform irradiance provides computational efficiency, with little loss of accuracy. Randomly generated realizations of the surface were generated for a Monte-Carlo calculation (Metropolis and Ulam, 1949). The slope of the surface at each ray intercept was used to calculate the refraction using Snell’s law, and the refracted rays were propagated into the water. At depth intervals of 0.2 m, the positions of all rays were calculated and the number of ray crossings were counted. In this case, two rays were assumed to cross if the distance between them was less than half of the initial ray separation.

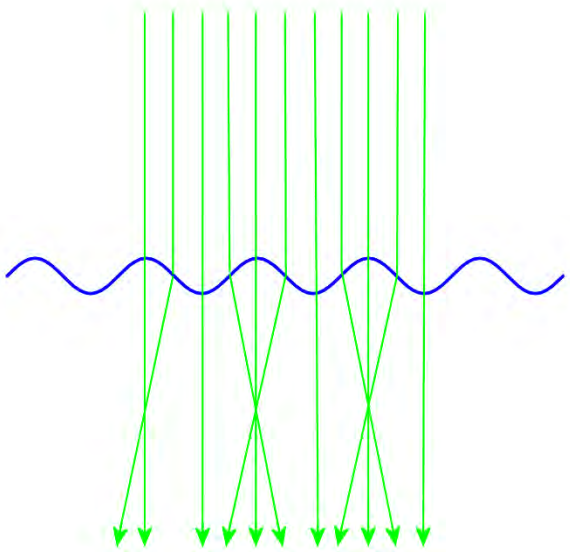

Figure 3.10. Schematic diagram of the lidar geometry of interest. Parallel rays (green) are incident on the wavy sea surface (blue). If the ray is not normal to the surface, it is refracted toward the normal.

We used a Gaussian approximation for the distribution of sea surface height (Cox and Munk, 1954; Shaw and Churnside, 1997). With this approximation, we could generate random realizations of the surface using Fourier components whose amplitudes were distributed according to the surface spectrum and whose phases were independent and uniformly distributed. Random realizations of the sea surface were generated using the Pierson–Moskowitz spectrum (Pierson and Moskowitz, 1964). The temporal spectrum has the form

$$S(\omega) = \frac{8.1\times10^{-3} g^2}{\omega^5} \exp\left[-0.74\left(\frac{\omega_0}{\omega}\right)^4\right], \tag{3.6}$$

where g is gravitational acceleration and ω_0 is $g/U_{19.5}$. The spectrum was developed using winds measured at a height of 19.5 m, $U_{19.5}$. Meteorological winds are more commonly measured at a height of 10 m, which can be approximated by $U = 0.975U_{19.5}$. The difference is small, but the simulations were made with this correction to wind speed. For each realization, 100 frequencies were selected with equal spacing between 0.8 to 80 rad s^{-1}. The amplitude of each was set equal to the square root of the spectral value, and the phase of each was randomly chosen between 0 and 2π. The wavenumber, k, corresponding to each frequency was calculated from the dispersion relation for surface waves in deep water, $\omega^2 = gk$. The propagation direction for each spectral component was randomly chosen between 0 and 2π. A typical realization (Figure 3.11) shows that the surface characteristics are dominated by longer waves, as expected.

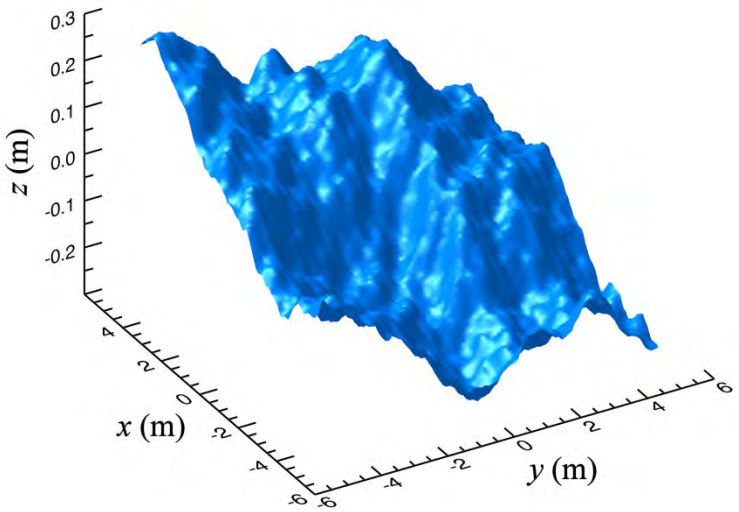

Figure 3.11. Example of a sea surface with a Pierson–Moskowitz spectrum for a wind speed of 5 m s^{-1}. Root-mean-square slope at this wind speed was about 9°.

This model of the sea surface was chosen for its relative simplicity, and does not account for the directionality of the actual wave field or the effects of wave age or fetch. There are other surface models that provide a more accurate description of the sea surface (Donelan and Pierson, 1987; Elfouhaily *et al.*, 1997; Hasselmann *et al.*, 1980), but the details are not important for our purpose. What is important is the probability distribution of surface slopes. Cox and Munk (Cox and Munk, 1954) measured the mean-square surface slope for near-neutral atmospheric stability and obtained a linear dependence on wind speed given by

$$mss_{CM} = 5.08\times10^{-3}U + 3\times10^{-3}. \tag{3.7}$$

We measured the mean-square slope for 100 realizations of our surface model for wind speeds from 1 to 20 m s^{-1}, and performed a linear regression against wind speed with the result

$$mss_{PM} = 2.06\times10^{-3}U + 5.4\times10^{-5}. \tag{3.8}$$

The conclusion is that the model accurately represents surface slopes.

The backscattering enhancement can be derived from the number of crossing rays. If two rays do not cross, the intensities at the receiver add directly. Light goes into the water along a ray path and returns along the same ray path, so the total intensity for an N by N array of initial rays is proportional to N^2. If two rays cross, there are two additional ray paths between the transmitter and receiver. Light that goes into the water along Ray 1 can return along Ray 1, but additional scattered light can also return to the receiver along Ray 2. Similarly light that goes into the water along Ray 2 can return along Ray 2 and additional light can return along Ray 1. Since these two additional ray paths between the transmitter and receiver are exactly the same length, the fields

add coherently, so the total intensity is proportional to $N^2 + 2N_x$, where N_x is the number of rays that intersect at a particular depth. The enhancement factor is $2N_x/N^2$.

We performed the calculation for several wind speeds between 1 and 20 m s^{-1}. For each wind speed, we used three independent realizations of the surface, using 100 wavelengths between 1 cm and 96 m. For each realization, we used a rectangular grid of 201 by 201 rays. These were propagated into the ocean in depth increments of 20 cm down to a depth of 4 m. Two rays were assumed to intercept if their separation at any depth was less than half of the initial separation.

3.2.3. Results

Since the enhancement depends of focusing by surface waves, it is zero at the surface. The left panel in Figure 3.12 shows the regular array of ray positions at the surface from -3.5 m to 3.5 m in both X and Y dimensions. As the rays propagate through the water, however, they are focused and defocused by surface waves. The right panel shows the ray positions at a depth of 0.8 m for a particular realization of the surface heights at a wind speed of 3 m s^{-1}. The random density of ray positions is clearly visible in this figure.

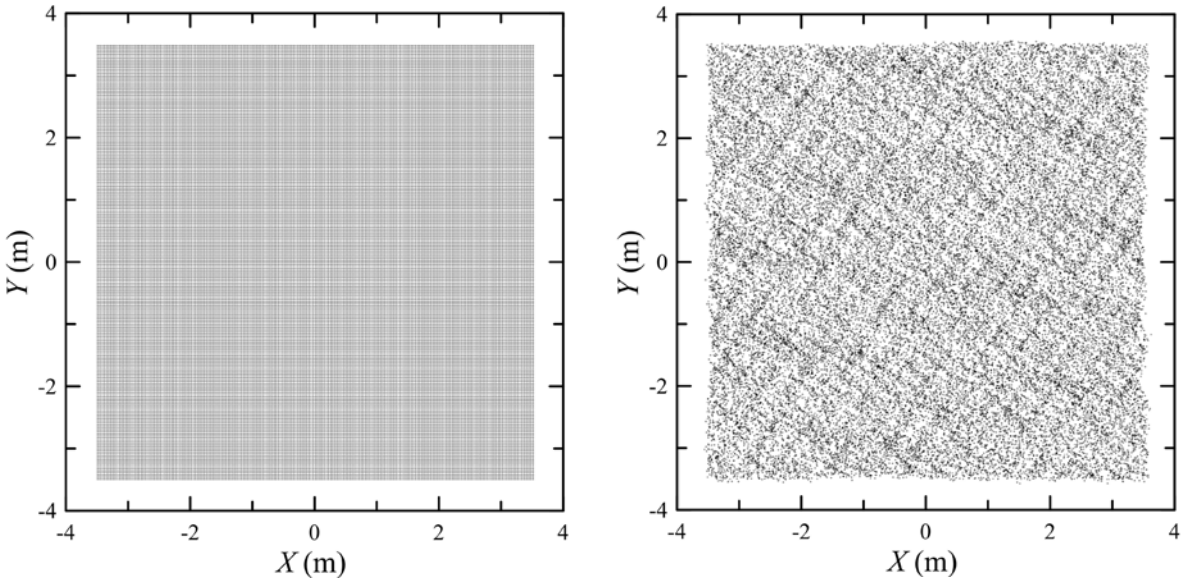

Figure 3.12. Ray positions at the surface (left panel) and at a depth of 0.8 m (right panel) for a particular realization of the surface heights.

The enhancement as a function of depth is plotted in Fig. 3.13. The peak enhancement is at 0.8 m. This was the case for all wind speeds considered. The average peak enhancement for all flights was 0.32, with no significant dependence on wind speed. This is a feature of the spectrum in Eq. (3.6). If $\omega > g/U$, the exponential will be nearly unity, and the spectrum does not depend strongly on U. From the dispersion relationship of surface waves, the condition that $\omega > g/U$ is equivalent to the condition that the surface wavelength, $\Lambda < 2\pi U^2/g$. Because surface waves

longer than the lidar spot diameter of 7 m tend to tilt the light with little focusing, we do not expect much dependence on wind speed for winds above about 3 m s^{-1}.

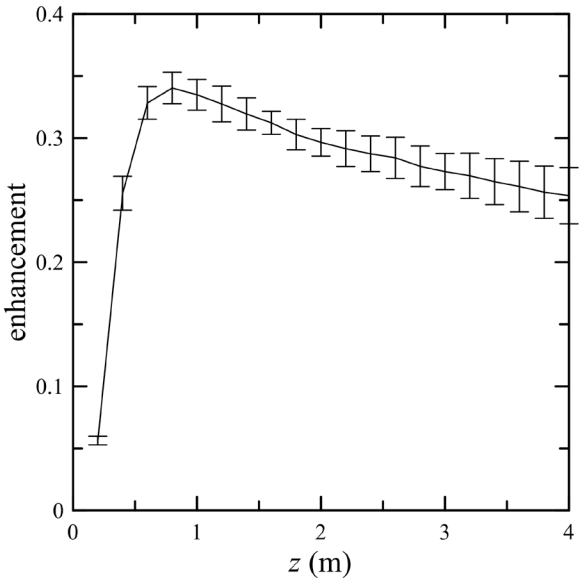

Figure 3.13. Enhancement factor as a function of depth, *z*, from a Monte-Carlo calculation with wind speed of 3 m s^{-1}. Error bars represent the standard deviation of three Monte-Carlo runs.

The average enhancement of 32% in this calculation is less than the observed value of 41%, but close enough that we believe that this is, in fact, the source of the observed enhancement. The difference is likely to the simplified model used in the calculation. In particular, the result is sensitive to the way we have defined intercepting rays. A more accurate calculation would use a much denser ray field, but this increases the calculation time to unacceptable levels.

3.2.4. Conclusions

Despite its simplicity, the Monte-Carlo calculation produced an average near-surface enhancement that was only 22% different from the observed value, so we conclude that the observed enhancement is probably caused by focusing by surface waves.

4. NOAA Oceanographic Lidar Data

4.1. Introduction

The climate of the Arctic is rapidly changing as a result of several amplifying feedback mechanisms (Pithan and Mauritsen, 2014; Serreze and Barry, 2011; Taylor *et al.*, 2013). These include decreases in surface albedo, increases in cloud cover, and increased atmospheric transport from the south. The largest factor in determining surface albedo is sea ice, which has been shrinking in extent, getting thinner, and drifting more rapidly (Comiso, 2011; Kwok and Rothrock, 2009; Spreen *et al.*, 2011; Vaughan *et al.*, 2013). In turn, the reduction in sea ice affects the timing and distribution of phytoplankton. Satellite observations suggest that the

primary productivity of the Arctic Ocean is increasing as the area of open water and the growing season increase (Arrigo and van Dijken, 2015; Arrigo *et al.*, 2008). In addition, thinning ice with more melt ponds allows increased primary productivity under the ice (Arrigo *et al.*, 2014).

Sub-surface phytoplankton layers are common in the Arctic Ocean in summer (Ardyna *et al.*, 2013; Cota *et al.*, 1996; Coupel *et al.*, 2011). As nutrients are depleted at the surface, a plankton layer develops at the pycnocline formed by melting ice (Brown *et al.*, 2015; Hill and Cota, 2005; Martin *et al.*, 2010; Naoya *et al.*, 2018). While the depth of these layers is generally consistent with measured pycnocline depths, some can be much deeper. Brown reported depths ranging from 3-106 m, but with a mode of 15-20 m in July. This is consistent with a previous suggestion that there might be shallow layers associated with the pycnocline, but also deep layers that might be associated with the deeper nutricline (Churnside and Marchbanks, 2015; Martin *et al.*, 2013). While this work is all in the Arctic Ocean, we should note that thin plankton layers associated with a salinity-driven pycnocline has also been observed in Magellan Strait in the south (Ríos *et al.*, 2016).

Subsurface plankton layers affect primary productivity. In the northern Barents Sea, productivity in the subsurface plankton layer was measured to be similar to that during the spring bloom (Hegseth, 1998). In the central North Sea, 58% of the total column productivity in August was in a subsurface plankton layer, and 37% of the annual average was in this layer (Weston *et al.*, 2005; 2011). Measurements in the Beaufort Sea found 55% of the productivity in the subsurface layer (Retamal *et al.*, 2008), and models suggest that 35-90% of the coastal productivity in the Beaufort Sea is within the subsurface layer (Martin *et al.*, 2013). A comparison of 32 models found that the models generally performed better in regions where there was no subsurface layer (Lee *et al.*, 2015). It has been noted that models often overestimate primary production, and this can compensate for not including production of the subsurface layer, resulting in an overall estimate that might be better than expected (Arrigo *et al.*, 2011; Lee *et al.*, 2015). In fact, column integrated productivity can be negatively correlated with surface chlorophyll, because low surface chlorophyll is often associated with a subsurface chlorophyll layer with high productivity (Jacox *et al.*, 2015).

Within the Arctic Ocean, Barrow Canyon is a region that has received a lot of attention. Much of the water flowing northward through Bering Strait passes through the canyon, especially in summer. Summertime estimates range from 50% (Stabeno *et al.*, 2018) to 80% (Gong and Pickart, 2015), and an annual average of 55% has been reported (Itoh *et al.*, 2013). With this influx of water from the south, Barrow Canyon is also a biologically active, and has been designated as one of eight regions of the Distributed Biological Observatory to detect changes in the Arctic Ocean (Grebmeier *et al.*, 2010; Moore and Grebmeier, 2018). Flow through the canyon might also be expected to generate turbulent mixing, and a direct measurement of turbulent kinetic energy dissipation near the head of the canyon along the 70 m isobaths on the northern side showed elevated levels near the pycnocline and also within the boundary layer near the bottom (Shroyer *et al.*, 2014).

There have been a number of investigations of plankton using lidar (Churnside, 2014; Churnside and Ostrovsky, 2005; Churnside and Donaghay, 2009; Churnside *et al.*, 2012), but few in the Arctic. Hill and Zimmerman (Hill and Zimmerman, 2010) used model results to show that primary production estimates in the Arctic could be improved with lidar. Goldin et al. (Goldin *et al.*, 2007) used an airborne lidar to detect subsurface layers in the Barents Sea in August of 2003. We used a similar lidar to provide more details of the structure of subsurface layers in the Chukchi and Beaufort Seas in 2014 (Churnside and Marchbanks, 2015). Beherenfeld *et al.* (Behrenfeld *et al.*, 2016) estimated phytoplankton biomass in the Arctic using the depth-integrated return from a space-based lidar that lacks depth resolution required for profiling. That same lidar has been used to detect sea ice (Lu *et al.*, 2017).

In this paper, we report the results of lidar surveys in 2017 and compare these with our 2014 results. The survey periods were the same for the two years, but the ice conditions were very different.

4.2. Materials and Methods

The study area and period of investigation were the same as in 2014, except that the flight locations were adjusted in response to the different ice conditions. Fig. 4.1 shows the flight tracks for the two years, along with the ice extent at the beginning (July 15) and end (July 31) of the study. The platform was a NOAA Twin Otter flying at 300 m altitude at a speed of about 60 m s^{-1}. Ice extent values are from satellite-derived maps of marginal ice zone from the US National Ice Center. These are provided for context, and were not used in the analysis. Additionally, daily ice extent values were obtained from the National Snow and Ice Data Center (Fetterer *et al.*, 2010) and averaged over the period July 15-31 for each year.

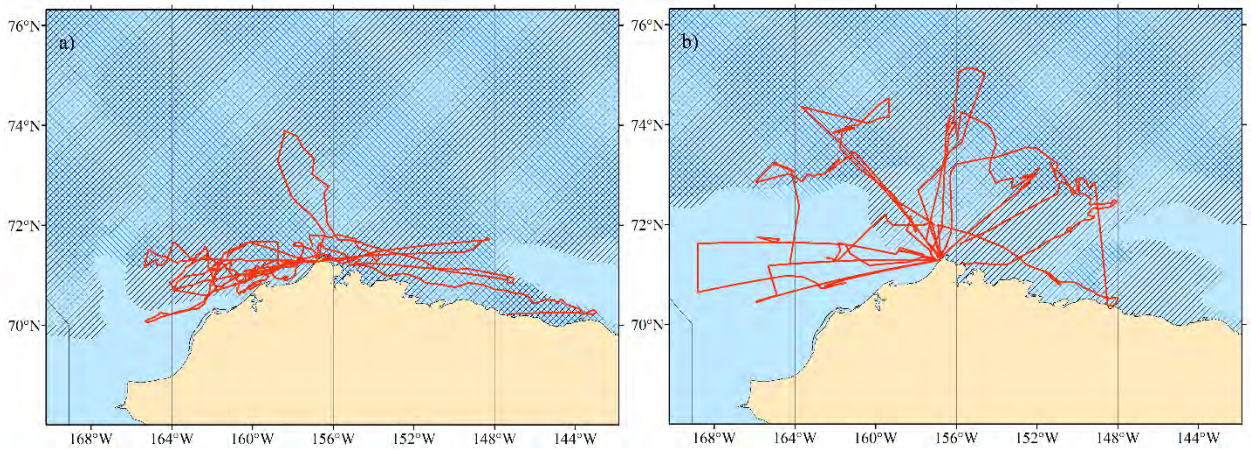

Figure 4.1. Map of study area near northern Alaska in **a)** July 2014 and **b)** July 2017. Black /// denotes the area covered by ice on July 15, and blue \\\ denotes the area covered by ice on July 31 of each year. Red lines are the aircraft flight tracks.

The primary instrument for this investigation, as in 2014, was the NOAA airborne oceanographic lidar. This lidar transmitted 12 ns pulses of linearly polarized green (532 nm) light at a rate of 30 Hz. Two receiver channels detected the co- and cross-polarized light scattered from the ocean with a 1 GHz sample rate. Processing of the lidar data to obtain layer parameters used the same technique as before, which has been described in more detail in a recent publication (Churnside and Marchbanks, 2017). Fractional ice cover was also obtained from the lidar, based in the fraction of pulses in each kilometer of flight track where the surface return saturated the detector.

To investigate turbulent mixing in Barrow Canyon, five transects of the canyon were selected (Fig. 4.2). Bathymetric data were obtained from the International Bathymetric Chart of the Arctic Ocean (IBCAO) Version 3.0 (Jakobsson *et al.*, 2012), and the flight segment where the depth is greater than 70 m was used to define the canyon. The power spectral density (*psd*) of the lidar return from depths of 10 m and 20 m were calculated. A linear regression of the logarithm of the *psd* to the logarithm of spatial wavenumber was calculated for each pass at each of the two depths.

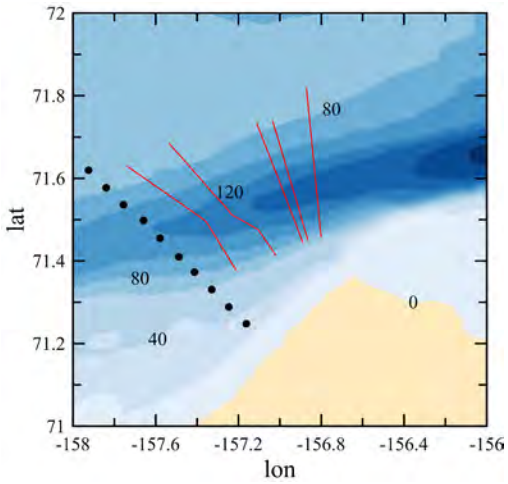

Figure 4.2. Map of region near Point Barrow, Alaska, with bathymetry denoted by color scale at depth intervals of 20 m. Flight segments are denoted by red lines, and ship stations by black circles.

Water density profiles were measured at 71.219° N, 164.257° W using the NOAA PRAWLER (PRofiling crAWLER) (Osse *et al.*, 2015; Tabisola *et al.*, 2017). This instrument provided CTD (Conductivity Temperature Depth) profiles at three hour intervals beginning July 29, 2017, and data through August 5, 2017 were considered in the analysis. For each profile, density was calculated from temperature and salinity, and the depth where the derivative of density with depth was maximum (maximum Brunt-Väisälä frequency) was used as a measure of the mixed layer depth (Bourgain and Gascard, 2011). Lidar flights came within 50 km of this mooring on three days, July 22, 26, and 28, 2017.

Water density was also measured by CTD cast from the USCGC *Healy* at 71.223° N, 164.262° W on July 29, 2017 and 72.473° N, 156.567° W on August 3, 2017. The first position was within 500 m of the PRAWLER position. Lidar flights came within 50 km of the second position on July 18, 27, and 29, 2017.

We also have CTD casts from 10 positions across Barrow Canyon (Fig. 1) measured on July 21 and 22, 2017 from the CCGS *Sir Wilfrid Laurier*. In addition to calculating mixed layer depths for these casts, we calculated the positions of various water masses across the canyon according to the classifications of Gong and Pickard (Gong and Pickart, 2015). During the same period, a 150 kHz Acoustic Doppler Current Profiler (ADCP) was operated from the ship. The ship made four passes along the CTD line in Fig. 1, and we calculated the power spectral density of the acoustic backscatter at three depths – 11, 19, and 39 m.

Large-scale winds were obtained from the National Centers for Environmental Prediction (NCEP) North American Regional Reanalysis (Kalnay *et al.*, 1996). These were averaged over the period of the flights (July 15-31) for each year. Only values over water and between 170° and 168° W longitude were used in the analysis. This roughly corresponds to the longitudinal extent of the Bering Strait.

The Bakun upwelling index (Bakun, 1973; 1990) was calculated using the hourly wind speed and direction at the Wiley Post-Will Rogers Memorial Airport in Utqiaġvik, Alaska. For this calculation, a value of 34° from the east-west direction was used for the orientation of the coastline. This is the angle of a line from Point Barrow to Point Hope along the NW coast of Alaska.

4.3. Results

As Fig. 4.1 shows, the ice conditions were very different in the latter half of July in the two years, and this difference shows up in survey conditions (Fig. 4.3). The surveys in 2017 were much more likely to be over open water (ice fraction < 0.1), less likely to be over broken ice, and slightly more likely to be over complete ice cover (ice fraction > 0.9).

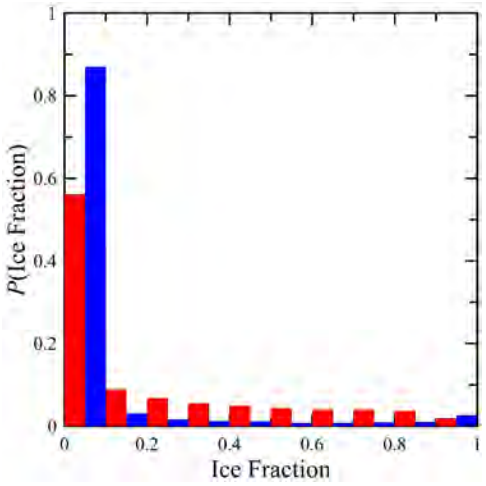

Figure 4.3. Probability of encountering a given fractional ice cover in increments of 0.1 for 2014 (red) and 2017 (blue).

The probability of encountering a subsurface plankton layer in 2017 was greater than in 2014, except in open water (Fig. 4.4). For 2014, the Pearson correlation between ice fraction and layer probability was R = -0.72 (p = 0.02). Without the open water value, the correlation was much higher, with R = -0.96 ($p < 10^{-4}$). For 2017, the correlation was much higher when all values were used, with R = -0.91 ($p < 0.001$). Without the open water point, the correlation was slightly less than in 2014, with R = -0.92 ($p < 0.001$).

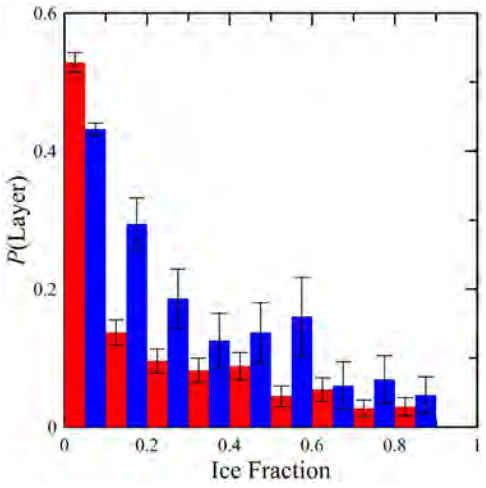

Figure 4.4. Probability of encountering a subsurface layer as a function of ice fraction for 2014 (red) and 2017 (blue). Error bars represent ±1 standard deviation of the values.

The mean characteristics of the layers for both years are listed in Table 4.1, including a column for layers south of 72° N. This area, where most of the 2014 surveys took place, was almost entirely open water in 2017. The most notable feature is the difference in layer strength; the average and median strength of the layers was much weaker in 2017 than 2014. For both years, layers in open water were stronger than those in broken ice. Open water layers south of

72° were stronger than the overall average, but still only about half as strong as open water layers in 2014. Average layer depths were about the same for both years, with open water layers slightly deeper than those in broken ice. Layers in 2017 were thinner than those in 2014, with little difference between open water and ice in either year.

Table 4.1. Strength (average, standard deviation, and median), average and standard deviation depth, and average and standard deviation thickness for layers identified in 2014 and 2017. Columns present values for open water and broken ice for each year and open water south of 72° N for 2017.

2014:	Open Water	Ice > 0.1	2017:	Open Water	Ice > 0.1	S of 72°
Strength	27.0 ± 44.7	8.9 ± 14.0		10.7 ± 48.9	4.1 ± 5.6	13.4 ± 55.3
Median	12	5.1		2.6	2.2	3.0
Depth (m)	19.6 ± 6.0	15.6 ± 6.2		18.5 ± 8.1	15.5 ± 7.0	20.1 ± 8.2
Thickness (m)	3.8 ± 1.5	3.4 ± 2.0		2.4 ± 1.6	2.8 ± 1.7	2.3 ± 1.6

The average depth of layers within 50 km of the PRAWLER was 27.0 m with a standard deviation of 8.8 m. The average depth of the mixed layer inferred from the PRAWLER data was 25.6 m with a standard deviation of 1.7 m. The difference in the average depths, 1.4 m, is about 13% of the combined standard deviations.

The mixed layer depths inferred from the two ship-based casts were 23 m and 29 m. Note that the first cast was within 500 m of the PRAWLER, so the average depth of the layers observed by the lidar within 50 km of the cast is the same as for the PRAWLER, 27.0 ± 8.8 m. For the other cast, the average layer depth was 16.2 ± 8.1 m, which is well below the mixed layer depth of 29 m inferred from the CTD cast. However, there was a second jump in density at about 14 m, which is much closer to the average layer depth. The Brunt-Väisälä frequency at this depth was 0.041 s^{-1}, which is not far from the peak value of 0.053 s^{-1} at 29 m.

The average mixed layer depth across the Barrow Canyon casts was 11.9 m, with a standard deviation of 4.0 m. Stratification was weak, with the mean of the peak Brunt-Väisälä frequency only 5.4×10^{-3} s^{-1} and the standard deviation 3.1×10^{-3} s^{-1}. The average depth of layers across the five lidar transects of the canyon was 17.8 m, with a standard deviation of 7.4 m. The layers were also weak, with a mean and standard deviation of 1.98 ± 1.06 times the background scattering level. Both depth and strength of layers decreased with decreasing distance from the mouth of the canyon.

The water masses calculated from the CTD casts across Barrow Canyon (Fig. 4.5) show three types. Alaska Coastal Water (ACW), warm and salty, covered the surface and extended to the bottom on the south side of the canyon. Pacific Winter Water (PWW), cold and salty, was below 30 m on the north side of the canyon. Chukchi Summer Water (CSW), with intermediate temperature and salinity, was found primarily in a layer around 25 m on the north side of the canyon and to the bottom in the deepest part of the canyon.

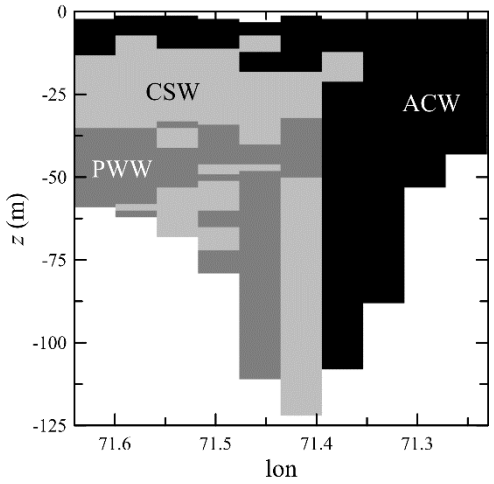

Figure 4.5. Distribution of Gong-Pickard water masses across Barrow Canyon. Colors represent Alaska Coastal Water (ACW, black), Pacific Winter Water (PWW, dark gray), and Chukchi Summer Water (CSW, light gray).

The power spectral density of the fluctuations in lidar signal were very close to a power law with exponent of -5/3 for all five passes over Barrow Canyon and for both depths. A typical spectrum (Fig. 4.6) clearly shows a power-law shape until the lidar noise limit is reached at high wavenumbers. For this case, the fit was performed up to a wavenumber of 40 km^{-1}, and the exponent of -1.70 is within 2% of the expected value.

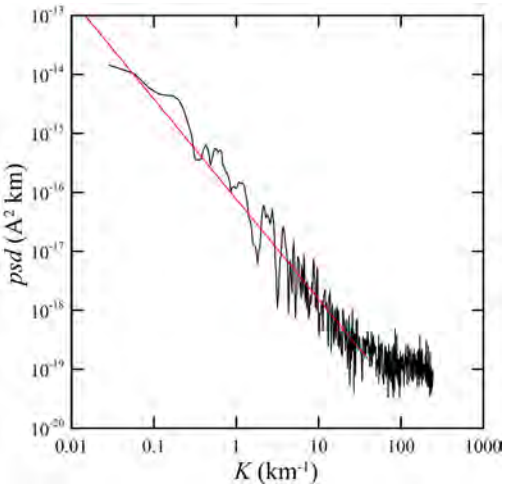

Figure 4.6. Power spectral density, *psd*, as a function of wavenumber, *K*, for lidar data collected at 10 m depth on July 28, 2017. Red line is the result of a linear regression from the first value to 40 km^{-1}.

The characteristics of power spectral density for the five passes and two depths are presented in Table 4.2, along with the Bakun upwelling index estimated from Utqiaġvik winds. The correlation between upwelling and turbulence level was 0.91 (P = 0.03) at 10 m and 0.88 (P = 0.05) at 20 m. During periods of downwelling (negative index), turbulence levels were all below 10^{-17} and the difference between the level at the two depths were 10% or less of the 10 m value.

During upwelling conditions, turbulence levels were higher (> 10^{-17}) and the difference was 60% and higher.

Table 4.2. Line number (from west to east in Fig. 4.2), date (July) of the measurement, Bakun upwelling index (m^3 s^{-1} per 100 m of coastline), turbulence level, T (A^2 km) at 10 m and 20 m depths, and the percent difference between them.

Line (W to E)	Date	Upwelling	T_{10}	T_{20}	Difference (%)
1	21	-177	7.96×10^{-18}	7.45×10^{-18}	6
2	28	58	1.12×10^{-16}	4.50×10^{-17}	60
3	29	-509	3.43×10^{-18}	3.08×10^{-18}	10
4	31	-310	2.95×10^{-18}	3.11×10^{-18}	5
5	18	64	4.09×10^{-17}	1.31×10^{-17}	68

The acoustic spectra (Fig. 4.7) are very similar to the lidar spectra; a power law with slope near -5/3 and a nearly white noise floor at high wavenumbers. For the case presented, the slope of -1.68 was within 1% of the expected value out to a wavenumber of 20 km^{-1}. These data were collected over too short a time period to investigate the effects of upwelling on turbulence level, but we did find a significant increase of turbulence with depth (R = 0.76, P = 0.005) over the three depths investigated.

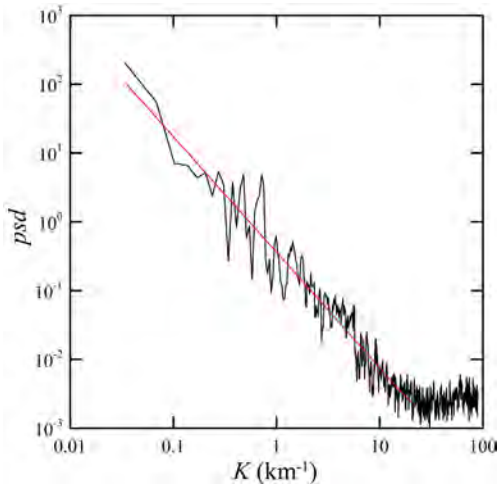

Figure 4.7. Power spectral density, *psd*, as a function of wavenumber, *K*, for acoustic data collected at 39 m depth on July 22, 2017. Red line is the result of a linear regression from the first value to 20 km^{-1}.

4.4. Discussion

Much of the difference in ice cover can be explained by a difference in winds. In 2014, the mean value of the NCEP reanalysis southerly wind component was 0.75 m s^{-1} from Bering Strait to 80° N. To the north of 75°, the average wind was out of the north. In 2017, the same average southerly wind component was 2.4 m s^{-1} and the direction was within 45° of south over the entire latitude range. From these differences, we would expect the ice to be pushed farther north in

2017. We would also expect individual floes to be pushed together resulting in smaller areas with partial ice cover and more areas with almost complete ice cover. These features are consistent with the differences seen in Fig. 3. This is also consistent with visual observations of areas of complete ice cover from the aircraft; in 2014, these areas appeared to be mostly solid ice, while in 2017, they appeared to be mostly closely packed ice floes. The change in ice conditions seems less likely to be related to global changes. For the northern hemisphere, the average ice extent over the last half of July only decreased by 1.5% from 2014 to 2017, while the corresponding decrease in the Chukchi Sea was 20% (Fetterer *et al.*, 2010).

For both years, an exponential model for the relationship between ice fraction and the probability of encountering a subsurface plankton layer explained most of the variance in the latter. Within the region of broken ice (fraction > 0.1), $R^2 = 0.90$ in 2014 and 0.86 in 2017 for this model. The rate of decay for the two years was very similar, although the overall levels were different. In general, $P_L = A\exp(-2.32F_I)$, where P_L is the probability of a layer and F_I is the ice fraction. The difference in the coefficient of F_I between the two years was about 5% of the reported mean value. The constant, A was 0.18 in 2014 and twice as large (0.37) in 2017. It is not clear why so much of the variability would be explained by ice fraction. One possibility is lower light levels under ice.

The biggest difference in layer properties between the two years was the layer strength in both open water and in broken ice. Because the layer strength is defined as the ratio of the layer signal to the background, this difference could be because the layers were less dense in 2017, the background density was greater, or some combination of both. To answer this question, we used chlorophyll concentration composites for the month of July in each year from the Visible and Infrared Imager/Radiometer Suite (VIIRS). For pixels (at 4 km resolution) in US Arctic waters with data for both years, the average increase in surface chlorophyll concentration was 72%. The change in layer strength in the area south of 72° N was 50%, suggesting that much of the difference was caused by an increase in background levels, coupled with a smaller decrease in density within the layers.

The average depths of layers in open water and in broken ice were nearly the same for both years, and, in both cases, slightly deeper in open water. In 2017, the depths agreed with available measurements of pycnocline depth to within the variability of the measurements. In general, layer depths were slightly greater than pycnocline depth, however. Our depths are also consistent with *in situ* measurements of layer depths that range from 15-25 m (Brown *et al.*, 2015; Coupel *et al.*, 2011; Hill and Cota, 2005).

The average layer thickness was slightly less in 2017 than in 2014. This difference may also be at least partially explained by the difference in winds. A model of layer thickness based on current shear predicts a minimum thickness of (Birch *et al.*, 2008)

$$t = 2.4\alpha^{-1/3}\kappa_\upsilon^{1/3}L_0^{1/3}, \tag{4.1}$$

where α is vertical current shear, κ_v is the vertical diffusivity of plankton, and L_0 is the initial horizontal extent of the plankton patch before thinning by shear. In this simple model, the initial vertical extent does not matter. The factor of 2.4 is the result of converting from a Gaussian radius to full width at half maximum. Using typical parameters from Birch et al, the predicted minimum thickness is about what we observed in 2017. The thicker layers in 2014 could be explained by a current shear of about one fourth of the 2017 values. The weaker winds in 2014 would likely produce lower surface drift currents and less shear, although quantitative estimates of the difference are beyond the scope of this paper.

Except at the very limit of depth penetration, the lidar measurements in Barrow Canyon were made in either Alaska Coastal Water or Chukchi Summer Water. This is consistent with previous measurements of water masses in Barrow Canyon in summer, although some authors used different identifiers and different parameter ranges (Coachman and Barnes, 1961; Crawford *et al.*, 2012; Weingartner *et al.*, 1998). Therefore, it is mixing of these two water masses that provides the turbulence observed by the lidar and the ADCP at the two shallower depths. At 40 m, the ADCP is also influenced by Pacific Winter Water.

Turbulent mixing of phytoplankton in Barrow Canyon is enhanced by wind-driven upwelling. Another hypothesis, that tidal currents might be a factor, was not considered, because tidal currents are very small (Itoh *et al.*, 2013; Mountain *et al.*, 1976). We also observed that measured turbulence levels were higher at 10 m than at 20 during upwelling, but nearly the same during downwelling conditions. The mechanism is probably related to advection of surface water from near shore, where phytoplankton concentrations are higher, across the canyon during upwelling. This would create a high vertical gradient near the surface, which would be mixed downward by turbulence. The resulting turbulent mixing observed by the lidar would be high near the surface and decrease with depth under these conditions.

While the lidar return is dominated by phytoplankton (Churnside and Thorne, 2005), the ADCP return is mostly from zooplankton (Flagg and Smith, 1989; Ressler, 2002). This might explain why the turbulence levels observed by the ADCP increase with increasing depth. Zooplankton can be detected by lidar (Churnside and Thorne, 2005), but the required processing reduces the signal to noise ratio, and it was not possible to obtain clear spectra of the zooplankton return.

For a passive scalar quantity, θ, the turbulence level defined above is given by (Sreenivasan, 1996)

$$T = C_\theta \langle \varepsilon \rangle^{-1/3} \langle \chi_\theta \rangle, \tag{4.2}$$

where C_θ is the Obukhov-Corrsin constant (~0.4), $\langle \varepsilon \rangle$ is the mean energy dissipation rate, and the dissipation rate of the variance of the scalar is given by

$$\left\langle \chi_\theta \right\rangle = 2\kappa_\upsilon \left\langle |\nabla \theta|^2 \right\rangle, \quad (4.3)$$

where κ_v is the scalar diffusivity and $\nabla\theta$ is the scalar gradient. This suggests that the difference in the vertical distribution of turbulence level observed by the lidar and the ADCP is because of differences in the vertical distribution of gradients of phytoplankton and zooplankton.

4.5. Conclusions

Ice conditions were very different in the study area in July of 2014 and 2017, but the characteristics of subsurface plankton layers and their dependence on ice cover were similar for the two years. In both years, the prevalence of subsurface plankton layers exponentially decreased with increasing ice cover. The average depths were similar for both years, with layers in open water deeper than those in the pack ice. The depths of subsurface plankton layers were consistent with the mixed layer depth in areas where in situ density profiles were available. A noticeable difference in layer strength relative to the background water was likely caused by higher background phytoplankton concentrations in 2017. Differences in layer thickness were observed, which could be the result of higher current shears in 2017.

Turbulent mixing of phytoplankton and zooplankton in Barrow Canyon was inferred from the power spectral density of lidar and acoustic scattering. Lidar measurements suggested that the level of turbulence and its vertical distribution were affected by local upwelling winds. The vertical distribution of acoustic scattering was different from that of the lidar, which we interpret as different vertical distributions of phytoplankton and zooplankton gradients.

5. Data Sets

5.1. CALIOP

Datasets including total and perpendicular attenuated backscatter profiles (km^{-1} sr^{-1}), β_{total} and β_{perp}, wind speed (m s^{-1}), v, downwelling diffuse attenuation coefficient at 490 nm (m^{-1}), K_d, and hemispheric backscattering coefficient (m^{-1}), b_{bp}, were compiled for three locations. These include two in the Pacific Ocean: 50° N latitude and 145° W longitude, and 22° N latitude and 158° W longitude, and one in the Atlantic Ocean: 61° N latitude, 26° W longitude. A fourth set, differing in spatial area, was compiled for the Arctic region centered on 68° N latitude and -170° W longitude, including Chukchi Sea. Selected using three criteria, calibrated and geolocated profiles of β_{total} and β_{perp} (0.05 second and 333 m resolution) were averaged monthly in time and spatially to 5° latitude by 5° longitude grid. Once averaged, β_{total} and β_{perp} were corrected for the transient detector response using a deconvolution technique and a profile estimating this effect.

The CALIOP β_{total} and β_{perp} profiles were treated using three criteria. First, only night time designated half orbit, geolocated profiles were interrogated. Next, the maximum β_{total} value as determined from 5 near surface range bins must be $\beta_{total} > 0.1$ km^{-1} sr^{-1}. Finally, β_{total} and β_{perp}

profiles were used to compute a profile of depolarization ratio, where δ_{surf} was evaluated. Profiles meeting δ_{surf} criteria were included, $\delta_{surf} < 0.01$ for three locations: Ocean Station Papa, North Atlantic and Arctic, and $\delta_{surf} < 0.005$ for the Hawaiian location.

Monthly means of near surface wind speed provided at 2.5° latitude by 2.5° longitude were also gridded to 5° latitude by 5° longitude. The 4 km product of monthly diffuse attenuation coefficients, K_d, as retrieved by satellite, were also averaged spatially to the 5° latitude by 5° longitude grid. Additionally, the 4 km MODIS product b_{bp} at 443 nm was also spatially averaged to the the 5° latitude by 5° longitude grid.

5.2. NASA HSRL

The full SABOR data set is available from NASA Langley Research Center, but a reduced set of profiles of optical parameters was generated as part of this project. There is a file for each flight. Each file contains longitude (lon, decimal degrees), latitude (lat, decimal degrees), depth (z, m) and mean and standard deviations over 100 profiles of diffuse attenuation coefficient (K_d, m^{-1}) and volume backscatter coefficient (β m^{-1} sr^{-1}). These quantities are included both for the HSRL and perturbation techniques.

5.3. NOAA Oceanographic Lidar

The NOAA data set produced for this project includes the near-surface optical properties for the Arctic flights conducted in July, 2017. Data were processed using a linear regression of the log of photocathode current with depth over the depth range of 5-10 m. For the lidar geometry used, the slope of the regression = $-2K_d$, and this relationship was used to obtain the diffuse attenuation coefficient, K_d. The intercept of the regression provides an estimate of the attenuation corrected photocathode current near the surface. This was converted to volume scattering function value from the lidar equation

$$I = \frac{EAT_O T_S^2 \eta c}{2n^3 H^2} \beta(\pi), \tag{5.1}$$

where E is the laser pulse energy (100 mJ), A is the receiver telescope area (2.83×10^{-3} m^2), T_O is the optics transmission (0.37), T_S is the sea-surface transmission (0.98), η is the responsivity of the photocathode (42 mA W^{-1}), c is the speed of light, n is the refractive index of sea water (1.33), and H is the aircraft altitude (300 m). Using the values in parentheses, we have

$$\beta(\pi) = 334I. \tag{5.2}$$

The scattering phase function from seawater is well known, with

$$\beta_w(\pi) = 0.1142 b_w, \tag{5.3}$$

where b_w is the scattering coefficient of seawater. The scattering from seawater depends on wavelength and, to a certain extent, on temperature and salinity. We performed a fit to measurements at 546 nm made over a range of temperature, *T*, from 0-40°C and salinity, *S*, from 0-40 psu (Shifrin, 1988). At a wavelength of 532 nm, the result is

$$b_w = 1.64\times10^{-3} + 1.62\times10^{-5} S + 1.22\times10^{-6} T + 1.02\times10^{-7} TS. \quad (5.4)$$

Before converting from 546 nm to 532 nm, the fit was within about 1% of the measured values. The value doesn't change much with temperature and salinity, so we used average values for the top 10 m of the PRAWLER data, which were T = 5.94° and S = 31.9 psu. For these values, b_w = 2.18×10^{-3} m^{-1} and $\beta_w(\pi) = 2.49\times10^{-4}$ m^{-1} sr^{-1}. This value was subtracted from derived β values to get the particulate contribution.

The particulate volume scattering function can be related to the particulate backscattering coefficient, b_{bp}, by

$$b_{bp} = 2\pi\chi(\pi)\beta_p(\pi) = 2\pi(334I - 2.49\times10^{-4}), \quad (5.5)$$

where χ is related to the shape of the particulate phase function for scattering angles > 90°. There are few estimates of the shape parameter at 180°, but there have been measurements at 170°. These include values of χ = 0.62 ± 0.22 at a coastal site in the NW Atlantic (Boss and Pegau, 2001), χ = 0.69 ± 0.08 at a coastal site in the Black Sea (Chami *et al.*, 2006), and χ = 1.09 ± 0.06 at ten sites at coastal and open ocean locations (Sullivan and Twardowski, 2009). We have used $\chi(\pi)$ = 1.0 in creating the data set. This is within measured values and is easy to scale if a different value becomes more widely accepted.

Before averaging, several quality control tests were implemented. First, shots with ice on the surface were eliminated from the averaging, but the number of shots with ice was used to calculate the ice fraction within the averaging area. Shots where the regression did not provide a good fit to the data were eliminated. The specific requirement was that the sum of the squares of the residuals had to be less than 0.09 for the shot to be included. Then, files contaminated by clouds were removed by visual inspection of the raw data files. The remaining data were averaged over about 1 km of flight track, provided that there were at least five good shots after the quality control. Bathymetric data were obtained from the International Bathymetric Chart of the Arctic Ocean (IBCAO) Version 3.0 (Jakobsson *et al.*, 2012).

The data set contains one file for each day. The file name contains the July date of the data collection. Each file contains longitude (lon, decimal degrees), latitude (lat, decimal degrees), water depth (water_depth, m), diffuse attenuation coefficient (Kd, m^{-1}), its standard deviation (Kd_sd, m^{-1}), particulate backscatter coefficient (bbp, m^{-1}), ant its standard deviation (bbp_sd, m^{-1}).

6. Summary and Conclusions

The overall objective was to investigate the usefulness of lidar as a remote sensing technique to support EXPORTS objectives. The investigation concentrated on profiles of particulate backscattering, b_{bp}, especially the existence of subsurface phytoplankton layers not detected by ocean color remote sensing. The study used data from three different lidars [the NOAA airborne lidar, the NASA airborne HSRL, and the satellite cloud/aerosol lidar CALIOP] at five geographical areas [Ocean Station Papa, the region around the North Atlantic Bloom Experiment, Hawaiian Ocean Time Series (~23 N), mid-latitude western Atlantic (SABOR), and the Arctic]. The main conclusions were:

- CALIOP can detect subsurface layers under ideal conditions (clear water and deep layers), but not reliably enough to provide annual cycle, for example. The reasons are its poor depth resolution and long detector fall time.
- CALIOP can provide surface b_{bp} estimates that compare with MODIS estimates (R = 0.74 at OSP; 0.41 at HOTS; 0.81 at NABE; and 0.1 in the Arctic).
- The NOAA airborne lidar can detect subsurface layers. We found layers about half the time in open water in the US Arctic. The prevalence decreased exponentially with increasing ice cover. The mean depth was around 20 m.
- The NASA airborne lidar uses a self-calibrating technique, high spectral resolution lidar, that uses most of the return energy for the calibration. The b_{bp} error with HSRL was around 5% near the surface. The error using the same data, but without using the calibration channel was about 10%.
- A space-based oceanographic lidar would support studies like EXPORTS and monitor changes. The performance tradeoffs between HSRL and direct backscatter lidars have been quantified.

Acknowledgments:

Bathymetric data were obtained from NOAA, https://ngdc.noaa.gov/mgg/global/relief/ETOPO1/data/ice_surface/grid_registered/netcdf/ Downloaded on December 5, 2017

b_{bp} data were obtained from the NASA Goddard Space Flight Center, Ocean Ecology Laboratory, Ocean Biology Processing Group. Moderate-resolution Imaging Spectroradiometer (MODIS) Aqua Inherent Optical Properties Data; 2018 Reprocessing. NASA OB.DAAC, Greenbelt, MD, USA. doi: 10.5067/Aqua/MODIS/L3B/IOP/2018.
Accessed on 02/2018 and the NASA Goddard Space Flight Center, Ocean Ecology Laboratory, Ocean Biology Processing Group. Moderate-resolution Imaging Spectroradiometer (MODIS) Terra Inherent Optical Properties Data; 2018 Reprocessing. NASA OB.DAAC, Greenbelt, MD, USA. doi: 10.5067/Terra/MODIS/L3B/IOP/2018. Accessed on 02/2018

K_d data were obtained from the NASA Goddard Space Flight Center, Ocean Ecology Laboratory, Ocean Biology Processing Group. Moderate-resolution Imaging Spectroradiometer (MODIS) Aqua Downwelling Diffuse Attenuation Coefficient Data; 2018 Reprocessing. NASA OB.DAAC, Greenbelt, MD, USA. doi: 10.5067/Aqua/MODIS/L3B/KD/2018.
Accessed on 02//2018 and the NASA Goddard Space Flight Center, Ocean Ecology Laboratory, Ocean Biology Processing Group. Moderate-resolution Imaging Spectroradiometer (MODIS) Terra Downwelling Diffuse Attenuation Coefficient Data; 2018 Reprocessing. NASA OB.DAAC, Greenbelt, MD, USA. doi: 10.5067/Terra/MODIS/L3B/KD/2018.
Accessed on 02/2018 and the NASA Goddard Space Flight Center, Ocean Ecology Laboratory, Ocean Biology Processing Group. Visible and Infrared Imager/Radiometer Suite (VIIRS) Chlorophyll Data; 2018 Reprocessing. NASA OB.DAAC, Greenbelt, MD, USA. doi: 10.5067/NPP/VIIRS/L3B/CHL/2018.
Accessed on 09/18/2017

NCEP Reanalysis data provided by the NOAA/OAR/ESRL PSD, Boulder, Colorado, USA, from their Web site at https://www.esrl.noaa.gov/psd/

References

Ardyna, M., M. Babin, M. Gosselin, E. Devred, S. Bélanger, A. Matsuoka, and J. É. Tremblay (2013), Parameterization of vertical chlorophyll a in the Arctic Ocean: impact of the subsurface chlorophyll maximum on regional, seasonal, and annual primary production estimates, Biogeosciences, *10*(6), 4383-4404. doi:10.5194/bg-10-4383-2013

Arrigo, K. R., and G. L. van Dijken (2015), Continued increases in Arctic Ocean primary production, Prog. Oceanogr., *136*, 60-70. doi:http://dx.doi.org/10.1016/j.pocean.2015.05.002

Arrigo, K. R., G. van Dijken, and S. Pabi (2008), Impact of a shrinking Arctic ice cover on marine primary production, Geophys. Res. Lett., *35*(19), L19603. doi:10.1029/2008gl035028

Arrigo, K. R., P. A. Matrai, and G. L. van Dijken (2011), Primary productivity in the Arctic Ocean: Impacts of complex optical properties and subsurface chlorophyll maxima on large-scale estimates, J. Geophys. Res. Oceans, *116*(C11), C11022. doi:10.1029/2011jc007273

Arrigo, K. R., et al. (2014), Phytoplankton blooms beneath the sea ice in the Chukchi sea, Deep Sea Res. II, *105*, 1-16. doi:10.1016/j.dsr2.2014.03.018

Bakun, A. (1973), Coastal Upwelling Indices, West Coast of North America, 1946-71, *NOAA Technical Report Rep. NMFS SSRF-693*, 103 pp, U.S. Department of Commerce, Seattle, Washington.

Bakun, A. (1990), Global Climate Change and Intensification of Coastal Ocean Upwelling, Science, *247*(4939), 198

Behrenfeld, M. J., and P. G. Falkowski (1997), A consumer's guide to phytoplankton primary productivity, Limnol. Oceanogr., *42*(7), 1479-1491. doi:10.4319/lo.1997.7.1479

Behrenfeld, M. J., Y. Hu, C. A. Hostetler, G. Dall'Olmo, S. D. Rodier, J. W. Hair, and C. R. Trepte (2013), Space-based lidar measurements of global ocean carbon stocks, Geophys. Res. Lett., *40*(16), 4355-4360

Behrenfeld, M. J., et al. (2016), Annual boom–bust cycles of polar phytoplankton biomass revealed by space-based lidar, Nature Geoscience, *10*, 118. doi:10.1038/ngeo2861
https://www.nature.com/articles/ngeo2861#supplementary-information

Bilbro, J. W., C. DiMarzio, D. Fitzjarrald, S. Johnson, and W. Jones (1986), Airborne Doppler lidar measurements, Appl. Optics, *25*(21), 3952-3960. doi:10.1364/AO.25.003952

Birch, D. A., W. Young, and P. Franks (2008), Thin layers of plankton: Formation by shear and death by diffusion, Deep-Sea Research Part 1, *55*, 277-295. doi:10.1016/j.dsr.2007.11.009

Bliokh, K. Y., and Y. A. Kravtso (2004), Observation of sunlight enhanced backscattering from the sea bottom near the beach, Waves in Random Media, *14*(3), 479-483. doi:10.1088/0959-7174/14/3/016

Boss, E., and W. S. Pegau (2001), Relationship of light scattering at an angle in the backward direction to the backscattering coefficient, Appl. Opt., *40*(30), 5503-5507. doi:10.1364/AO.40.005503

Bourgain, P., and J. C. Gascard (2011), The Arctic Ocean halocline and its interannual variability from 1997 to 2008, Deep Sea Res. I, *58*(7), 745-756. doi:https://doi.org/10.1016/j.dsr.2011.05.001

Brown, Z. W., K. E. Lowry, M. A. Palmer, G. L. van Dijken, M. M. Mills, R. S. Pickart, and K. R. Arrigo (2015), Characterizing the subsurface chlorophyll a maximum in the Chukchi Sea and Canada Basin, Deep Sea Res. II. doi:10.1016/j.dsr2.2015.02.010

Chami, M., E. Marken, J. J. Stamnes, G. Khomenko, and G. Korotaev (2006), Variability of the relationship between the particulate backscattering coefficient and the volume scattering function measured at fixed angles, J. Geophys. Res. Oceans, *111*(C5), C05013. doi:10.1029/2005JC003230

Churnside, J., B. McCarty, and X. Lu (2013), Subsurface Ocean Signals from an Orbiting Polarization Lidar, Remote Sensing, *5*(7), 3457-3475

Churnside, J., R. Marchbanks, C. Lembke, and J. Beckler (2017), Optical Backscattering Measured by Airborne Lidar and Underwater Glider, Remote Sensing, *9*(4), 379

Churnside, J. H. (2008), Polarization effects on oceanographic lidar, Opt. Express, *16*(2), 1196-1207. doi:10.1364/oe.16.001196

Churnside, J. H. (2014), Review of profiling oceanographic lidar, Opt. Eng., *53*(5), 051405-051405. doi:10.1117/1.oe.53.5.051405

Churnside, J. H. (2015), Bio-optical model to describe remote sensing signals from a stratified ocean, J. Appl. Remote Sens., *9*(1), 095989-095989. doi:10.1117/1.jrs.9.095989

Churnside, J. H., and J. J. Wilson (2001), Airborne lidar for fisheries applications, Opt. Eng., *40*(3), 406-414

Churnside, J. H., and L. A. Ostrovsky (2005), Lidar observation of a strongly nonlinear internal wave train in the Gulf of Alaska, Int. J. Remote Sens., *26*(1), 167-177. doi:10.1080/01431160410001735076

Churnside, J. H., and R. E. Thorne (2005), Comparison of airborne lidar measurements with 420 kHz echo-sounder measurements of zooplankton, Appl. Opt., *44*(26), 5504-5511

Churnside, J. H., and J. J. Wilson (2006), Power spectrum and fractal dimension of laser backscattering from the ocean, Journal of the Optical Society of America a-Optics Image Science and Vision, *23*(11), 2829-2833

Churnside, J. H., and P. L. Donaghay (2009), Thin scattering layers observed by airborne lidar, ICES J. Mar. Sci., *66*(4), 778-789. doi:10.1093/icesjms/fsp029

Churnside, J. H., and R. Marchbanks (2015), Sub-surface plankton layers in the Arctic Ocean, Geophys. Res. Lett., *42*, 4896-4902. doi:10.1002/2015GL064503

Churnside, J. H., and R. D. Marchbanks (2017), Inversion of oceanographic profiling lidars by a perturbation to a linear regression, Appl. Opt., *56*(18), 5228-5233. doi:10.1364/AO.56.005228

Churnside, J. H., J. M. Sullivan, and M. S. Twardowski (2014), Lidar extinction-to-backscatter ratio of the ocean, Opt. Express, *22*(15), 18698-18706. doi:10.1364/oe.22.018698

Churnside, J. H., R. D. Marchbanks, J. H. Lee, J. A. Shaw, A. Weidemann, and P. L. Donaghay (2012), Airborne lidar detection and characterization of internal waves in a shallow fjord, J. Appl. Remote Sens., *6*(1), 063611: 063611-063615. doi:10.1117/1.jrs.6.063611

Coachman, L. K., and C. A. Barnes (1961), The contribution of Bering Sea water to the Arctic Ocean, Arctic, *14*, 147-161

Comiso, J. C. (2011), Large Decadal Decline of the Arctic Multiyear Ice Cover, J. Clim., *25*(4), 1176-1193. doi:10.1175/jcli-d-11-00113.1

Cota, G., L. Pomeroy, W. Harrison, E. Jones, F. Peters, W. J. Sheldon, and T. Weingartner (1996), Nutrients, primary production and microbial heterotrophy in the southeastern Chukchi Sea: Arctic summer nutrient depletion and heterotrophy, Mar. Ecol. Prog. Ser., *135*, 247-258. doi:10.3354/meps135247

Coupel, P., H. Y. Jin, D. Ruiz-Pino, J. F. Chen, S. H. Lee, H. L. Li, M. Rafizadeh, V. Garçon, and J. C. Gascard (2011), Phytoplankton distribution in the Western Arctic Ocean during a summer of exceptional ice retreat, Biogeosciences Discuss., *8*(4), 6919-6970. doi:10.5194/bgd-8-6919-2011

Cox, C., and W. Munk (1954), Measurement of the Roughness of the Sea Surface from Photographs of the Sun?s Glitter, J. Opt. Soc. Am., *44*(11), 838-850

Crawford, R. E., S. Vagle, and E. C. Carmack (2012), Water mass and bathymetric characteristics of polar cod habitat along the continental shelf and slope of the Beaufort and Chukchi seas, Polar Biol., *35*(2), 179-190. doi:10.1007/s00300-011-1051-9

Cutten, D. R., J. Rothermel, M. A. Jarzembski, R. M. Hardesty, J. N. Howell, D. M. Tratt, and V. Srivastava (2002), Radiometric calibration of an airborne CO2 pulsed Doppler lidar with a natural Earth surface, Appl. Optics, *41*(18), 3530-3537. doi:10.1364/AO.41.003530

Donelan, M. A., and W. J. Pierson, Jr. (1987), Radar Scattering and Equilibrium Ranges in Wind-Generated Waves With Application to Scatterometry, J. Geophys. Res., *92*(C5), 4971-5029. doi:10.1029/JC092iC05p04971

Elfouhaily, T., B. Chapron, K. Katsaros, and D. Vandemark (1997), A unified directional spectrum for long and short wind-driven waves, J. Geophys. Res., *102*(C7), 15781-15796. doi:10.1029/97jc00467

Fetterer, F., M. Savoie, S. Helfrich, and P. Clement-Colon (2010), Multisensor Analyzed Sea Ice Extent - Northern Hemisphere (MASIE-NH), Version 1, edited, p. Daily ice extent, National Ice Center and National Snow and Ice Data Center, Boulder, Colorado, USA.https://doi.org/10.7265/N5GT5K3K

Flagg, C. N., and S. L. Smith (1989), On the use of the acoustic Doppler current profiler to measure zooplankton abundance, Deep Sea Research Part A. Oceanographic Research Papers, *36*(3), 455-474. doi:https://doi.org/10.1016/0198-0149(89)90047-2

Goldin, Y. A., A. N. Vasilev, A. S. Lisovskiy, and V. I. Chernook (2007), Results of Barents Sea airborne lidar survey, paper presented at Current Research on Remote Sensing, Laser Probing, and Imagery in Natural Waters, SPIE.

Gong, D., and R. S. Pickart (2015), Summertime circulation in the eastern Chukchi Sea, Deep Sea Res. II, *118*, 18-31. doi:https://doi.org/10.1016/j.dsr2.2015.02.006

Grebmeier, J. M., S. E. Moore, J. E. Overland, K. E. Frey, and R. Gradinger (2010), Biological Response to Recent Pacific Arctic Sea Ice Retreats, Eos, Transactions American Geophysical Union, *91*(18), 161-162. doi:doi:10.1029/2010EO180001

Grund, C. J., and E. W. Eloranta (1991), University of Wisconsin high spectral resolution lidar, Optical Engineering, *30*(1), 6-13

Hair, J., et al. (2016), Combined Atmospheric and Ocean Profiling from an Airborne High Spectral Resolution Lidar, EPJ Web of Conferences, *119*, 22001

Hair, J. W., C. A. Hostetler, A. L. Cook, D. B. Harper, R. A. Ferrare, T. L. Mack, W. Welch, L. R. Izquierdo, and F. E. Hovis (2008), Airborne High Spectral Resolution Lidar for profiling aerosol optical properties, Appl. Opt., *47*(36), 6734-6752

Hall, F. F., and H. Y. Ageno (1970), Absolute Calibration of a Laser System for Atmospheric Probing, Appl. Optics, *9*(8), 1820-1824. doi:10.1364/AO.9.001820

Hasselmann, D. E., M. Dunckel, and J. A. Ewing (1980), Directional Wave Spectra Observed during JONSWAP 1973, J. Phys. Oceanogr., *10*(8), 1264-1280. doi:10.1175/1520-0485(1980)010<1264:dwsodj>2.0.co;2

Hegseth, E. N. (1998), Primary production of the northern Barents Sea, Polar Res., *17*(2), 113-123. doi:doi:10.1111/j.1751-8369.1998.tb00266.x

Hill, V., and G. Cota (2005), Spatial patterns of primary production on the shelf, slope and basin of the Western Arctic in 2002, Deep Sea Res. II, *52*(24–26), 3344-3354. doi:10.1016/j.dsr2.2005.10.001

Hill, V. J., and R. C. Zimmerman (2010), Estimates of primary production by remote sensing in the Arctic Ocean: Assessment of accuracy with passive and active sensors, Deep Sea Res. I, *57*(10), 1243-1254. doi:10.1016/j.dsr.2010.06.011

Hoge, F. E., C. W. Wright, W. B. Krabill, R. R. Buntzen, G. D. Gilbert, R. N. Swift, J. K. Yungel, and R. E. Berry (1988), Airborne Lidar Detection of Subsurface Oceanic Scattering Layers, Appl. Opt., *27*(19), 3969-3977

Hostetler, C. A., M. J. Behrenfeld, Y. Hu, J. W. Hair, and J. A. Schulien (2018), Spaceborne Lidar in the Study of Marine Systems, Annu. Rev. Mar. Sci., *10*(1), 121-147. doi:10.1146/annurev-marine-121916-063335

Hu, Y., et al. (2008), Sea surface wind speed estimation from space-based lidar measurements, Atmos. Chem. Phys., *8*(13), 3593-3601. doi:10.5194/acp-8-3593-2008

Hunt, W. H., D. M. Winker, M. A. Vaughan, K. A. Powell, P. L. Lucker, and C. Weimer (2009), CALIPSO Lidar Description and Performance Assessment, Journal of Atmospheric and Oceanic Technology, *26*(7), 1214-1228. doi:10.1175/2009jtecha1223.1

Isobe, T., E. D. Feigelson, M. G. Akritas, and G. J. Babu (1990), Linear regression in astronomy. I, The Astrophysical Journal, *364*, 104-113

Itoh, M., S. Nishino, Y. Kawaguchi, and T. Kikuchi (2013), Barrow Canyon volume, heat, and freshwater fluxes revealed by long-term mooring observations between 2000 and 2008, J. Geophys. Res. Oceans, *118*(9), 4363-4379. doi:doi:10.1002/jgrc.20290

Jacox, M. G., C. A. Edwards, M. Kahru, D. L. Rudnick, and R. M. Kudela (2015), The potential for improving remote primary productivity estimates through subsurface chlorophyll and irradiance measurement, Deep Sea Res. II, *112*, 107-116. doi:https://doi.org/10.1016/j.dsr2.2013.12.008

Jakobsson, M., et al. (2012), The International Bathymetric Chart of the Arctic Ocean (IBCAO) Version 3.0, Geophys. Res. Lett., *39*(12). doi:doi:10.1029/2012GL052219

Kalnay, E., et al. (1996), The NCEP/NCAR 40-Year Reanalysis Project, Bulletin of the American Meteorological Society, *77*(3), 437-472. doi:10.1175/1520-0477(1996)077<0437:tnyrp>2.0.co;2
Kavaya, M. J., and R. T. Menzies (1985), Lidar aerosol backscatter measurements: systematic, modeling, and calibration error considerations, Appl. Optics, *24*(21), 3444-3453. doi:10.1364/AO.24.003444
Kokhanenko, G. P., M. M. Krekova, I. E. Penner, and V. S. Shamanaev (2005), Influence of the air–water interface on hydrosol lidar operation, Appl. Optics, *44*(17), 3510-3519. doi:10.1364/AO.44.003510
Kwok, R., and D. A. Rothrock (2009), Decline in Arctic sea ice thickness from submarine and ICESat records: 1958–2008, Geophys. Res. Lett., *36*(15), L15501. doi:10.1029/2009gl039035
Lee, J. H., J. H. Churnside, R. D. Marchbanks, P. L. Donaghay, and J. M. Sullivan (2013), Oceanographic lidar profiles compared with estimates from in situ optical measurements, Appl. Opt., *52*(4), 786-794. doi:10.1364/AO.52.000786
Lee, Y., et al. (2015), An assessment of phytoplankton primary productivity in the Arctic Ocean from satellite ocean color/in situ chlorophyll-a based models, Journal of Geophysical Research-Oceans, *120*(9), 6508-6541. doi:10.1002/2015jc011018
Lu, X., Y. Hu, Z. Liu, S. Zeng, and C. Trepte (2013), CALIOP receiver transient response study, paper presented at SPIE Optical Engineering + Applications, SPIE.
Lu, X., Y. Hu, C. Trepte, S. Zeng, and J. H. Churnside (2014), Ocean subsurface studies with the CALIPSO spaceborne lidar, J. Geophys. Res. Oceans, *119*(7), 4305-4317. doi:10.1002/2014jc009970
Lu, X., Y. Hu, Z. Liu, S. Rodier, M. Vaughan, P. Lucker, C. Trepte, and J. Pelon (2017), Observations of Arctic snow and sea ice cover from CALIOP lidar measurements, Remote Sens. Environ., *194*, 248-263. doi:https://doi.org/10.1016/j.rse.2017.03.046
Lu, X., et al. (2016), Retrieval of ocean subsurface particulate backscattering coefficient from space-borne CALIOP lidar measurements, Opt. Express, *24*(25), 29001-29008. doi:10.1364/OE.24.029001
Martin, J., D. Dumont, and J.-É. Tremblay (2013), Contribution of subsurface chlorophyll maxima to primary production in the coastal Beaufort Sea (Canadian Arctic): A model assessment, J. Geophys. Res. Oceans, *118*(11), 5873-5886. doi:doi:10.1002/2013JC008843
Martin, J., J. Tremblay, J. Gagnon, G. Tremblay, A. Lapoussi, C. Jose, M. Poulin, M. Gosselin, Y. Gratton, and C. Michel (2010), Prevalence, structure and properties of subsurface chlorophyll maxima in Canadian Arctic waters, Mar. Ecol. Prog. Ser., *412*, 69-84. doi:10.3354/meps08666
McLean, J. W., and J. D. Freeman (1996), Effects of ocean waves on airborne lidar imaging, Appl. Optics, *35*(18), 3261-3269. doi:10.1364/AO.35.003261
Metropolis, N., and S. Ulam (1949), The Monte Carlo Method, Journal of the American Statistical Association, *44*(247), 335-341. doi:10.1080/01621459.1949.10483310
Mobley, C. D. (1994), *Light and Water: Radiative transfer in natural waters*, 592 pp., Academic Press, San Diego.
Moore, S. E., and J. M. Grebmeier (2018), The Distributed Biological Observatory: Linking Physics to Biology in the Pacific Arctic Region, Arctic, *71*(5), 1-7. doi:10.14460/arctic4606
Moses, W. J., S. G. Ackleson, J. W. Hair, C. A. Hostetler, and W. D. Miller (2016), Spatial scales of optical variability in the coastal ocean: Implications for remote sensing and in situ

sampling, Journal of Geophysical Research: Oceans, *121*(6), 4194-4208. doi:10.1002/2016JC011767

Mountain, D. G., L. K. Coachman, and K. Aagaard (1976), On the Flow Through Barrow Canyon, J. Phys. Oceanogr., *6*(4), 461-470. doi:10.1175/1520-0485(1976)006<0461:otftbc>2.0.co;2

Naoya, K., S. Shin, O. Yoshihiko, S. Daiki, F. Yasushi, and N. Daiki (2018), Upwelling of Macronutrients and Dissolved Inorganic Carbon by a Subglacial Freshwater Driven Plume in Bowdoin Fjord, Northwestern Greenland, Journal of Geophysical Research: Biogeosciences, *123*(5), 1666-1682. doi:doi:10.1029/2017JG004248

Osse, T. J., C. Meinig, S. Stalin, and H. Milburn (2015), The PRAWLER, a vertical profiler powered by wave energy, paper presented at OCEANS 2015 - MTS/IEEE Washington, 19-22 Oct. 2015.

Petzold, T. J. (1972), Volume scattering functions for selected ocean waters*Rep.*, Scripps Institution of Oceanography, La Jolla, CA.

Pierson, W. J., Jr., and L. Moskowitz (1964), A Proposed Spectral Form for Fully Developed Wind Seas Based on the Similarity Theory of S. A. Kitaigorodskii, J. Geophys. Res., *69*(24), 5181-5190. doi:10.1029/JZ069i024p05181

Pithan, F., and T. Mauritsen (2014), Arctic amplification dominated by temperature feedbacks in contemporary climate models, Nature Geosci, *7*(3), 181-184. doi:10.1038/ngeo2071

Ressler, P. H. (2002), Acoustic backscatter measurements with a 153kHz ADCP in the northeastern Gulf of Mexico: determination of dominant zooplankton and micronekton scatterers, Deep Sea Res. I, *49*(11), 2035-2051. doi:https://doi.org/10.1016/S0967-0637(02)00117-6

Retamal, L., S. Bonilla, and W. F. Vincent (2008), Optical gradients and phytoplankton production in the Mackenzie River and the coastal Beaufort Sea, Polar Biol., *31*(3), 363-379. doi:10.1007/s00300-007-0365-0

Ríos, F., R. Kilian, and E. Mutschke (2016), Chlorophyll-a thin layers in the Magellan fjord system: The role of the water column stratification, Cont. Shelf Res., *124*, 1-12. doi:https://doi.org/10.1016/j.csr.2016.04.011

Schulien, J. A., M. J. Behrenfeld, J. W. Hair, C. A. Hostetler, and M. S. Twardowski (2017), Vertically- resolved phytoplankton carbon and net primary production from a high spectral resolution lidar, Opt. Express, *25*(12), 13577-13587. doi:10.1364/OE.25.013577

Serreze, M. C., and R. G. Barry (2011), Processes and impacts of Arctic amplification: A research synthesis, Global Planet. Change, *77*(1–2), 85-96. doi:org/10.1016/j.gloplacha.2011.03.004

Shaw, J. A., and J. H. Churnside (1997), Scanning-laser glint measurements of sea-surface slope statistics, Appl. Opt., *36*(18), 4202-4213

Shifrin, K. S. (1988), *Physical Optics of Ocean Water*, 285 pp., American Institute of Physics, New York.

Shipley, S. T., D. H. Tracy, E. W. Eloranta, J. T. Trauger, J. T. Sroga, F. L. Roesler, and J. A. Weinman (1983), High spectral resolution lidar to measure optical scattering properties of atmospheric aerosols. 1: Theory and instrumentation, Appl. Optics, *22*(23), 3716-3724. doi:10.1364/AO.22.003716

Shroyer, E. L., K. J. Benoit-Bird, J. D. Nash, and J. N. Moum (2014), Stratification and mixing regimes in biological thin layers over the Mid-Atlantic Bight, Limnol. Oceanogr., *59*(4), 1349-1363. doi:10.4319/lo.2014.59.4.1349

Spreen, G., R. Kwok, and D. Menemenlis (2011), Trends in Arctic sea ice drift and role of wind forcing: 1992–2009, Geophys. Res. Lett., *38*(19), L19501. doi:10.1029/2011gl048970

Sreenivasan, K. R. (1996), *The Passive Scalar Spectrum and the Obukhov-Corrsin Constant*, 189-196 pp.

Stabeno, P., N. Kachel, C. Ladd, and R. Woodgate (2018), Flow Patterns in the Eastern Chukchi Sea: 2010–2015, J. Geophys. Res. Oceans, *123*(2), 1177-1195. doi:doi:10.1002/2017JC013135

Sullivan, J. M., and M. S. Twardowski (2009), Angular shape of the oceanic particulate volume scattering function in the backward direction, Appl. Opt., *48*(35), 6811-6819. doi:10.1364/ao.48.006811

Tabisola, H. M., P. J. Stabeno, and C. W. Mordy (2017), Using a biophysical mooring as a sentinel for ecosystem change: The story of M2, paper presented at OCEANS 2017 - Anchorage, 18-21 Sept. 2017.

Taylor, P. C., M. Cai, A. Hu, J. Meehl, W. Washington, and G. J. Zhang (2013), A Decomposition of Feedback Contributions to Polar Warming Amplification, J. Clim., *26*(18), 7023-7043. doi:10.1175/jcli-d-12-00696.1

Vasilkov, A. P., Y. A. Goldin, B. A. Gureev, F. E. Hoge, R. N. Swift, and C. W. Wright (2001), Airborne polarized lidar detection of scattering layers in the ocean, Appl. Opt., *40*(24), 4353-4364

Vaughan, D. G., et al. (2013), Observations: Cryosphere, in *Climate Change 2013: The Physical Science Basis. Contribution of Working Group I to the Fifth Assessment Report of the Intergovernmental Panel on Climate Change*, edited by T. F. Stocker, D. Qin, G.-K. Plattner, M. Tignor, S. K. Allen, J. Boschung, A. Nauels, Y. Xia, V. Bex and P. M. Midgley, pp. 317-382, Cambridge University Press, Cambridge

Weingartner, T. J., D. J. Cavalieri, K. Aagaard, and Y. Sasaki (1998), Circulation, dense water formation, and outflow on the northeast Chukchi Shelf, J. Geophys. Res. Oceans, *103*(C4), 7647-7661. doi:doi:10.1029/98JC00374

Westberry, T., M. J. Behrenfeld, D. A. Siegel, and E. Boss (2008), Carbon-based primary productivity modeling with vertically resolved photoacclimation, Global Biogeochem. Cycles, *22*(2), GB2024. doi:10.1029/2007gb003078

Weston, K., L. Fernand, D. K. Mills, R. Delahunty, and J. Brown (2005), Primary production in the deep chlorophyll maximum of the central North Sea, J. Plankton Res., *27*(9), 909-922. doi:10.1093/plankt/fbi064

Weston, K., L. Fernand, D. K. Mills, R. Delahunty, and J. Brown (2011), Primary production in the deep chlorophyll maximum of the central North Sea, J. Plankton Res., *33*(10), 1627-1628. doi:10.1093/plankt/fbr067

Zhou, Y., D. Liu, P. Xu, C. Liu, J. Bai, L. Yang, Z. Cheng, P. Tang, Y. Zhang, and L. Su (2017), Retrieving the seawater volume scattering function at the 180° scattering angle with a high-spectral-resolution lidar, Optics Express, *25*(10), 11813-11826. doi:10.1364/OE.25.011813

Final Annual Progress Report
NNX16AR48G

MODELING STUDIES FOR EXPORTS IN A DYNAMIC OCEAN ENVIRONMENT

November 23, 2019

Personnel

Amala Mahadevan (PI, WHOI)
Tel: (508) 289 3440; E-mail: amala@whoi.edu
David Nicholson (co-I, WHOI)
Andrew Thompson (co-I, Caltech)
Melissa Omand (co-I, University of Rhode Island)
Adrian Martin (Collaborator, NERC, UK)
Mathieu Dever (Postdoctoral Investigator, WHOI)
Zachary Erickson (Ph.D. 2019, Caltech)
Alexis Johnson (M.S. candidate, University of Rhode Island)

Reporting Period: July, 2018 – August, 2019

Objectives

Our objectives are to (1) Analyze existing data sets from previous observational campaigns to characterize the flow field and export of particulate organic matter (POM) in regions where the EXPORTS campaign will be conducted; (2) Characterize the vertical transport of POM as a function of the flow field; and (3) Assess the ability of various observing platforms to characterize these fluxes. Our results will improve our ability to interpret observational data and to suggest strategies for employing a system observing assets for the EXPORTS field campaigns.

1 DATA MINING

1.1 North Atlantic – BGC-Argo floats

University of Rhode Island M.S. student Alexis Johnson analyzed seven biogeochemical (BGC) Argo floats (Fig. 1a) in the subpolar North Atlantic, looking for evidence of physical particulate organic carbon subduction. The criteria used to identify features of subduction following those described in Omand et al. [2015]. Namely, subsurface maxima in bbp, chl F, and AOU, coinciding with spice features, and appearing below the euphotic zone and mixed layer. Of the 1,956 profiles searched, 269 met the criteria for a subduction feature. The occurrence of these features was highest in summer (Fig. 1b,c)

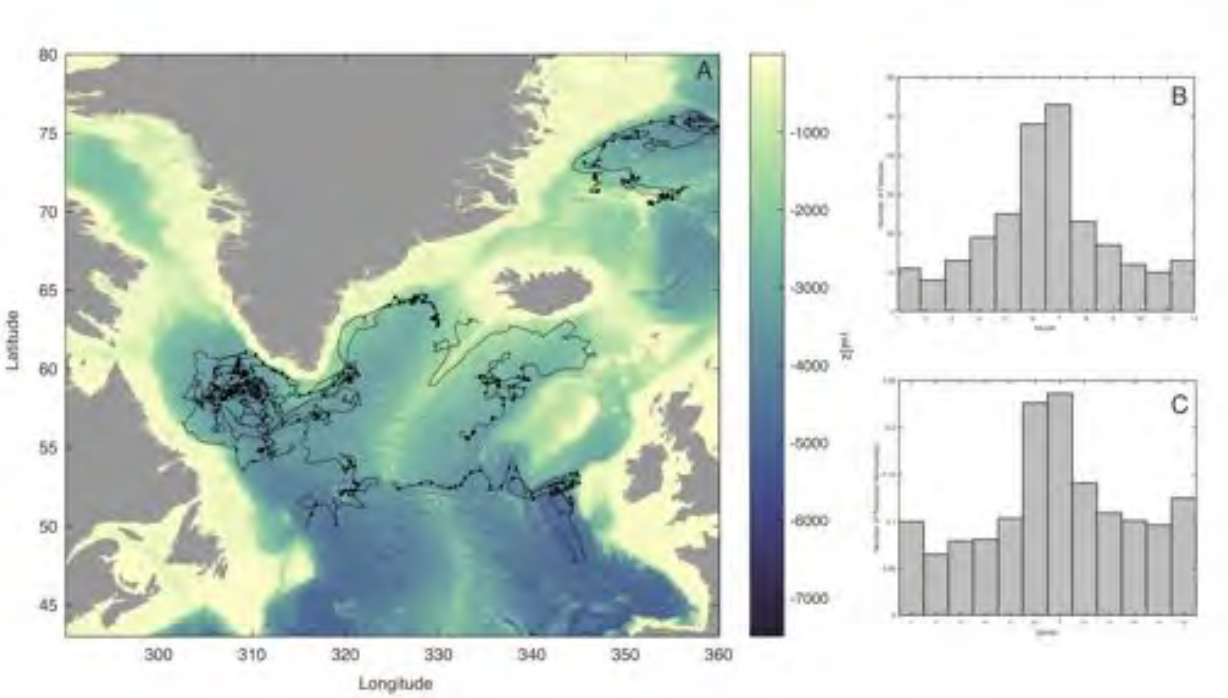

Figure 1: a) Map indicating the trajectories of the 7 BGC Argo floats analyzed by Alexis Johnson. b) The number of features observed in each month, indicating a nearly 3-fold increase during summer versus winter. c) The normalized distribution (accounting for the total number of profiles occurring in each month). This plot shows that the summertime increase is preserved, and suggests that there is a greater probability of observing a subduction feature during the summer.

Particular attention was placed on the BGC Argo float that spent time in the region of the proposed NA EXPORTS study site near 342E (18W), 52N (see Fig. 1a). In July and September 2015, when the float was in the NA EXPORTS region, it sampled a series of elevated POC features (derived from particle backscatter, bbp) around 300m depth (Fig. 2). A focused analysis from this record combined with HYCOM data indicated that the ele-

vated features were likely subducted from the surface in a region about 50-100km to the south of the float's location, during spring of that year. The fact that this feature was still very distinctive 3 months after subduction is remarkable, and speaks to the persistence of such features and their remaining detectable for months after they were formed. This may also help explain why we saw most subducted features in summer (Fig. 1b,c), even though the vertical velocities associated with submesoscale subduction is most intense during the winter [Erickson and Thompson, 2018]. Our hypothesis is that the subduction is occurring in winter or spring, and the features become apparent once they are capped-off by a warm stratified layer at the surface during the summer, thus meeting our criteria of being below the MLD.

This work is part of Ali Johnson's M.S. thesis titled "Evolution of a subducted carbon-rich filament on the edge of the North Atlantic gyre" that she will defend in February 2020.

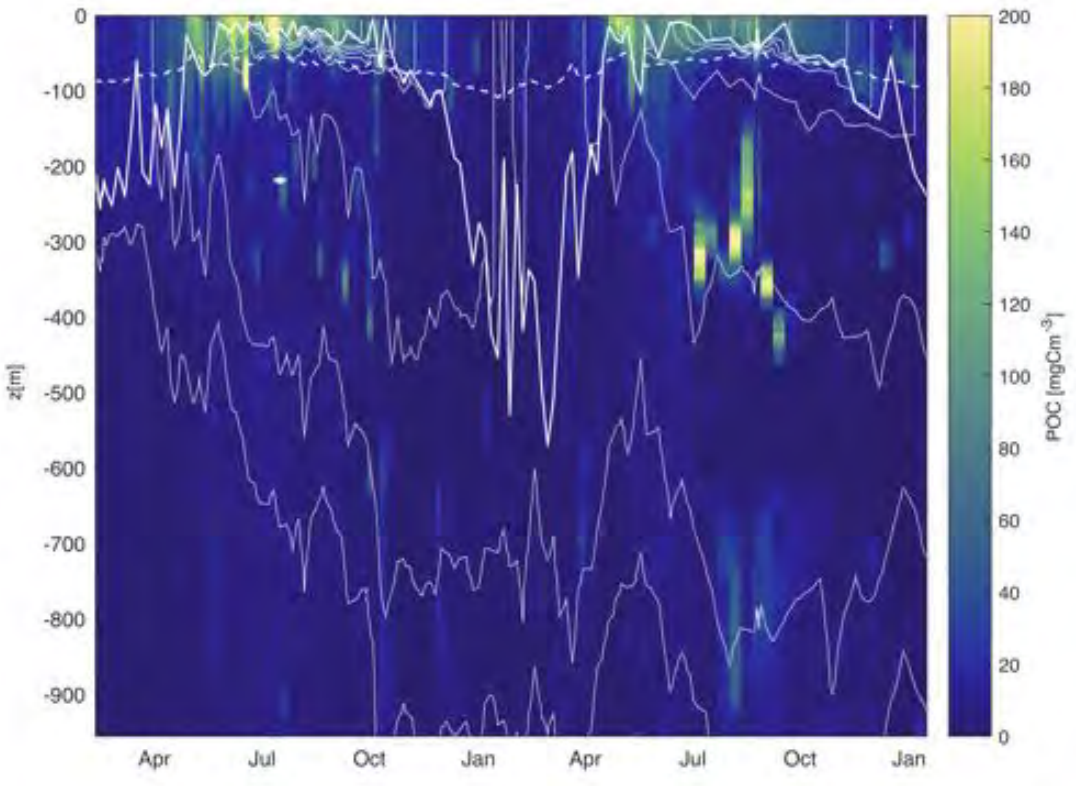

Figure 2: Timeseries of POC (derived from bbp) from MBARI float 0276NoAtlantic. The heavy white line indicates the mixed layer depth, and the thin white lines indicate isopycnals. The dashed white line shows the euphotic depth.

1.2 North Atlantic – Planning for 2020 EXPORTS North Atlantic field experiment

The spring 2020 EXPORTS field study will be sited at or near the Porcupine Abyssal Plain site (50°N, 16 °W). This project has supported participation of the project group in the planning process. One aspect of planning is to understand the transport and dispersion of drifting autonomous assets deployed as part of the study. co-PI Nicholson will be responsible for deploying BGC-Argo floats. To predict potential dispersal of project floats, the core Argo dataset was mined to track previous trajetories of the more abundant core Argo floats that have passed through the study region. Core Argo floats drift at the same 1000 db level as the BGC floats and thus should have similar behaviour. This activity contributes to a larger effort of Observing System Simulation Experiments and planning that has been underway to coordinated ship-based an autonomous assets that will be deployed in 2020. A plan is under development to center the process study on a selected retentive eddy in the region. Project members Nicholson, Omand, Thompson and Erickson have contributed to the collaborative planning effort.

1.3 North Atlantic – Mooring and glider analysis of the OSMOSIS observations

Caltech graduate student, Zachary Erickson, produced as part of his Ph.D. thesis [Erickson, 2019] an analysis of the seasonality of upper ocean turbulence and tracer fluxes from a year-long time series of submesoscale-resolving observations in the northeast Atlantic. These measurements were collected between September 2011 and September 2012 as part of the OSMOSIS (Ocean Surface Mixing Ocean Submesoscale Interaction Study) project, involving nine instrumented moorings and two ocean gliders. Both platforms enabled calculations of lateral gradients of various properties; all platforms sampled for the entire year (Figure 4).

Turbulent characteristics of ocean flows are often assessed from spectral properties of, for example, kinetic and potential energy and tracer variance. Spectra can be readily calculated from satellite tracks or ship transects, but are more difficult to calculate from less-structured observations. In Erickson et al. [2019], we used the OSMOSIS measurements, both the glider and mooring data, as well as a $1/48^\circ$ numerical ocean model, to probe the seasonality and vertical distribution of submesoscale motions using second-order structure functions, or variance in properties separated by distance. We considered statistical relationships between spice, buoyancy, and horizontal velocities, which provide similar information to spectral decomposition but are better suited to data from arrays of moorings and gliders (Figure 4). This unique observational dataset is the first to enable a statistical description of turbulence properties down to depths of 1 km and horizontal scales of 1 km over a full seasonal cycle. Thus we were able to probe scales that would be

Figure 3: Lines show the trajectory of core Argo floats for a six-month period after a float has entered a box centered on the Porcupine Abyssal Plain site.

expected to be only marginally resolved even in relatively high-resolution global models, for example the $1/48^\circ$ llc4320 analyzed in this study.

An important finding of this study was the emergence of sharp features in spice at scales of less than 5 km, well below the mixed layer. These small-scale features are present in a region of the ocean without strong currents or important bathymetric features, signifying that the results here may also occur in other open ocean areas. We found a clear difference between *in situ* data and model results at small scales, where the *in situ* data had more variance than the model. This is expected, as the effective model resolution is approximately a factor of four larger than the grid scale resolution. However, the model

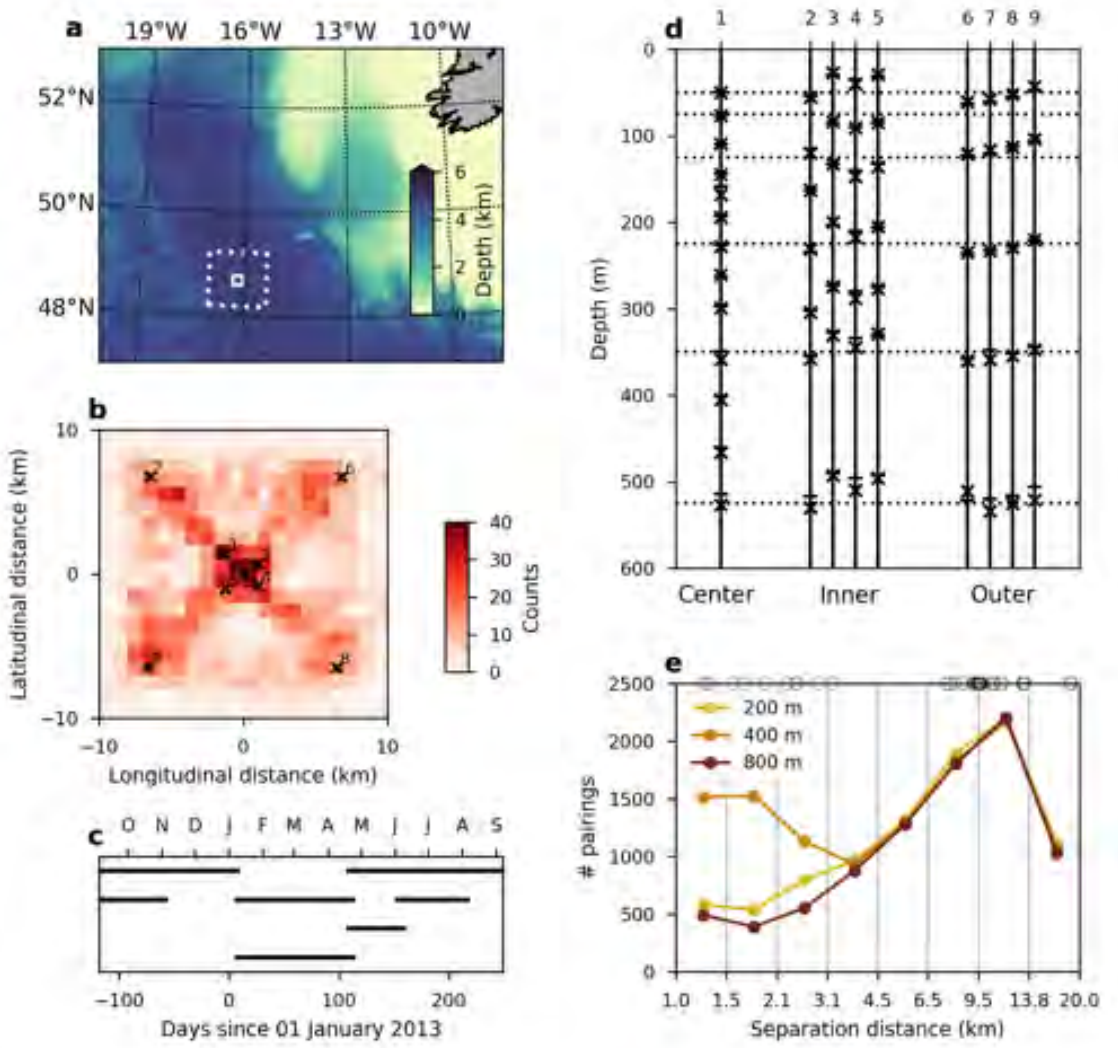

Figure 4: (a) Bathymetry from ETOPO in the northeast Atlantic. OSMOSIS region is shown in the white box at 16.2°W, 48.7°N. Larger region from the model is shown as the dotted white box. (b) Highlight on the OSMOSIS region, showing a histogram of glider surface locations (colors) and the positions of the nine moorings (x's). (c) Periods of time in which the gliders were active. (d) Depth placement of the ACMs (x's) and CTDs (-'s) for each mooring. Dotted horizontal lines denote the depths over which mooring structure functions were calculated. (e) Histogram of structure function pairings from glider measurements at 200, 400, and 800 m depth. Bins are equally spaced logarithmically. Circle markings at the top axis show the separations between moorings.

did compare well with the mooring data using only the sub-inertial components of velocity, buoyancy, and spice variables, even down to very small separations (2 km). This points to high-frequency motions as being the key unresolved physics in the model simulation.

The other important aspect of this study was to highlight the seasonal cycle (Figure 7).

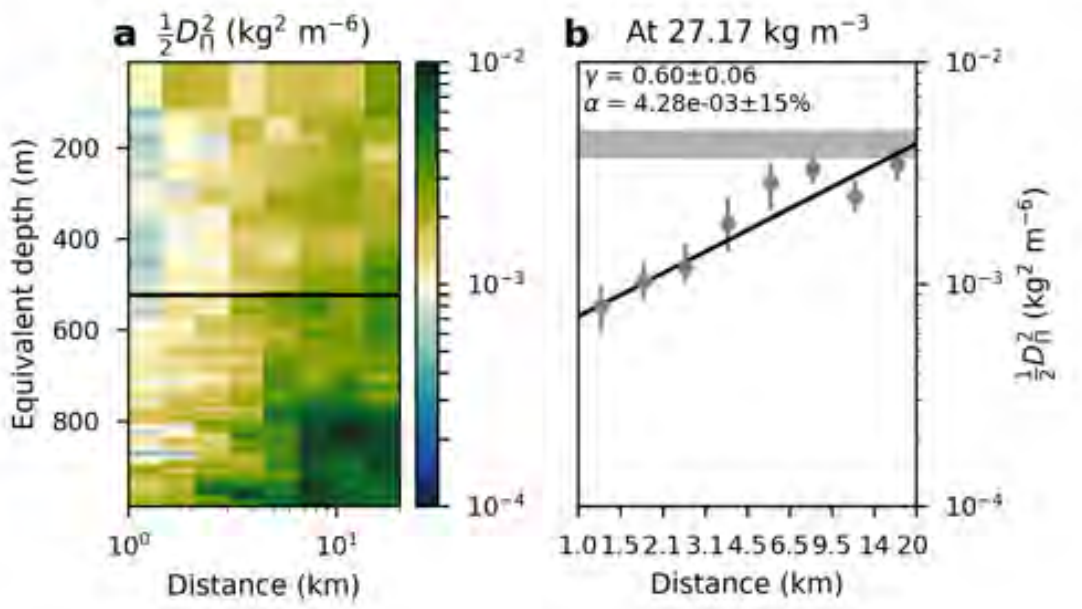

Figure 5: (a) Structure function of spice power at all isopycnals from the glider using winter time data, expressed in terms of equivalent depth (average depth of isopycnal during winter). (b) Example of calculating best-fit slopes for a representative SF taken from 27.17 kg m^3 (525 m equivalent depth) on panel (a). Black line gives the best fit to the data, and grey horizontal bar shows the range of values of the magnitude , defined as the variance at 20 km separation.

In the winter, mixed layers are deeper, yet the model mixed layers are deeper than the in situ data, which we conclude is due to unresolved restratification processes. However, the model structure functions agree much more closely with the *in situ* results during winter than in summer. One reason for this is that the model is more accurately resolving the important physical instabilities in the winter than the summer, because surface-enhanced submesoscale motions are larger in size when the mixed layer is deeper. This lack of sufficient resolution is most apparent during spring, when restratification processes make use of available potential energy to quickly shoal the mixed layer, removing submesoscale energy in the process. In the model high variance in velocities remain throughout spring and into summer, meaning the model does not efficiently transfer this energy to dissipative scales.

We also put this study in the context of other publications, which have found a k^{-2} spectral slope of passive tracers in the ocean regardless of depth. Here we do not reproduce this steep slope, and present this dataset as a counter example to several other studies suggesting a universal k^{-2} passive tracer spectral slope at depth.

These results have interesting implications for the vertical transport of properties beneath the mixed layer. This is especially important for biological properties such as par-

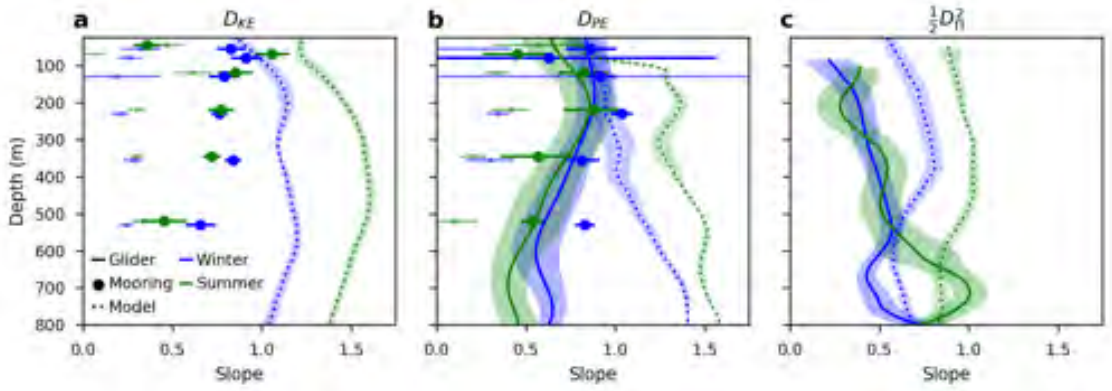

Figure 6: Best-fit slopes of KE (a), PE (b), and spice (c) structure functions from gliders (solid), moorings (dots), and model (dotted line) during winter (blue) and summer (green). Light dots indicate super-inertial structure functions from the moorings. Shading and error bars show the standard deviation of the fits.

ticulate or dissolved carbon, where vertical exchange across the mixed layer base may lead to sequestration and carbon export on long time scales. Our observations suggest that the boundary between the ocean-atmosphere interface and the ocean interior — the pycnocline at the base of the mixed layer — is not well-developed during the wintertime, meaning the conventional distinction between well-mixed surface waters and an ocean interior out of contact with the atmosphere, may not apply during all seasons. In conclusion, these results suggest that submsesoscale motions can be important over much greater depths than the diagnosed mixed layer, especially in the weakly stratified subpolar mode waters.

In Erickson and Thompson [2018], we considered an annual cycle of submesoscale dynamics and their relation to productivity and export in the OSMOSIS study region. In this area, a springtime bloom is initiated by re-stratification of the mixed layer in June 2012, although intermittent shoaling of the mixed layer maintains phytoplankton populations throughout the year. An optical community index suggests a dominance of large species (e.g., diatoms) during spring and pico-phytoplankton during the winter. We reviewed three types of submesoscale instabilities – mixed layer (baroclinic), gravitational, and symmetric – and considered the impact of each on export of fixed carbon out of the surface layer. Mixed layer instabilities can potentially export material out of the mixed layer during winter, although the vertical velocity across the base of the mixed layer is sensitive to the parameterization scheme. Symmetric instabilities, in contrast, provide a clear mechanism for rapid export out of the mixed layer. A crucial factor determining export potential is the strength of the pycnocline at the base of the mixed layer. Export production is sensitive to the degree of overlap that exists between intense submesoscale

activity associated with deep mixed layers in the winter and high productivity associated with the spring restratification, meaning physically-driven export of fixed carbon will likely happen over a short time window during spring.

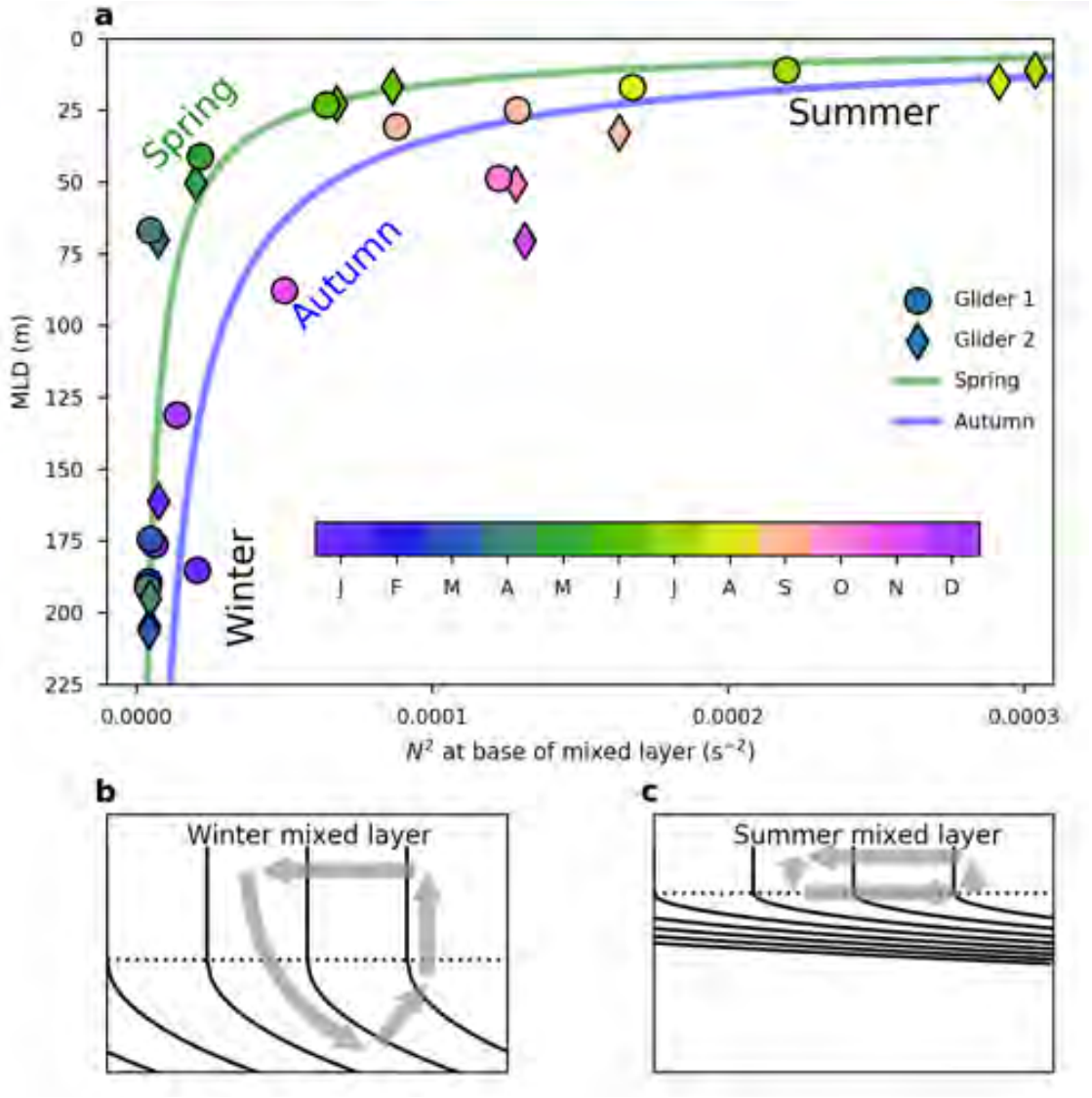

Figure 7: (a) MLD and vertical stratification at the base of the mixed layer as monthly averages for Glider 1 (circles) and Glider 2 (diamonds). The best fit exponential for the winter-to-summer (summer-to-winter) transition is shown in green (blue). (b, c) Schematics for winter (b) and summer (c) surface ocean densities, where solid lines are isopycnal surfaces, dotted lines are the mixed layer depths, and gray arrows show the effect of MLI. MLD = mixed layer depth; MLI = mixed layer instability.

An key result of this study is the coupled seasonal cycle of mixed layer depth and the stratification at the base of the mixed layer, and in particular the difference in these prop-

erties across the fall-winter and winter-spring transitions (Figure 7). During winter, mixed layers are deep and vertical stratification at the base is small. This is shown schematically in Figure 7b, where the along- isopycnal movement of water due to MLI is indicated by the grey arrows. The combination of deep mixed layers, implying a large reservoir of available potential energy, and weak stratification, causing a weak vertical decay of vertical velocities, can lead to deep subduction of water masses through MLI. During the spring, the mixed layer shoals, but periodic de-stratification events keep the vertical stratification at the base of the mixed layer weak, and along-isopycnal motions can still lead to deep subduction. During summer, a strong pycnocline forms, and the mixed layer is shallow with a well-defined base (Figure 7c). This instability is well-parameterized but has negligible export potential. During autumn, the pycnocline is stronger than during spring (Figure 7a), limiting the potential for export during this season, even though the mixed layer is deepening and submesoscale motions in the mixed layer will be more energetic. Thus, the vertical velocities at the base of the mixed layer, and particularly their decay into the interior of the ocean, need to be parameterized accurately based on the observed or simulated stratification to properly account for export by submesoscale motions.

Although we found instances of subduction of water masses, we did not find evidence for substantial export of fixed carbon via this subductive route. Export through submesoscale instabilities requires both the production of unstable water columns and high fixed carbon concentrations at the surface. From this analysis, the influence from submesoscale motions on export is small at this location. This is due to limited overlap between strong, submesoscale vertical velocities across the base of the mixed layer, which are largest during winter, and fixed carbon concentrations in the surface of the ocean, which are largest in spring and summer. We point to the need for future work targeting this overlap window in other regions of the ocean.

This work is part of Erickson's Ph.D. thesis entitled "Physical processes leading to export of fixed carbon out of the surface ocean" that was successfully defended in May of 2019. Zach is now a NASA Postdoctoral Fellow at Goddard Space Flight Center where he is working on both the PACE mission and the EXPORTS project.

1.4 North Pacific – Mooring and glider analysis of observations at Station PAPA

Several datasets collected at Station Papa were used to both initialized and validate the modeling effort. Time series of surface winds and heat fluxes were obtained from the Pacific Marine Environmental Laboratory (PMEL; https://www.pmel.noaa.gov). A year-long time series was generated from data collected over the period 2002-2012 to force the numerical model described in Section 2. The north-south gradient in heat fluxes was determined from a re-analysis product (North American Regional Reanalysis; NARR). Ini-

tial conditions for the model experiments were generated from an ARGO gridded product for the model domain [Gaillard, 2015, Gaillard et al., 2016]. The temperature and salinity fields from ARGO floats are relatively smooth. To introduce frontal features in the model simulations not resolved by the ARGO product, synthetic fronts were generated by locally enhancing the density gradient. The strength of the density fronts was determined from a glider dataset collected at Station Papa between 2008 and 2010 [Pelland et al., 2016, Pelland, 2018]. More precisely, the 95th percentile of the distribution of lateral density gradients observed by the gliders was used to initialize the model runs. Finally, the glider dataset was also used to validate the model, ensuring that the distribution of vertical and lateral density gradients generated in the model simulations resembled observations.

2 MODELING

We have explored the size-dependent export of particles with the Process Study Ocean Model (PSOM) in the region around Station PAPA in the Pacific, which exhibits a mesoscale dynamical character. We have examined two contrasting regimes: (1) **Summer** – when the upper ocean is stratified, mixed layer depths are shallow, and horizontal density gradients in the mixed layer are weak. The flow is dominated by mesoscale eddies, and submesoscale activity is weak or absent. (2) **Winter** – when lateral density gradients are strong and mixed layers deeper. In winter, the flow field is more dynamic, and submesoscale in character, with stronger vertical velocities which can influence the descent rate of particles.

Particles with different settling speeds are released in two process-oriented model simulations of an upper ocean eddying flow to evaluate the impact of (1) ocean dynamics on the respective contribution of the different sinking-velocity classes to POC export, and (2) the particle number size-spectrum slope. The analysis reveals that the leading export mechanism changes from gravitationally-driven to advectively-driven as submesoscale dynamics become more important.

In the model experiments, we used particles (with sinking speeds of 0.0025 m/day – 5 m/day) that could be affected by the vertical velocity of the flow, while recognizing that particles with much higher sinking velocities will not be affected by the flow. A significant fraction of the POC biomass, however, has small sinking velocities in this range.

2.1 Tasks Completed

- Model was set up and run with conditions resembling summer and winter conditions near station PAPA.

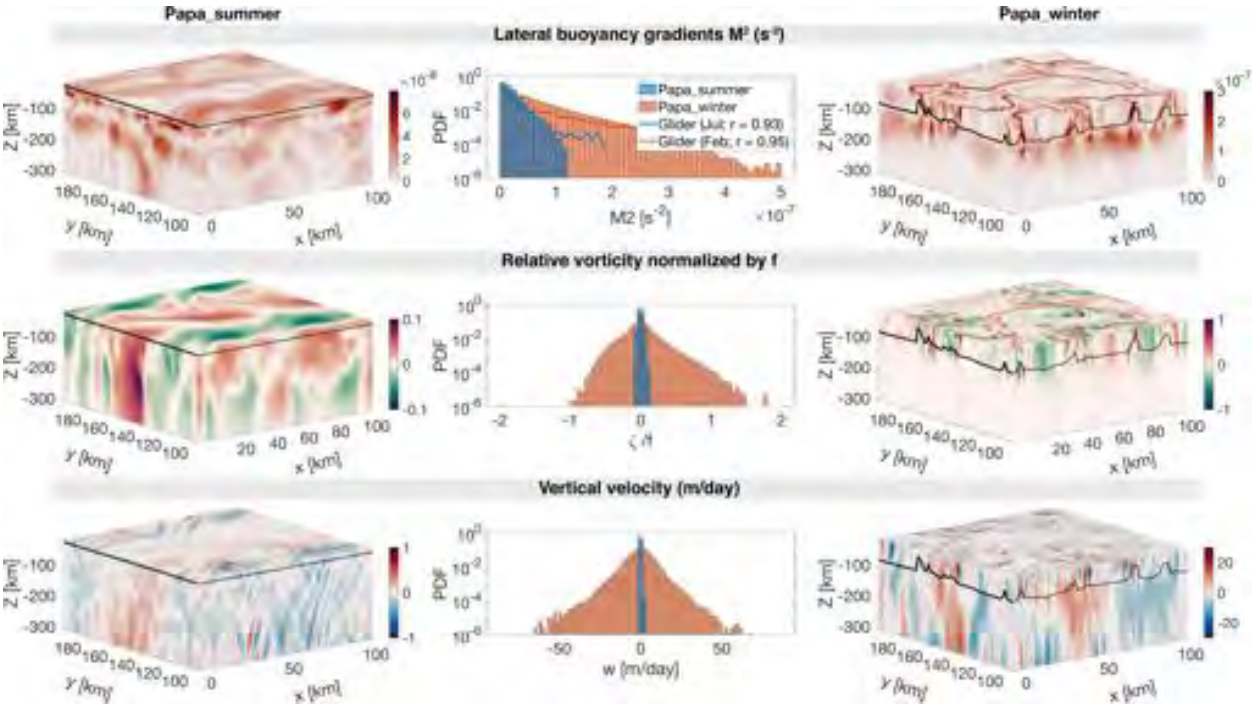

Figure 8: Snapshots of M^2 (top), ζ/f (middle), and w (bottom) half-way through the particle tracking experiment for *Papa_summer* (left) and *Papa_winter* (right), with the Mixed Layer Depth indicated by the solid black line. The corresponding Probability Distribution Functions (PDFs) are shown in the center for both *Papa_summer* (blue) and *Papa_winter* (red). Note the different colorbars used for *Papa_summer* and *Papa_winter*. Histograms of M^2 computed from glider data at Station Papa in February (blue line) and July (red line) are superimposed in the top middle panel.

- Statistics of horizontal and vertical density gradients from the model were compared with glider data collected around Station Papa.
- The summer and winter models were seeded with particles at 85 m depth, to resemble the flux of POC from the base of the euphotic zone.
- Particles were advected with the model flow field. A Lagrangian offline advection module was written for PSOM. The offline advection enables calculating trajectories for large numbers of particles (e.g., 10 million in the case of our experiment).
- The trajectories of particles with different sinking velocities were analyzed.
- Remineralization was implemented on the particles, and the downward biomass flux was calculated in each sinking velocity class.

- Statistics were computed for different size spectral slopes, with and without remineralization.

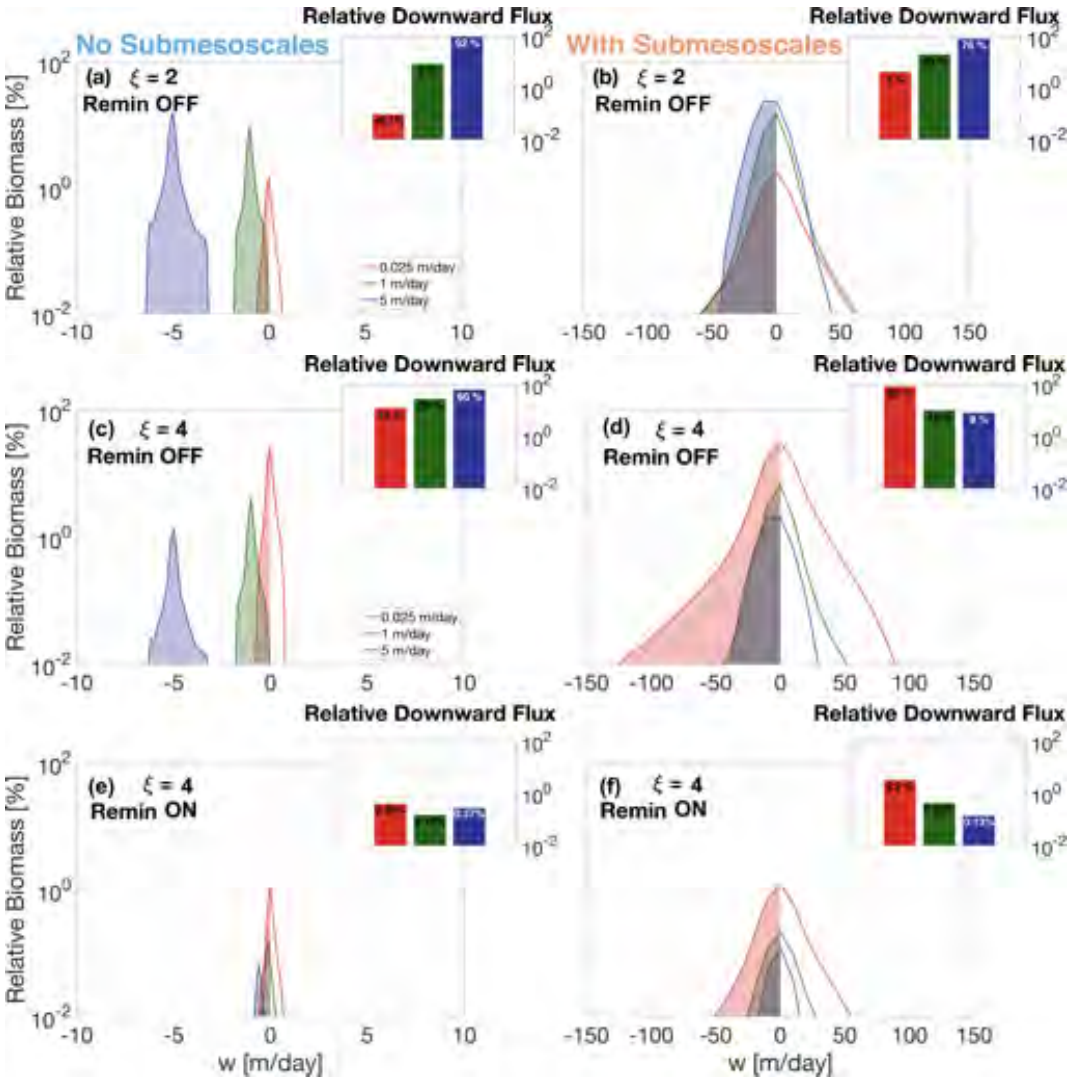

Figure 9: Probability Distribution Function (PDF) of relative biomass versus vertical velocity along particle trajectories in the summer case [left] and winter case [right], with a Junge slope of 2 [top] and 4 [middle and bottom], with [top and middle] and without [bottom] remineralization. Inserts show the integrated relative downward biomass flux associated with each sinking-velocity class. Both winter dynamics and steeper Junge slopes tend to increase the relative contribution of slower-sinking particles, which remains true in the presence of remineralization.

2.2 *Results*

The main conclusions of this study are:

1. Ocean dynamics in the subpolar Northeast Pacific exhibit a seasonal cycle with low submesoscale activity in the summertime, and more submesoscale features present in the wintertime. Submesoscale dynamics generate larger, and asymmetric, vertical currents leading to a vertical biomass flux driven by advective processes, as opposed to gravitational sinking in the summertime.

2. Submesoscale dynamics generally enhance the downward particulate flux by increasing the contribution of slower-sinking particles to the total flux through advective transport. The slower-sinking particles are found to be significant for export, and can be even make the dominant contribution under certain conditions.

3. The contribution of slower-sinking particles to the downward biomass flux depends on the slope of the particle size spectra (i.e., the Junge Slope), that controls the relative number of particles per size class. Two cases emerge from this study:

   (a) If the Junge slope is smaller than 3, larger particles contribute most to vertical biomass fluxes independently of flow dynamics, as there are no mechanisms capable of selectively advecting slower-sinking particles. The system is described as gravitationally-driven.

   (b) If the Junge slope is greater than 3, as most commonly observed, ocean dynamics become key for determining which particle classes dominate the downward flux. As submesoscale dynamics become more active, ageostrophic circulations leading to larger vertical velocities develop. In these conditions, downward biomass fluxes are largely driven by the slower-sinking particle classes.

4. Remineralization processes logically reduce the amount of biomass flux. However, it unexpectedly enhances the role of slower-sinking particles, which are are advectively transported. The impact of remineralization is greater on faster-sinking particles since it affects both the biomass content and their sinking velocity.

3 Presentations

These were presentations made by Mahtieu Dever and Alexis Johnson. The PIs included results from this study in several of their presentations that are not listed here.

- "Physical Subduction and Sequestration of Particulate Organic Carbon in the North Atlantic". Alexis Johnson, Melissa Omand. Ocean Optics Meeting. Dubrovnik Croatia, Nov 2018.

- ”Size-differentiated export in different dynamical regimes of the ocean”. Mathieu Dever, Roo Nicholson, and Amala Mahadevan.
  Seminar at Massachusetts Institute of Technology, Cambridge, U.S.A, Nov 2019
  Seminar at Bedford Institute of Oceanography, Dartmouth, Canada, Oct 2019
  Seminar at Dalhousie University, Halifax, Canada, Sep 2019

- ”Vertical mixing of organic material at meso- and submeso-scales.” Mathieu Dever, Roo Nicholson, Melissa Omand, and Amala Mahadevan. Gordon Research conference on Mixing, Andover, U.S.A., June 2018

4 Recent Manuscripts/Publications

- Erickson, Zachary, 2019, *Ph.D Thesis* (see below)

- Erickson et al., 2019, *J. Phys. Oceanogr.* In Press (see below).

- Dever, Matieu, The Living, Breathing Ocean – Can 'ocean elevators' carry excess carbon to the deep?, 2018, *Oceanus Magazine*, Vol. 53 (2), *Woods Hole Oceanographic Institution*.

- Dever, M., D. Nicholson, M. M. Omand, and A. Mahadevan, Size-differentiated export in different dynamical regimes in the ocean, In revision, submitted to *Global Biogeochem. Cycles*.

- Omand, Melissa, Rama Govindarajan and Amala Mahadevan, A mechanistic model for the sinking flux of particles in the oceans, Submitted to Scientific Reports.

References

Zachary K Erickson. *Physical Processes Leading to Export of Fixed Carbon Out of the Surface Ocean*. PhD thesis, California Institute of Technology, 2019.

Zachary K Erickson and Andrew F Thompson. The seasonality of physically driven export at submesoscales in the northeast atlantic ocean. *Global Biogeochemical Cycles*, 32 (8):1144–1162, 2018.

Zachary K Erickson, Andrew F Thompson, Jörn Callies, Xiaolong Yu, Alberto Naveira Garabato, and Patrice Klein. The vertical structure of open-ocean submesoscale variability during a full seasonal cycle. *Journal of Physical Oceanography*, 2019.

Fabienne Gaillard. ISAS-13 temperature and salinity gridded fields. SEANOE., 2015.

Fabienne Gaillard, Thierry Reynaud, Virginie Thierry, Nicolas Kolodziejczyk, and Karina von Schuckmann. In situ-based reanalysis of the global ocean temperature and salinity with isas: Variability of the heat content and steric height. *Journal of Climate*, 29(4): 1305–1323, 2016. doi: 10.1175/JCLI-D-15-0028.1.

M.M. Omand, E.A. D'Asaro, C.M. Lee, M-J. Perry, N. Briggs, I. Cetinic, and A. Mahadevan. Eddy-driven subduction exports particulate organic carbon from the spring bloom. *Science*, 348(6231):222–225, 2015. doi: 10.1126/science.1260062.

N.A. Pelland, C.C. Eriksen, and M.F. Cronin. Seaglider surveys at Ocean Station Papa: Circulation and watermass properties in a meander of the North Pacific Current. *Journal of Geophysical Research: Oceans*, 121:6816–6846, 2016. doi: 10.1002/2016JC011920.

Noel Pelland. Seaglider Surveys at Ocean Station Papa: Bin-Averaged Profiles, Currents, and Independent Oxygen Data, 2018. URL `http://hdl.handle.net/1773/41656`.

Final Progress Report for:

Primary production changes across the Subarctic Atlantic: The physical and ecological roles of surface advection

NASA award NNX17AB99G (original) / 80NSSC18K0081 (current)

March 31, 2019 – December 31, 2020

Patricia Matrai, PI

Bigelow Laboratory for Ocean Sciences, 60 Bigelow Dr., East Boothbay, ME 04544

February 24, 2021

Participants

- P. Matrai (Bigelow: PI, project coordination, Arctic database, and data analysis)
- M. Vernet (SIO: co-I, physical-biological interactions)
- N. Mayot (Bigelow: Postdoctoral Research Scientist, data- model output (1-D, 3-D) comparisons)
- I. Ellingsen (SINTEF, Norway, unfunded Collaborator, SINMOD GCM)
- S. Bélanger (UQAR, Canada, unfunded Collaborator, custom processing of ocean color satellite imagery for Arctic waters)
- K. Richardson (Univ. Copenhagen, Denmark: unfunded co-PI, European field sea truth data products, interpretation of data-model output comparisons)
- P. Wassmann (Univ. Tromsø, Norway: unfunded co-I, zooplankton, interpretation of model outputs)

Objectives

Our main objective focused on the balance of net primary production (NetPP) in the Subarctic Atlantic as affected by (i) advective losses and gains within this region at large-scales interaction with respect to boundary conditions in the temperate N. Atlantic and Arctic Oceans; (ii) lateral and vertical "export" production within sub-regions of the Subarctic Atlantic at intermediate scales; and (iii) advective and local processes controlling NetPP in the Subarctic Atlantic region.

2020 Activities and Findings

Project Meetings: We have had multiple 2-way to 4-way video conference calls throughout the year.

Activities: Three manuscripts were published (Mayot et al. 2020, Ardyna et al. 2020, Wassmann et al. 2020), one manuscript was submitted, revised and is awaiting acceptance (Vernet et al. 2021a), and one manuscript is in preparation (Vernet et al. 2021b).

- A large-scale overview of annual net primary production rates (NPP) and their spatial variability in 7 regional shelves around Greenland (Fig. 1a) is done over the last decade (2008-2017), with special emphasis on spring bloom initiation. NPP is estimated by two independent approaches already established as best for estimating Arctic productivity: a regional, physically-biologically coupled, nested 3D ocean model (SINMOD) (Fig. 1b) and a spectrally-resolved, light-photosynthesis model of primary production applied to

satellite observations of phytoplankton biomass derived from ocean color remote sensing (OCRS, UQUAR-Takuvik model) (Fig. 1c). These two models were selected following the NASA-funded PPARR intercomparison for the Arctic Ocean (Lee et al. 2015, 2016).

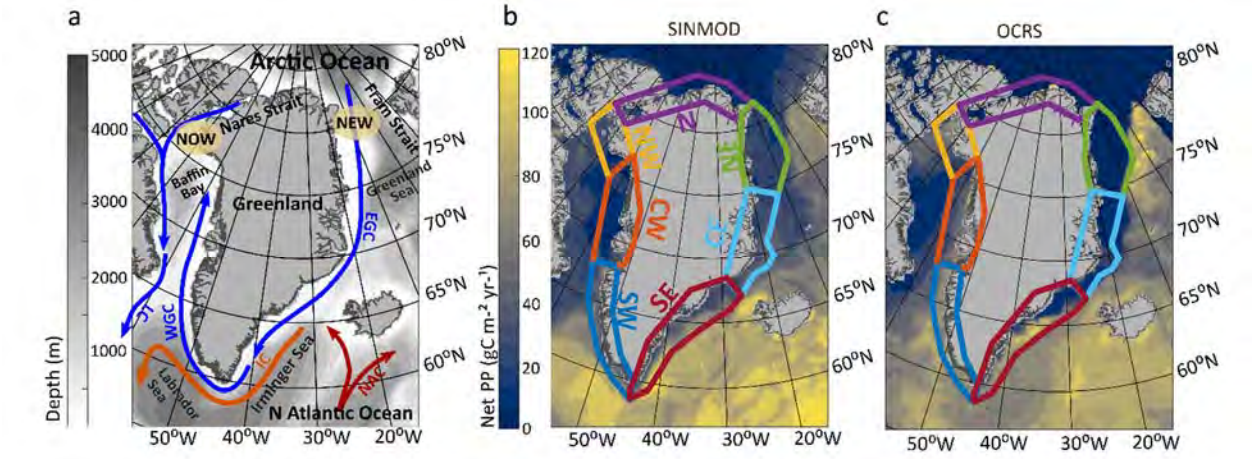

Figure 1 *– Study area and average productivity rates in the Greenland region and nearby seas. (a) The left panel describes major currents along the Greenland coast and the location of the NOW and NEW polynyas. Based on the NPP distribution in the coastal waters around Greenland and large geographical features, the shelf has been divided in 7 regions, as depicted in (b) and (c): counter-clockwise, SouthEast (**SE**), Central East (**CE**), NorthEast (**NE**), North (**N**), NorthWest (**NW**), Central West (**CW**) and SouthWest (**SW**). (b) Middle panel shows SINMOD-based NPP (g C m^{-2} yr^{-1}) for the year 2012, from a 365-day model output. (c) The right panel shows the average annual NPP for each sub-region for the year 2012 based on weekly estimates (n= 39 days) available for OCRS. Zero NPP_{OCRS} values may also represent no data available due to the presence of sea ice, especially further north.*

- Bloom initiation shows a strong south-north gradient, beginning in April in the southern regions and late June in the Arctic Ocean. OCRS-modeled NPP highlights the effect of sea ice presence on bloom initiation; this method depicts the start of the bloom consistently later, by up to 13 days on average, than SINMOD-modeled NPP estimates.
- Rates of annual NPP show a strong south-north gradient, with higher NPP rates observed in the North Atlantic water-influenced southern regions, with up to a factor of 3 decrease in NPP towards the north, in the western Eurasian Basin of the Arctic Ocean.
- Numerical modeling is able to detect early phytoplankton growth in Greenland shelves, particularly underneath seasonal sea ice. In each region, sea ice distribution and timing of formation and retreat affects location and timing of seasonal productivity with earlier and higher NPP offshore, moving inshore towards the summer (Fig. 2).
- An average 55% to 75% of the annual production is exported to depth, higher in Arctic and sub-Arctic regions, suggesting Greenland shelf waters have a potential for high carbon export to depth.

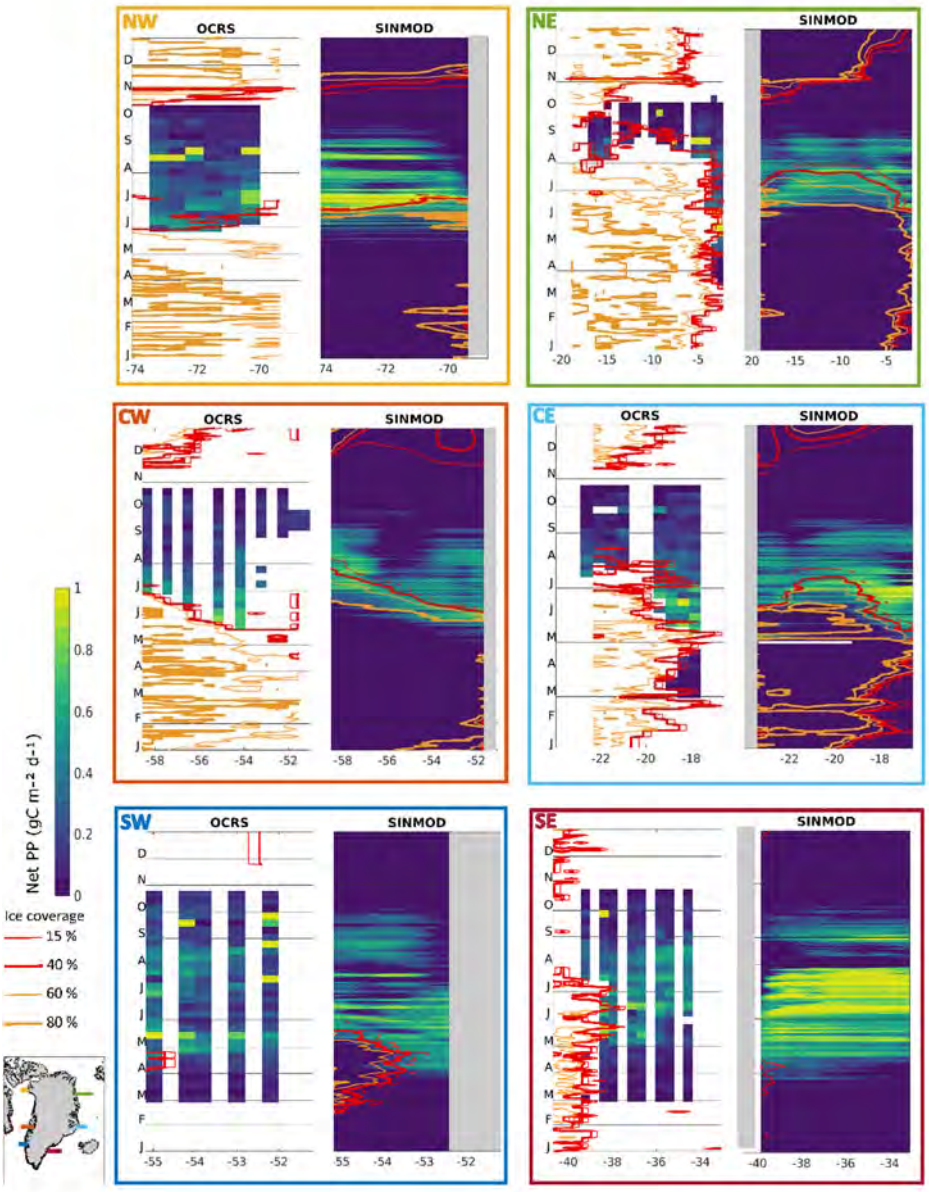

Figure 2 *– Seasonal NPP and sea ice concentration in six cross-shelf transects in eastern and western continental shelves of Greenland in 2017 (shown in far left). NPP rates from January to December estimated by SINMOD (right panel within each box) and NPP rates from January to December estimated by OCRS (left panel within each box) are shown in the North West (**NW**), North East (**NE**), Central West (**CW**), Central East (**CE**), South West (**SW**) and South East (**SE**) regions, respectively – Longitude is on the x-axes and Time, as months, on the y-axes. Color scheme depicts levels of NPP (0 to 1 g C m^{-2} d^{-1}) and isolines refer to sea ice concentration (from 0% to 100% concentration, as % ice cover that defines light penetration in the water column). The range of sea ice concentration is between 100% and 25% in OCRS, while the minimum sea ice concentration is 15%. Please note that the coast (grey bar) is on the right for the western regions and is on the left for the eastern regions. See Figure 1 for location identification.*

Data submitted: No new data were generated.

Manuscripts in preparation:

- Vernet, M., I. H. Ellingsen, C. Marchese, S. Bélanger, M. Cape and **P. A. Matrai**. "Net primary production and bloom initiation around Greenland". In review in Progress in Oceanography, September 2020, re-submitted February 2021 (based on SINMOD model runs and satellite-derived primary production data)
- Vernet, Eilertsen, Matrai et al. (2021b) – The focus is now on the southward East Greenland Current and its effect on local vs. advected primary production and interaction with nutrient inputs (or lack thereof) from the Arctic, the Greenland shelf, and the deep Greenland Sea. This modeling approach is similar to our publication in Frontiers in Marine Science (Vernet et al. 2019)

Next steps

- Manuscript preparation and publication (as listed above) will continue.

Presentations (Presenter underlined; postdocs and students bolded):

- COVID-19 resulted in the cancellation or postponement of all meetings where we planned to present, including Gordon Research Conference on Polar Oceans (Matrai, co-chair; initially March, then May, then cancelled) and 5th pan-Arctic Integration Symposium (Matrai and Vernet, invited speakers; Nov 2020, postponed).

Final Peer-Reviewed Manuscripts up to date (Postdocs and students bolded; PIs and Co-Is underlined):

- **Mayot, N.**, **A. Arjona**, S. Bélanger, **C. Marchese**, I. H. Ellingsen, T. Jaegler and P. Matrai. 2020. "Open-ocean phytoplankton production patterns associated with sea ice: A Greenland Sea analysis". J. Geophys. Res.-Oceans, 125, e2019JC015799. https://doi.org/10.1029/2019JC015799.
- Wassmann, P., Carmack, E.C., Bluhm, Duarte , B.A., Berge, J., Brown, K., Grebmeier, J.M., **Holding, J.**, Kosobokova, K., Kwok, R., Matrai, P., Agusti, S.R., Babin, M., Bhatt, U., Eicken, H., Polyakov, I., Rysgaard, S. and Huntington, H. "Towards a unifying pan-Arctic perspective: A conceptual modelling toolkit". Progress in Oceanography, 102455
- **Ardyna, M.**, C.J Mundy, **N. Mayot**, **L. Matthes**, **L. Oziel**, C. Horvat, E. Leu, P. Assmy, V. Hill, P. Matrai, M. Gale, I.A. Melnikov, K.R. Arrigo. "Under-ice phytoplankton blooms shedding light on the 'invisible' part of Arctic primary production?" Frontiers in Marine Science, | https://doi.org/10.3389/fmars.2020.608032.
- **Marchese, C.**, de la Guardia, L.C., Myers, P.G. and Bélanger, S. 2019. "Regional differences and inter-annual variability in the timing of surface phytoplankton blooms in the Labrador Sea". Ecological Indicators 96:81-90.
- Vernet, M., I. H. Ellingsen, L. Seuthe, D. Slagstad, **M. R. Cape**, P. A. Matrai, and P. Wassmann. 2019. "Importance of phytoplankton advection in the Atlantic Water Inflow to the Arctic Ocean", Frontiers in Marine Science, Research Topic Carbon Bridge to the Arctic, https://doi.org/10.3389/fmars.2019.00583.
- Valente, A., S. Sathyendranath, V. Brotas, S. Groom, M. Grant, M. Taberner, D. Antoine, R. Arnone, W.M. Balch, K. Barker, R. Barlow, S. Bélanger, J.-F. Berthon, Ş. Beşiktepe, Y. Borsheim, A. Bracher, V. Brando, E. Canuti, F. Chavez, A. Cianca, H. Claustre, L.

Clementson, R. Crout, R. Frouin, C. García-Soto, S.W. Gibb, R. Gould, S. Hooker, M. Kahru, M. Kampel, H. Klein, S. Kratzer, R. Kudela, J. Ledesma, H. Loisel, P. Matrai, D. McKee, B. G. Mitchell, T. Moisan, F. Muller-Karger, L. O'Dowd, M. Ondrusek, T. Platt, A.J. Poulton, M. Repecaud, T. Schroeder, T. Smyth, D. Smythe-Wright, H.M. Sosik, M. Twardowski, V. Vellucci, K. Voss, J. Werdell, M. Wernand, S. Wright, and G. Zibordi. 2019. A compilation of global bio-optical in situ data for ocean-colour satellite applications – Earth Syst. Sci. Data, 11, 1037–1068, https://doi.org/10.5194/essd-11-1037-2019.

- **Mayot, N.**, P. Matrai, M. Steele, K. Jonhson, S. C. Riser and D. Swift. 2018. "Assessing Phytoplankton Activities in the Seasonal Ice Zone of the Greenland Sea over an Annual Cycle". J. Geophys. Res.-Oceans 123:8004-8025. https://doi.org/10.1029/2018JC014271.

2019 Activities and Findings

Project Meetings: We have had multiple 2-way to 4-way video conference calls throughout the year.

Activities: One manuscript was published (Vernet et al. 2019), one manuscript was finalized and submitted (Mayot et al. in review), and three more are in preparation. Conclusions include:

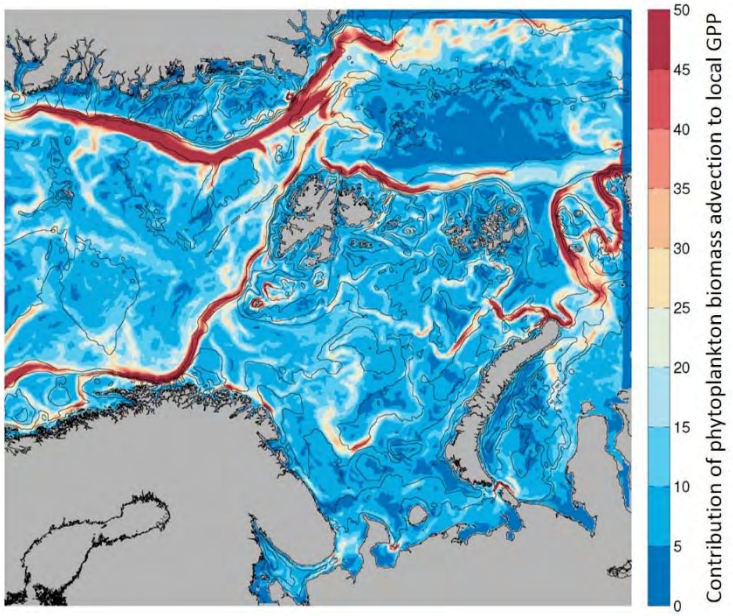

- Results from the regional, coupled physics – ice-biogeochemistry Arctic Ocean SINMOD GCM model show that changes in phytoplankton biomass at any one location along the Atlantic Water Inflow are supported primarily by advection (see left). This advection is 5-50 times higher than the biomass photosynthesized *in situ*, seasonally variable, with minimum contribution in June, at the time of maximum *in situ* production. Advection in the Norwegian Atlantic Current transports phytoplankton biomass from areas of higher production in the south, contributing to the maintenance of phytoplankton productivity further north. *In situ* productivity further decreases north of Svalbard Archipelago, at the entrance to the Arctic Ocean. Excess *in situ* annual production in the NW Svalbard Archipelago region is exported to the Arctic Ocean during the growth season (Vernet et al. 2019).

- The interannual variability (over 16 years) of the spring primary production in the open-ocean area of the Greenland Sea is directly linked to the presence or absence of sea ice exiting the

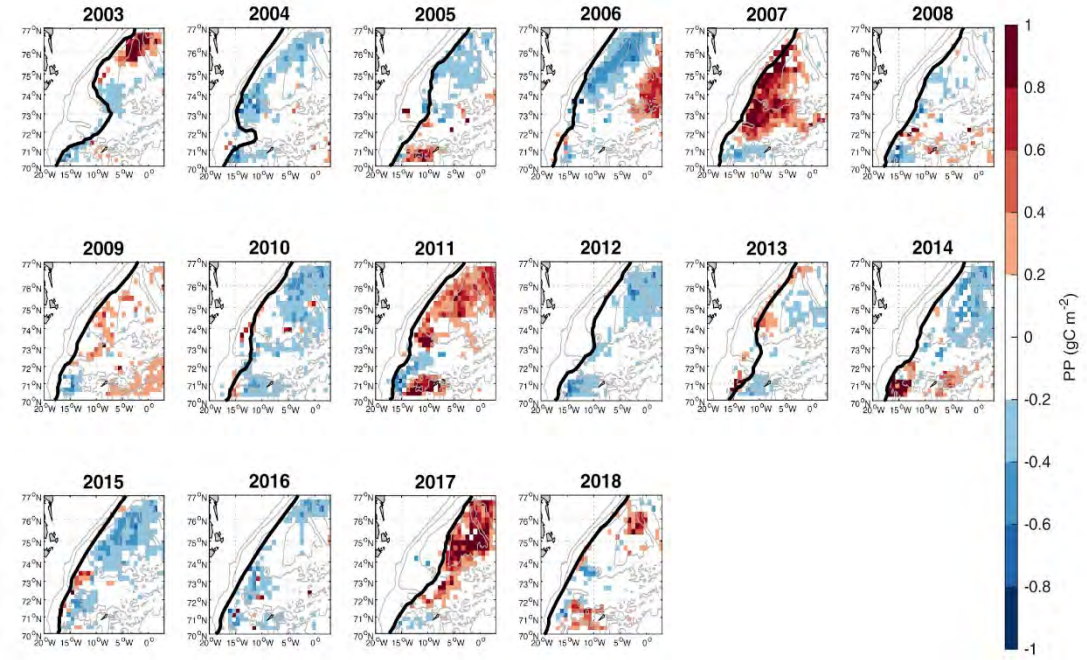

Anomaly of the daily primary production (PP) in spring for each year between 2003 and 2018. *The black line represents the location of the ice edge in April for each year studied. Data derived from MODIS composite imagery coupled with the Takuvik PP algorithm. (Mayot et al. in review)*

Arctic Ocean via Fram Strait. The magnitude of the sea ice flux determines whether thermal or haline stratification is the ultimate trigger for the onset and establishment of the phytoplankton spring bloom in Greenland basin per se, mainly in areas close to the seasonal ice zone (both under sea ice and in open water). Our results were next discussed within the framework of the Wassmann and Carmack (2006) conceptual model for alpha- and beta-oceans in sub-Arctic seas and the Arctic Ocean, with links to spring bloom mechanisms at lower latitudes in the North Atlantic Ocean. This exercise was based on runs of the Takuvik primary production (PP) algorithm optimized for the Arctic Ocean, with output provided by Arctus, Canada (http://arctus.ca/) as well as SINMOD model simulations provided by Sintef, Norway (https://www.sintef.no/en/) (Mayot et al., under review).

- Dr. Matrai participated in the NASA/NSF-funded workshop – "OCB Ocean-Atmosphere Interactions: Scoping directions for U.S. research" (The Woodlands, Sterling, VA), October 2019; https://web.whoi.edu/air-sea-workshop/

Data submitted:

- The Bio-ARGO data used in Mayot et al. (2018, in review) and being used in Vernet et al. (in prep 1 and 2) as well as by Marchese et al. (in prep) are already available at http://www.argo.ucsd.edu/Argo_data_and.html and are acknowledged in publications

- The satellite-derived primary production data for the Greenland Sea (2003-2018, as annual *.csv files) used in Mayot et al. (in review) has been deposited at NOAA NCEI, Submission Package Reference ID: B8UHE3 – Data set under review by NCEI, as "PRIMARY PRODUCTIVITY - PHYTOPLANKTON in Nordic Seas from 2003-03-06 to 2018-10-15"

Manuscripts in preparation:

- Marchese, Mayot, Bélanger, Matrai et al. – Multi-year variability in Labrador Sea primary production and controlling mechanisms (based on remote sensing data and primary production algorithm and Bio-Argo float data)

- Vernet, Eilertsen, Matrai, Marchese et al. (1) – Primary production patterns in the eastern Greenland Sea, Labrador Sea and Baffin Bay as a function of sea ice concentration (based on SINMOD model runs and satellite-derived primary production data)
- Vernet, Eilertsen, Matrai et al. (2) – The focus is now on the southward East Greenland Current and its effect on local vs. advected primary production and interaction with nutrient inputs (or lack thereof) from the Arctic, the Greenland shelf, and the deep Greenland Sea. This modeling approach is similar to our recent publication in Frontiers in Marine Science (Vernet et al. 2019)

Next steps

- Dr. Mayot will present results from his manuscript in review at the 2020 Ocean Sciences meeting in San Diego.

- Dr. Mayot's appointment at Bigelow Laboratory will end on Dec. 31, 2019. He will take a new position at the University of East Anglia, Norrich, UK in mid-January 2020 in Dr. Corinne LeQueré's group, with a focus on Earth System modeling coupled to remote sensing and in situ data. The Senior PIs of this NASA project are delighted with Dr. Mayot's professional progress.

- Manuscript preparation and publication (as listed above) will continue.

Presentations (Presenter underlined; postdocs and students bolded):

"Evidence for a link between the phytoplankton spring bloom in the Greenland Sea and Arctic sea ice export." Presentation with **N. Mayot**, P. Matrai, **A. Arjona**, S. Bélanger, T. Jaegler, **C. Marchese**, IOCS, March 2019, Busan, South Korea.

"Phytoplankton dynamics in the Greenland Sea." Presentation with **N. Mayot**, P. Matrai, Université Laval Conference, 5 April 2019, Quebec, Canada.

"Evidence for a link between the phytoplankton spring bloom in the Greenland Sea and Arctic sea ice export." Presentation with **N. Mayot**, P. Matrai, **A. Arjona**, S. Bélanger, T. Jaegler, **C. Marchese**, OCB summer workshop, June 24-28, 2019, Woods Hole, MA.

2018 Activities and Findings

Project Meetings: PI Matrai's field work schedule (~5 months in 2018), combined with the busy schedule of all participants, precluded an in-person meeting. Instead, we've had multiple 2-way to 4-way video conference calls throughout the year.

Activities: Three manuscripts were finalized and submitted. Two are published (Mayot et al. 2018, Marchese et al. 2019) and one is under review (Vernet et al. 2019). Conclusions include:

- Three phytoplankton activity phases were distinct within an annual cycle: one under ice, a second at the ice edge, and a third one around an open-water subsurface chlorophyll maximum (SCM). On average, most of the annual net community production occurred equally under ice and at the ice edge. The open-water SCM phase contribution, on the other hand, was much smaller. Phytoplankton biomass accumulation and production thus occur over a longer period

than might be assumed if under ice blooms were neglected. This also means that satellite-based estimates of phytoplankton biomass and production in this seasonal ice zone (SIZ) are likely underestimated. Simulations with the Arctic-based physical-biologically coupled SINMOD model suggest that most of the annual net community production in this SIZ results from local processes rather than due to advection (Mayot et al. 2018).

- A satellite time series of chl *a* in the Labrador Sea was combined with the GCM NEMO to determine the spring bloom timing: two neighboring but distinct bio-regional patterns were observed (above >60°N and below <60°N). The North blooms earlier and more intensely, while the south blooms later and lasts longer. The northern early onset of the spring bloom is related to the seasonal evolution (i.e., shoaling) of the mixed-layer depth and precedes the cessation of wintertime cooling. The southern delayed onset of the spring bloom tends to precede the shoaling of the mixed-layer depth and the vernal development of the upper ocean stratification. Hence, the physical heterogeneity of the Labrador basin requires physical-biological interactions to be examined regionally (Marchese et al. 2019).

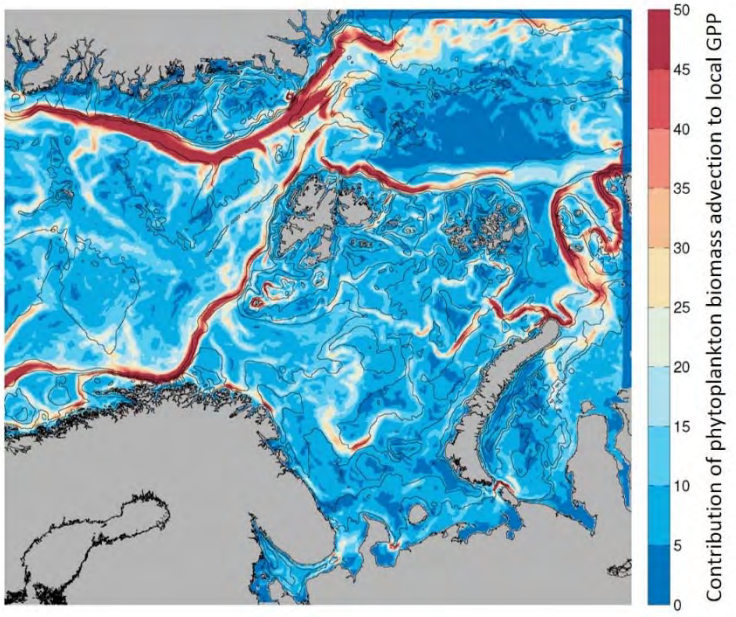

- The SINMOD model results show that changes in phytoplankton biomass at any one location along the Atlantic Water Inflow is supported primarily by advection (see left). This advection is 5-50 times higher than the biomass photosynthesized *in situ*, seasonally variable, with minimum contribution in June, at the time of maximum *in situ* production. Advection in the Norwegian Atlantic Current transports phytoplankton biomass from areas of higher production in the south, contributing to the maintenance of phytoplankton productivity further north. *In situ* productivity further decreases north of Svalbard Archipelago, at the entrance to the Arctic Ocean. Excess *in situ* annual production in the NW Svalbard Archipelago region is exported to the Arctic Ocean during the growth season (Vernet et al. 2019).

- Dr. Mayot is leading a 3rd manuscript, with results being presented at the 2019 ASLO Aquatic Sciences and the 2019 IOCCG meetings. The examination of the interannual variability (over 16 years) of the spring primary production in the open-ocean area of the Greenland Sea has led to the realization that the presence or absence of sea ice determines whether thermal or haline stratification is the ultimate trigger, which can next be compared to mechanisms at lower latitudes in the North Atlantic Ocean. This exercise was based on runs of the Takuvik primary production (PP) model for the Arctic Ocean, with output provided by Arctus, Canada (http://arctus.ca/).

- We hypothesize that the observed interannual variability in the Greenland basin is due to reduced export (or flux out) of Arctic sea ice in spring inducing a strong reduction of sea ice and

freshwater content in the Greenland basin per se, mainly in areas close to the SIZ, which further results in a weaker stratification of the water column. However, in contrary to the SIZ, for the deep basin an above-average Arctic sea ice export in spring did not necessarily lead to a strong and early phytoplankton spring bloom (e.g., 2008 and 2012).

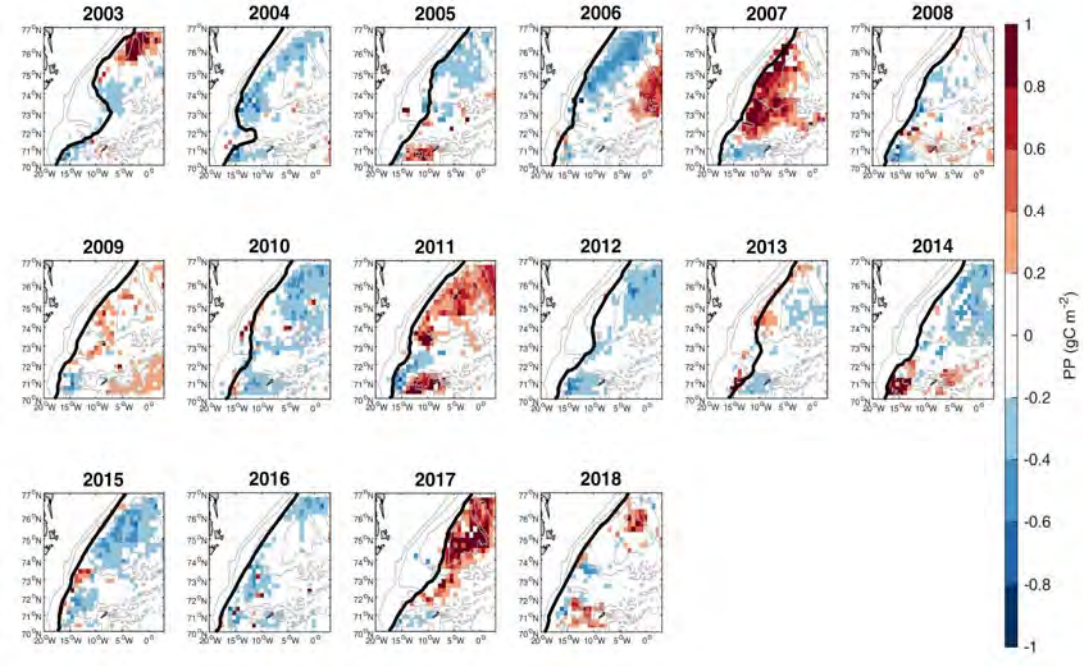

Anomaly of the daily primary production in spring for each year between 2003 and 2018. *The black line represents the location of the ice edge in April for each year studied. Data derived from MODIS composite imagery coupled with the Takuvik PP algorithm.*

Dr. Vernet is leading a 4th effort, using output from the biogeochemical GCM SINMOD, optimized for the Arctic Ocean, especially for the Atlantic-influenced side of the N. Atlantic (https://www.sintef.no/en/ocean/initiatives/sinmod/, led by I. Eilertsen). The focus is now on the southward East Greenland Current and its effect on local vs. advected primary production and interaction with nutrient inputs (or lack thereof) from the Arctic, the Greenland shelf, and the deep Greenland Sea.

Next steps

a. Dr. Mayot will present at the IOCCG meeting in Busan in April 2019, on behalf of our team.

b. Dr. Vernet will finish the effort to examine the effect of the southward advection of arctic waters on primary production of the sub-Arctic North Atlantic, with a modeling approach similar to our manuscript currently under review by Frontiers in Marine Science. Stratification, as mixed-layer depth, nitrate concentration and sea ice distribution are being considered in relation to advection, as main drivers. This modeling experiment will result in the following publication:

Vernet, M., I. H. Ellingsen, N. Mayot, M. R. Cape, D. Slagstad and P. A. Matrai 2019. "Contribution of advection to primary production in the Arctic Water Outflow to the sub-arctic Atlantic Ocean". In preparation for Global Biogeochemical Cycles.

c. Drs. Matrai and Mayot will focus on a 5th manuscript that can be finished by the end of calendar 2019, when the postdoctoral appointment will end.

d. Drs. Bélanger and Marchese will focus on the link between anomalous ocean physics and a massive spring phytoplankton bloom observed in the Labrador Sea in 2015 in relation to the available 2009-2018 time series. This effort will result in the following publication:

Yashayaev, I., C. Marchese, L. Oziel, Igor and S. Bélanger. 2019. "Anomalous mesoscale activity leads to a massive phytoplankton spring bloom in the Labrador Sea". In preparation for Can. J. Fisheries and Aquatic Sciences.

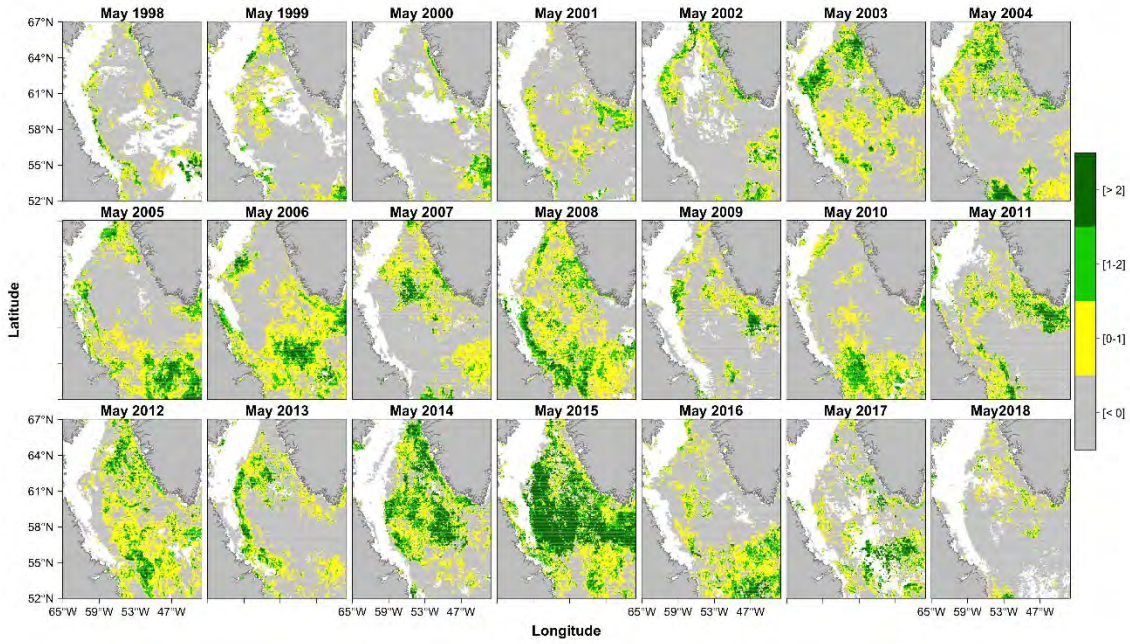

The figure above shows the standardized Chl a anomalies for the month of May (1998-2018) in the Labrador Sea (LS). Note that only positive values of Chl a (from GlobColour) are colored and binned into three classes. Grey areas represent negative values while white represents no data. Positive anomalies over the LS basin are only present in 2008, 2012,2014 and 2015.

Presentations (Presenter underlined; postdocs and students bolded):

"Assessing phytoplankton activities in the seasonal ice zone of the Greenland Sea over an annual cycle". Presentation with **N. Mayot**, P. Matrai, I. H. Ellingsen, M. Steele, K. Jonhson, S. C. Riser and D. Swift, OCB summer workshop, June 25-28, 2018, Woods Hole, MA.

"Arctic-COLORS (Arctic-COastal Land Ocean inteRactionS) Field Campaign Scoping Study Update and Plans". Presentation with A. Mannino, M. A. M. Friedrichs, P. Hernes, J. Salisbury II, M. Tzortziou, C. E. Del Castillo and Arctic-COLORS Team, A23G-1666 Fall AGU, December 10-14, Washington, D.C.

"Open-ocean phytoplankton production patterns associated with sea ice: A Greenland Sea analysis". Presentation with **N. Mayot**, P. Matrai, **A. Arjona**, S. Bélanger, **C. Marchese**, and T. Jaegler, ASLO Aquatic Sciences, Feb. 24- March 1, 2019, San Juan, PR.

"The role of sea ice extent on phytoplankton phenology in the Greenland Sea". Presentation with **A. Arjona**, **N. Mayot** and P. Matrai, ASLO Aquatic Sciences, Feb. 24- March 1, 2019, San Juan, PR.

2017 Activities and Findings

Postdoctoral Research Scientist Recruitment. Dr. Nicolas Mayot was hired by Bigelow Laboratory for Ocean Sciences for this project, starting early August 2017. He received his PhD in Oceanography from Villefranche Oceanographic Laboratory, under the direction of Drs. Fabrizio D'Ortenzio and Hervé Claustre.

First Project Meeting. Co-Is, Collaborators and Postdoc met at SINTEF, Trondheim, Norway in early August 2018 for our first joint workshop. The location allowed immediate preliminary model runs, as we set goals and priorities for the first 12 months.

Second partial Project Meeting. Collaborator Belanger and his soon-to-be postdoc Christian Marchese (UQAR), N. Mayot and I met in Quebec in Dec 2017 during the 2017 ArcticChange meeting to discuss timeline and a hierarchy of questions to be addressed in spring 2017.

Field Data Analyses. The focus of this year for Dr. Mayot was to take advantage of the biogeochemical Argo float data acquired in the Greenland Sea during a previous NASA-funded project. This data set provides the only continuous (weekly) data over four years (Jan-Dec 2012-2015), including winter, in the Greenland Sea in areas with and without sea ice, i.e., the bio-floats sampled under sea ice on a regular basis. The topography of the region fortunately allowed for one float to remain in more or less the same general location for two complete annual cycles while other floats sampled open waters during two additional annual cycles. The last year of data was transmitted once the last float resurfaced, months after being considered no longer active.

The currently accepted corrections for all biogeochemical ARGO float variables were applied to the original values, especially for oxygen concentration for which an atmospheric oxygen concentration correction has been developed.

A manuscript is in the final stages of preparation (see below) that focuses on primary production under sea ice and at the ice edge, compares field and ocean color (when available) values of chlorophyll, identifies and quantifies the relative magnitude of physical processes (i.e., vertical and horizontal advection/ transport) with assistance of a 1-D physical model (i.e., vertically/locally) and the SINMOD fully-coupled GCM (i.e., horizontally/regionally). We also identify and quantify the temporal variability of the annual cycle of net community production in the seasonal ice zone (i.e., using the NO_3^- fields measured by the floats) of this region.

Next steps

a. As we learned during our PPARR-Arctic project, modeled Arctic NetPP is most sensitive to the source of chl used and to the chl-primary production algorithm applied. Postdoc Mayot and P. Matrai have begun discussions with our Collaborator Simon Belanger and his new postdoc Dr. Christian Marchese on updating the Takuvik NPP algorithm for the Arctic (now just completed) and applying it to the Greenland and Labrador Seas. Both regions are strongly influenced by northward advection of Atlantic waters and southward advection of Arctic waters. Both regions also have sufficiently long field data sets to answer our proposed questions.

b. M. Vernet and graduate student Allison Lee from SIO will meet with co-I I. Ellingsen and Dr. Dag Slagstad (also SINTEF) to start discussions on how best to quantify the effect of advective and non-advective systems to the NetPP in the sub-Arctic Atlantic Ocean and the import/export of phytoplankton biomass, from/to the Arctic, similarly to the approach applied the advection of North Atlantic NetPP (manuscript in preparation; see below). The SINMOD GCM model will be

used to estimate the loss and gain terms at the boundaries as well as the internal physical, chemical, biological processes driving NetPP within the sub-Arctic N. Atlantic, with emphasis

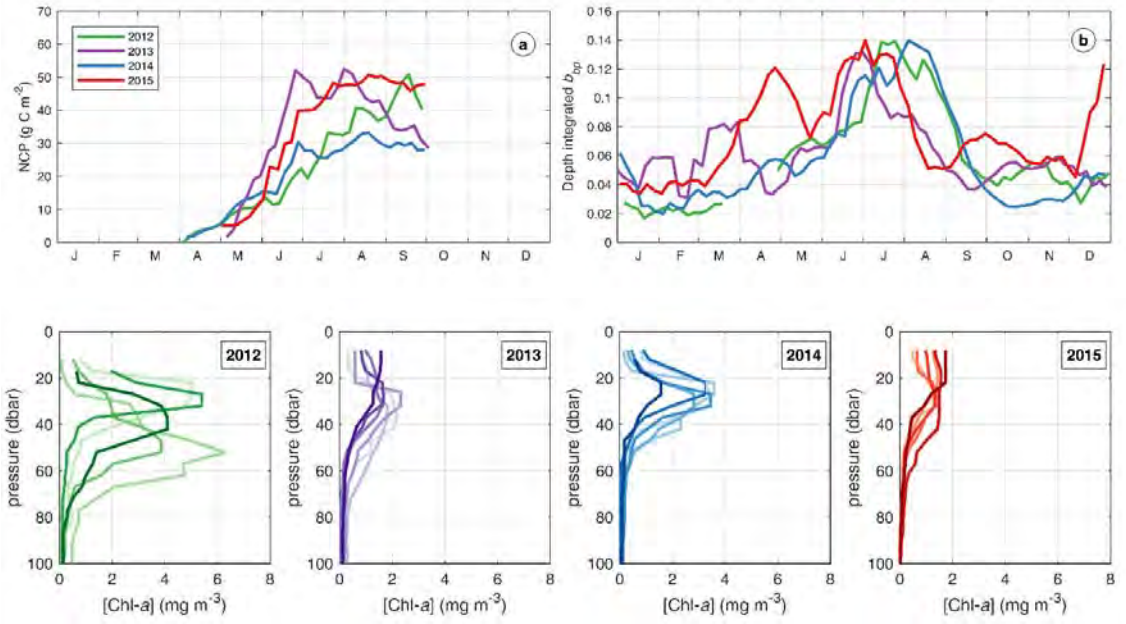

on advection, sea ice, nutrients and grazing/sedimentation.

Figure 1. Comparison between open-ocean and Seasonal Ice Zone areas. *(Top panels) Annual time series of Net Community Production (a) and surface-integrated b_{bp} (b), from 2012 to 2014. Time series were smoothed with a three points (i.e., 15 days) moving average. (Bottom panels) Vertical profiles of [Chl-a] measured during each of these four years in August, where the brightness encodes time (the darker, the later).*

Presentations:

"Spatiotemporal variabilities of phytoplankton activity in the Greenland Sea". Presentation with N. Mayot, P. Matrai, M. Steele, K. Johnson, S. Riser, D. Swift, ArcticNet Annual Scientific Meeting, December 12-14, Quebec City, QC, Canada.

"Contribution of advection to primary production in the Atlantic Water Inflow to the Arctic Ocean", M. Vernet, I. H. Ellingsen, L. Seuthe, D. Slagstad, M. R. Cape, P. A. Matrai, P. Wassmann, Invited Talk, Arctic Frontiers, 25-27 January 2017, Tromsø, Norway.

FINAL REPORT

Mechanisms controlling mesoscale/submesoscale hotspots in net community production/export, with simulation-based studies on how to sample them

NASA Grant No. NNX16AR50G
Period of Performance: 8/25/2016 to 8/24/2020

Dennis J. McGillicuddy, Jr.
Bigelow 209b – MS 11
Woods Hole Oceanographic Institution
Woods Hole, MA 02543
508-289-2683 phone
508-457-2194 fax
email: dmcgillicuddy@whoi.edu

November 18, 2020

The cornerstone contributions of this project are summarized in McGillicuddy et al. (2019) and Resplandy et al. (2019). In the former, we tested the Siegel et al. (2014) export flux model (EFM) using the output of a basin-scale coupled physical-biogeochemical model (CPBGCM). Our results indicate that there is tight correlation between the annual mean export flux simulated by the biogeochemical model and that predicted by the satellite-based algorithm driven by net primary production (NPP) from the model. Although the satellite-based approach performs well on the annual average, there are significant departures during the course of the year, particularly in spring. NPP and export flux can also become decoupled at the mesoscale, when the dynamics of fronts and eddies cause export to be displaced in space and/or time from the productivity event generating the particulate material. These findings have significant implications for the design of field studies aimed at reducing uncertainties in estimates of export flux.

Resplandy et al. (2019) investigated the effects of eddy-driven subduction on the biological pump. Estimates of the ocean biological carbon pump are limited by uncertainties in the magnitude of the physical injection of particulate and dissolved organic carbon to the ocean interior. A major challenge is to evaluate the contribution of these physical pumps at small spatial and temporal scales (<100 km and <1 month). We used a submesoscale permitting biophysical model covering a large domain representative of a subpolar and a subtropical gyre to quantify the impact of small-scale physical carbon pumps. The model successfully simulates intense eddy-driven subduction hot spots with a magnitude comparable to what has been observed in nature (1,000–6,000 mg $C \cdot m^{-2} \cdot day^{-1}$). These eddy-driven subduction events are able to transfer carbon below the mixed-layer, down to 500- to 1,000-m depth. However, they contribute <5% to the annual flux at the scale of the basin, due to strong compensation between upward and downward fluxes. The model also simulates hot spots of export associated with small-scale heterogeneity of the mixed layer, which intermittently export large amounts of suspended particulate and dissolved organic carbon. The mixed-layer pump contributes ∼20% to the annual flux. High-resolution measurements of export flux are needed to test models such as this one and to improve our mechanistic understanding of the biological pump and how it will respond to climate change.

Funding from this grant also facilitated the lead PIs participation in related studies of how mesoscale and submesoscale processes influence export. Barone et al. (2019) document variations in the ecological and biogeochemical state of the North Pacific Subtropical Gyre that relate to fluctuations in sea surface height (SSH). SSH is routinely measured from satellites and used to infer ocean currents, including eddies, that affect the distribution of organisms and substances in the ocean. SSH not only reflects the dynamics of the surface layer, but also is sensitive to the fluctuations of the main pycnocline; thus it is linked to events of nutrient upwelling. Beyond episodic upwelling events, it is not clear if and how SSH is linked to broader changes in the biogeochemical state of marine ecosystems. Our analysis of 23 years of satellite observations and biogeochemical measurements from the North Pacific Subtropical Gyre shows that SSH is associated with numerous biogeochemical changes in distinct layers of the water column. From the sea surface to the depth of the chlorophyll maximum, dissolved phosphorus and nitrogen enigmatically increase with SSH, enhancing the abundance of heterotrophic picoplankton. At the deep chlorophyll maximum, increases in SSH are associated with decreases in vertical gradients of inorganic nutrients, decreases in the abundance of eukaryotic phytoplankton, and increases in the abundance of prokaryotic phytoplankton. In waters below ∼100 m depth, increases in SSH are associated with increases in organic matter and decreases in

inorganic nutrients, consistent with predicted consequences of the vertical displacement of isopycnal layers. Our analysis highlights how satellite measurements of SSH can be used to infer the ecological and biogeochemical state of open-ocean ecosystems, and how this relates to export of organic material from the euphotic zone.

All of these studies note dependence of export flux on variations in the mixed layer. Gaube et al. (2019) demonstrate how mesoscale eddies modulate mixed layer depth on a global basis. Analysis of concurrent satellite observations of mesoscale eddies with hydrographic profiles by autonomous Argo floats reveals rich geographic and seasonal variability in the influence of eddies on mixed layer depth. Anticyclones deepen the mixed layer depth, whereas cyclones thin it, with the magnitude of these eddy-induced mixed layer depth anomalies being largest in winter. Eddy-centric composite averages reveal that the largest anomalies occur at the eddy center and decrease with distance from the center. Furthermore, the extent to which eddies modulate mixed layer depth is linearly related to the sea surface height amplitude of the eddies. Finally, large eddy-mediated mixed layer depth anomalies are more common in anticyclones when compared to cyclones. We present candidate mechanisms for this observed asymmetry and how this could impact biogeochemical cycling and export flux.

Song et al. (2020) quantify the impact of current-wind interaction on vertical processes in the Southern Ocean. Momentum input from westerly winds blowing over the Southern Ocean can be modulated by mesoscale surface currents and result in changes in large-scale ocean circulation. We used an eddy-resolving 1/20 degree ocean model configured near Drake Passage to evaluate the impact of current-wind interaction on vertical processes. We find a reduction in momentum input from the wind, reduced eddy kinetic energy, and a modification of Ekman pumping rates. Wind stress curl resulting from current-wind interaction leads to net upward motion, while the nonlinear Ekman pumping term associated with horizontal gradients of relative vorticity induces net downward motion. The spatially averaged mixed layer depth estimated using a density criteria is shoaled slightly by current-wind interaction. Current-wind interaction, on the other hand, enhances the stratification in the thermocline below the mixed layer. Such changes have the potential to alter biogeochemical processes including nutrient supply, biological productivity, export flux, and air-sea carbon dioxide exchange.

Publications resulting in whole or in part from this grant

Barone, B., Coenen, A.R., Beckett, S.J., McGillicuddy, D.J., Weitz, J.S., and D.M. Karl, 2019. The ecological and biogeochemical state of the North Pacific Subtropical Gyre is linked to sea surface height. *Journal of Marine Research*, 77, Supplement, 215–245, 2019, Volume of *The Sea*: The Current and Future Ocean.

Gaube, P., McGillicuddy, D.J., and A.J. Moulin, 2019. Mesoscale eddies modulate mixed layer depth globally. *Geophysical Research Letters*, 46. https://doi.org/10.1029/2018GL080006/

McGillicuddy, D.J., Resplandy L., and M. Lévy, 2019. Estimating particle export flux from satellite observations: Challenges associated with spatial and temporal decoupling of production and export. *Journal of Marine Research*, 77, Supplement, 247–258, 2019, Volume of *The Sea*: The Current and Future Ocean.

Resplandy, L., Lévy, M., and D.J. McGillicuddy, 2019. Effects of eddy-driven subduction on ocean biological carbon pump. *Global Biogeochemical Cycles*, 33, 1-14. https://doi.org/10.1029/2018GB006125.

Song, H., Marshall, J., McGillicuddy, D.J., and H. Seo, 2020. Impact of current-wind interaction on vertical processes in the Southern Ocean. *Journal of Geophysical Research: Oceans*, 125, 4, 1-14, https://doi.org/10.1029/2020JC016046.

Reference

Siegel, D. A., K. O. Buesseler, S. C. Doney, S. F. Sailley, M. J. Behrenfeld, and P. W. Boyd, 2014: Global assessment of ocean carbon export by combining satellite observations and food-web models. *Global Biogeochemical Cycles,* **28,** 181-196.

Observation-system simulation experiments (OSSEs) and seasonal forecasts to support EXPORTS

Cecile S. Rousseaux [1*], Lionel Arteaga[2,3] , Ivona Cetinić[4,1]

[1] Ocean Ecology Laboratory, NASA Goddard Space Flight Center, Greenbelt, Maryland, USA
[2] University of Maryland Baltimore County, Maryland, USA
[3] Global Modeling and Assimilation Office, NASA Goddard Space Flight Center, Greenbelt, Maryland, USA
[4] Morgan State University, Maryland, USA

1. Introduction

Oceans play an important role in the Earth's carbon cycle. The transport processes and pathways of carbon matter from the ocean's surface to the deep ocean directly affect the efficiency of carbon sequestration. Our current understanding of the fate of organic matter remains very limited and the uncertainties associated with the spatial and temporal patterns in carbon exports from the surface ocean remain very high (Siegel et al., 2014). As a direct result of this gap in knowledge, the EXPORTS field campaign was planned to "develop a predictive understanding of the export and fate of global primary production and its implications for the Earth's carbon cycle in present and future climates". EXPORTS integrates ship, autonomous robots, satellite observations and models to improve our predictive understanding of the export and fate of global ocean primary production and its implications for the Earth's carbon cycle.

Models have become more complex and now include a variety of mechanisms and variables that are not always measured directly from the field. The use of models combined with data assimilation allows for the integration of existing satellite data and provide global continuous data in the oceans, land and in the atmosphere. While models remain an approximation of the natural conditions, they can be particularly beneficial when designing and preparing field campaigns. The spatial and temporal representation of parameters of interest can provide information on their spatial and temporal magnitude and variability. Outputs of such modeling exercises can be used to target the specific suite of environmental, both ocean and atmosphere, conditions essential for the success of the field campaign. Furthermore, models can be used to test various sampling strategies through the use of Observing System Simulation Experiments (OSSEs). The objective of this project was to support the EXPORTS field campaign by (1) providing spatial and temporal magnitude of the variability of parameters involved in the carbon cycle and outlined by the EXPORTS Science Plan and (2) forecasting the short- and long-term physical and biogeochemical variability and fate of the carbon cycle. This was achieved by leveraging pre-existing capabilities and expertise developed at the NASA Global Modeling and Assimilation Office (GMAO) including an existing biogeochemical model (NASA Ocean Biogeochemical Model-NOBM), (2) the assimilation of satellite ocean color data and the use of satellite and reanalysis products (i.e., MERRA-2) to force the model and, (3) the use of an atmospheric and ocean 9-month forecast data. Hereafter we detail the findings from this project, how they were used in the context of EXPORTS as well as how these findings contributed to the improvement of the system used.

2. Spatial and temporal variability of parameters involved in the carbon cycle in the regions of interest for EXPORTS

At the beginning of the EXPORTS field campaign planning phase, the NOBM outputs were used to assess the spatial and temporal variability of various biogeochemical variables in the North Atlantic. The EXPORTS Science Team identified six potential stations and we provided information on the seasonal and interannual variability of various biogeochemical variables including phytoplankton composition and nutrient concentration at those stations to help them narrow down the best sampling strategies to effectively tackle their Science Questions. The results from this also highlighted some interesting pattern in the North Pacific Ocean and allowed us to provide a wider spatial and temporal context to the findings from the EXPORTS Project.

There is a clear seasonal variability in physical and biogeochemical conditions at station PAPA (50.1°N, 144.9°W). The deepest Mixed Layer Depth (MLD) is found in January after which it shallows until July. The shallowing of the MLD in January coincides with a decline in iron whereas nitrate concentration continues to increase until April. We found that this dynamic of deep MLDs in winter that shallow over the summer is characteristic of the whole North Pacific Ocean although the magnitude of the cycle is slightly more pronounced when averaging over the whole North Pacific Ocean. The seasonal variability of nitrate and iron at Station PAPA is also similar to those from the whole North Pacific although the concentrations are lower than the average for the North Pacific Ocean for both nitrate and iron. The assessment of the seasonal variability of physical and biogeochemical parameters at Station PAPA revealed the existence of a bimodal pattern in the primary production and export production (calculated at 200 m, Figure 1) that was related to a change in phytoplankton composition. This highlights the complex interactions between the production of chlorophyll in the surface water, the change in phytoplankton composition and the export of this production to deeper waters.

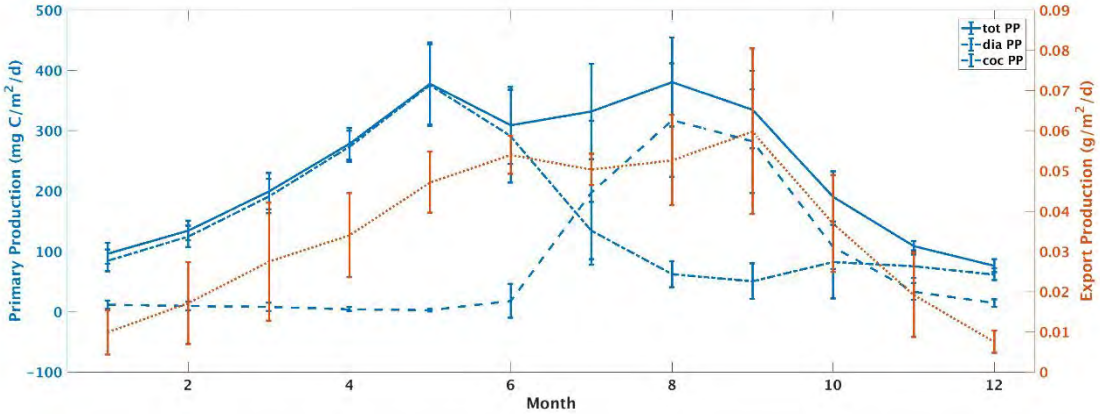

Figure 1: Seasonal variability of Primary Production (mg C m^{-2} d^{-1}, blue) and export production (g m^{-2} d^{-1}, orange) based on an average from 2012-2017. The error bars represent the standard deviation.

Chlorophyll concentrations vary by only 0.15 µg chl L^{-1} over the entire seasonal cycle (Figure 2). The maximum concentration is reached in September (0.35 µg chl L^{-1}). The phytoplankton community at station PAPA is dominated by diatoms, dinoflagellates and coccolithophores (Figure 2). Over the seasonal cycle, a succession is observed with diatoms dominating (>50% relative contribution) from November until June (maximum reached in May when they reach 0.25 µg chl L^{-1}, the equivalent of 98 % of the phytoplankton community). Dinoflagellates start to increase in

May and become dominant from July until October (maximum reached in July with 84% or 0.20 µg chl L^{-1}). Finally, coccolithophores reach their maximum concentration in August (0.05 µg chl L^{-1} or 16% of the phytoplankton community). Concentration of cyanobacteria, chlorophytes, and *Phaeocystis* spp. in this area are always <0.01 µg chl L^{-1}.

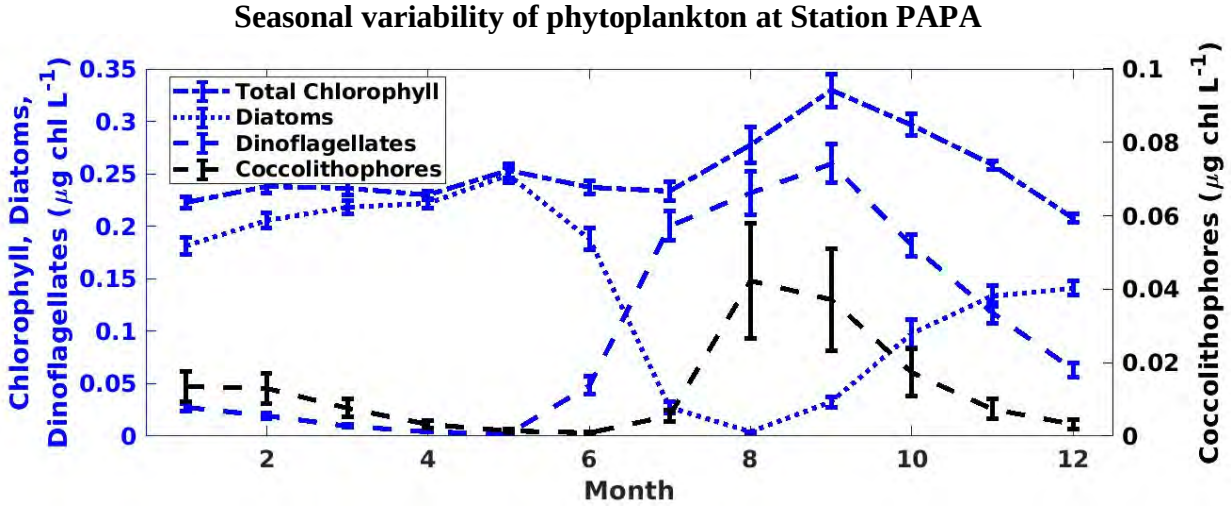

Figure 2: Seasonal variability of chlorophyll (µg chl L^{-1}, blue short dash), diatoms (µg chl L^{-1}, blue dotted), dinoflagellates (µg chl L^{-1}, blue long dash) and coccolithophores (µg chl L^{-1}, black long dash) based on an average from 2012-2018 for Station PAPA. The error bars represent the standard deviation. Cyanobacteria, chlorophytes, and Phaeocystis spp. are not represented since their concentrations was always <0.01 µg chl L^{-1}.

The seasonal variability of chlorophyll concentration at Station PAPA is quite different to the one observed for the North Pacific. In the North Pacific, instead of one maximum in September, there are two peaks: one in June reaching 0.46 µg chl L^{-1} and another smaller one in September (0.41 µg chl L^{-1}, Figure 3). There are however some similarities between Station PAPA and the rest of the North Pacific: the diatoms are the first group to increase and contribute considerably to the May-June peak (0.27 µg chl L^{-1} in May), their concentration declines afterwards (similarly to Station PAPA) but a second peak is observed in September (0.25 µg chl L^{-1}). Dinoflagellates follow a seasonal variability very similar to the one at Station PAPA where their concentrations increase from June onwards and reaches a maximum in September (although with a lower maximum, 0.13 µg chl L^{-1}). Finally, the overall concentration of coccolithophores at Station PAPA is higher than the average for the North Pacific but follows a similar seasonal cycle (with a maximum reached one month later: 0.05 µg chl L^{-1} in August instead of 0.006 µg chl L^{-1} in July in the North Pacific).

The export rates at Station PAPA oscillate between 10.2 mg C m^{-2} d^{-1} in December up to 151.8 mg C m^{-2} d^{-1} in August (Figure 4). The export rates within the North Pacific reach a maximum of 181.8 mg C m^{-2} d^{-1} two months earlier (June) than at Station PAPA but their rates remain above 150 mg C m^{-2} d^{-1} until the end of September after which they decline to reach rates comparable to Station PAPA in December and January. Primary production on the other hand has a biphasic signal with one first maximum (359.2 mg C m^{-2} d^{-1}) reached in May and another one (381.3 mg C m^{-2} d^{-1}) reached in August. In the North Pacific, the primary production reaches a maximum of 463.4 mg C m^{-2} d^{-1} in June and steadily decline until December when they reach a minimum of 76.1 mg C m^{-2} d^{-1}. Spatially, the export rates at Station PAPA appear comparable to

the rest of the North Pacific Ocean. Globally, upwelling regions as well as the North Indian and North Atlantic have relatively higher export rates than the North Pacific.

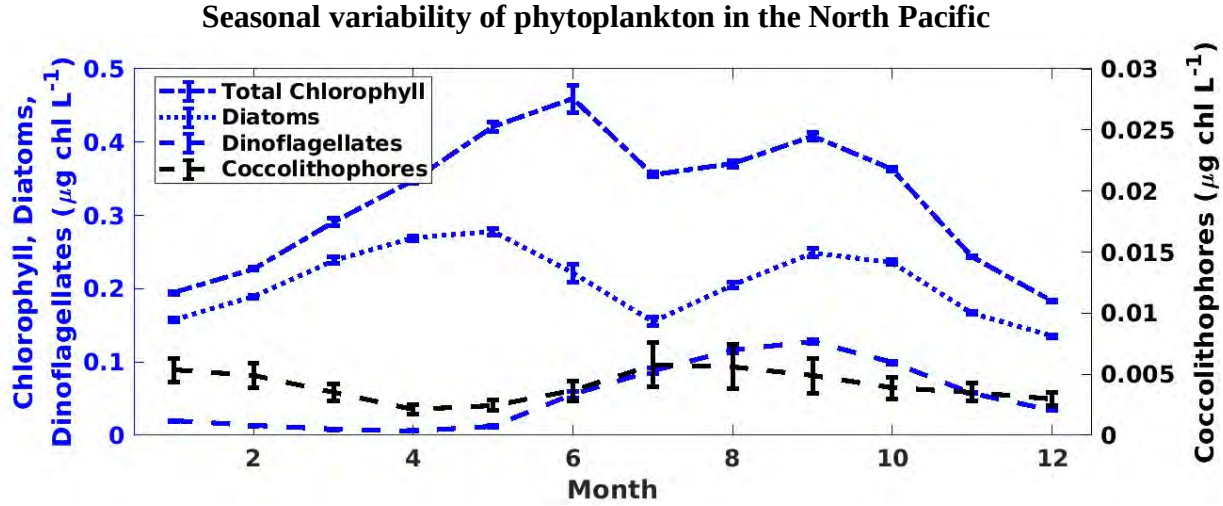

Figure 1: Seasonal variability of chlorophyll (µg chl L-1, blue short dash), diatoms (µg chl L-1, blue dotted), dinoflagellates (µg chl L-1, blue long dash) and coccolithophores (µg chl L-1, black long dash) based on an average from 2012-2018 for the North Pacific. The error bars represent the standard deviation. Cyanobacteria, chlorophytes, and Phaeocystis spp. are not represented since their concentrations was always <0.01 µg chl L^{-1}.

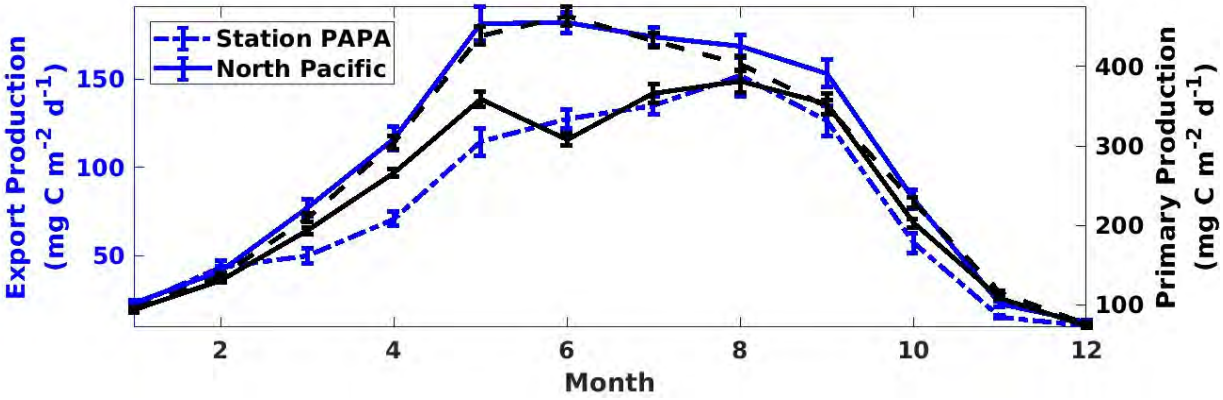

Figure 4: Seasonal variability of export production (mg m^{-2} d^{-1}) for Station PAPA and the North Pacific based on an average from 2012-2018. The error bars represent the standard deviation.

The primary focus was to estimate the impact of ecological diversity on carbon export rates, by quantifying the contribution of each phytoplankton group to the total production and export of organic carbon form the surface ocean to depth. NOBM output is intrinsically linked to remote sensing observations from space via the assimilation of satellite ocean color data. Chlorophyll (Chl) concentration has historically been considered the primary metric of phytoplankton biomass from space, which is why the NOBM is currently designed to provide Chl-based biomass estimates by accounting for variations in the cellular Chl:C ratio resulting from the photoacclimation state. Through this project we realized that this characteristic of the NOBM made the accurate estimation

of export rates in the model more difficult, since it is necessary to know depth-resolved carbon-based biomass estimates of each phytoplankton group to effectively compute their contribution of the total export production. This work highlighted this weakness in the model and ongoing work is aimed at updating the model saved output to facilitate the computation of export production from the different phytoplankton groups resolved by the model.

As part of this project, the analysis of the NOBM data in the North Pacific also highlighted some interesting patterns related to marine heatwaves and their effects on phytoplankton community composition in region. Marine heatwaves have become recurrent throughout the equatorial and northeastern Pacific Ocean during the last decade (2010s) and are associated with major deleterious environmental changes affecting the entire marine food chain. Recent studies have linked these ecological changes to decreased surface ocean chlorophyll levels, but a major missing component is how the anomalous warm events have affected the community composition of phytoplankton in the surface ocean. We used the NOBM outputs to describe changes in phytoplankton composition during the last decade's warm anomalies in the equatorial and northeastern Pacific Ocean. Our analysis revealed two periods of important changes in the partitioning of phytoplankton composition in the Gulf of Alaska (GOA), and the equatorial Pacific (ENSO 3.4 region). In GOA, reduced nutrient (silicate) supply led to a decrease in diatoms, permitting dinoflagellates to occupy a larger portion of the total stock in surface phytoplankton biomass. This switch in community composition prolonged an increase in surface chlorophyll concentration initiated since the beginning of the anomalous warm period in 2013 in this region. The second event was detected during the 2016 El Niño in the equatorial Pacific, where a major decline of ~ 40 % in surface chlorophyll was associated with a nearly total collapse in diatoms. We showed that in both cases, changes in community composition are triggered by alterations in wind-driven nutrient supply, related to "The Blob" warm anomaly in GOA, and to the extreme 2016 El Niño in the equatorial Pacific. Our results agree with observed phytoplankton community changes in GOA, where in situ field campaigns have been conducted during the anomalous warm period, and with historic biogeochemical patterns observed in the equatorial Pacific during El Niño events. We show that compound high-temperature and low-Chl events have become more frequent over the last twenty years in various regions of the Pacific Ocean and identify the predominant phytoplankton functional types under these emerging conditions, which might serve as a hint for how will surface ocean planktonic ecosystems evolve in a warmer future. These results have been summarized in a publication titled "Impact of Pacific Ocean heatwaves on phytoplankton community composition" and led by Lionel Arteaga that is currently being reviewed.

3. Forecasting system

We assessed the skills of the seasonal (9-month) forecast of chlorophyll concentration using the NOBM forced by the Global Modeling and Assimilation Office (GMAO) sub-seasonal to seasonal forecast system(GEOS-S2S, Molod et al., 2020). As a testbed for this we used the region of the Equatorial Pacific where we expect the skills of the model to be relatively good in forecasting interannual variability such as the El Niño event of 2015. The results from this validation were published in Rousseaux and Gregg (2017). We then focused on assessing the skills of the chlorophyll forecast in the northeast Pacific. This skill assessment revealed some limitations of the model including a bias in chlorophyll in the northeast Pacific. This led the initial condition of the forecast (produced by assimilating satellite ocean color) to return within days to the biased chlorophyll concentration of the free-run. The correction of this bias unveiled some interesting

observations about the challenges of forecasts for this region. The most important one being that the seasonal variability in this region was relatively small. It is more challenging to forecast a system that has little variability rather than one that has large-scale, atmospherically driven biogeochemical variability (e.g., Equatorial Pacific).

In 2019, we shifted our focus on assessing the skills of the seasonal forecast in the North and North Central Atlantic. In the North Atlantic (north of 40°N), we found that the spring bloom (peaks in May-June) reached higher chlorophyll concentration in the satellite data (Suomi-NPP) than in the free-run of the NASA Ocean Biogeochemical Model. This discrepancy could be the results of the bias introduced by missing data in the satellite dataset. In the North Central Atlantic (10-40°N) however, we observe the opposite. Here, the NOBM free-run has a positive bias during the annual chlorophyll peak in February/March for the period of study (2012-2016). The annual minimum chlorophyll occurs at the end of the summer and here the model seems to be underestimating the chlorophyll concentration at this time of the year. The chlorophyll concentration from the free-run model was found to be within 16 and 22% of the satellite data for the North Atlantic and within 4-19% for the North Central Atlantic. These are well within the semi-interquartile range of the Suomi-NPP versus in situ data (27.9%). The assimilation of chlorophyll further reduces the uncertainties and bias and provide initial conditions for the forecasting system.

We generated monthly retrospective forecasts for the period from January 2012 until December 2016 and assessed the skills of this forecasting system by comparing the forecasted chlorophyll concentration to those observed from Suomi-NPP. Note that these forecasts were generated by using initial conditions from a run that was forced using MERRA-2 and assimilated Suomi-NPP. Once the seasonal forecast starts, the assimilation is turned off and the MERRA-2 data are replaced by the seasonal forecast of several variables (from https://gmao.gsfc.nasa.gov/weather_prediction/) including: zonal and meridional wind stress, sea surface temperature and shortwave radiation. The skills of the various forecasts were assessed using three metrics: (1) the percent difference between the NPP-VIIRS chlorophyll data and the forecast (bias), (2) the anomaly correlation coefficient (ACC) and (3) the root mean square error (RMSE).We found that while the overestimate of the maximum peak and underestimate of the minimum peak for the North Central Atlantic was also observed in the forecasting system (Figure 2), the forecast of the North Atlantic chlorophyll agrees extremely well with the Suomi-NPP data (Figure 3). We found no obvious degradation of the forecast for longer lead time (as indicated by the ACC). ACC for the North Atlantic ranged between 0.76 (3-month lead forecast) to 0.82 (2-month lead forecast), while in the North Central Atlantic, the ACC ranged from 0.74 (8-month lead forecast) up to 0.86 (1-month lead forecast). These data indicate the potential for this system to be used in future field sampling design applications.

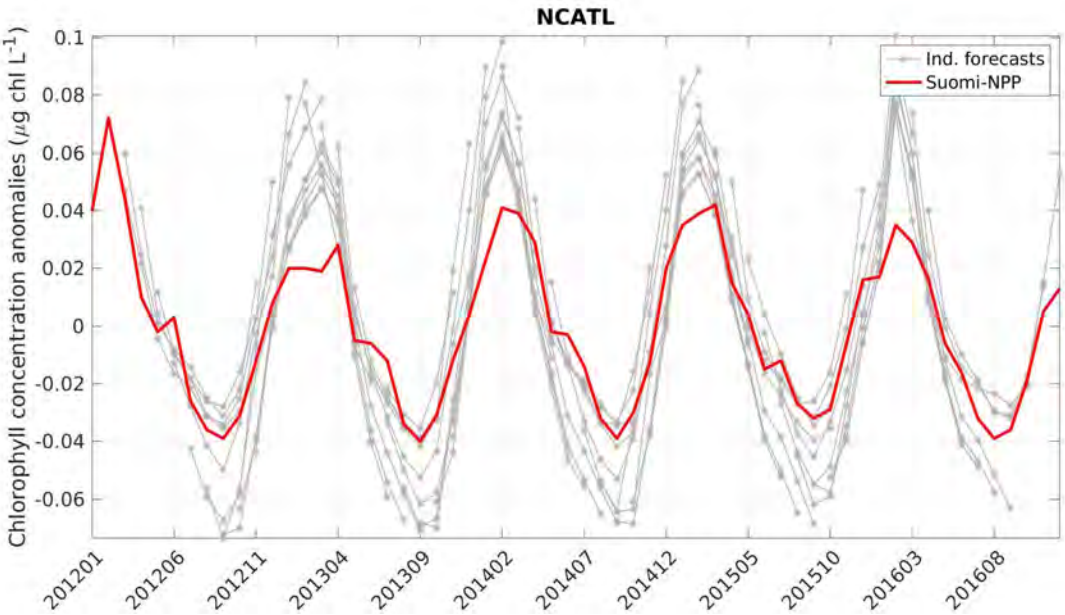

Figure 2: Chlorophyll concentration (μg chl L^{-1}) in the North Central Atlantic (10-40°N) from Suomi-NPP (red line) and the various 9-month forecast (grey lines) for the period from January 2012 until December 2016.

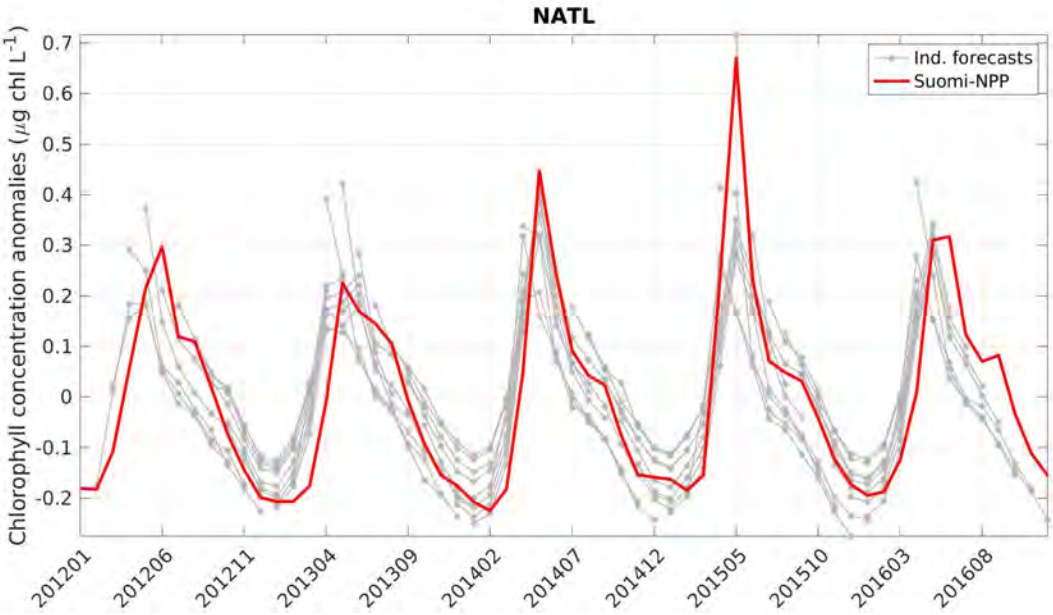

Figure 3: Chlorophyll concentration (μg chl L^{-1}) in the North Atlantic (40-71°N) from Suomi-NPP (red line) and the various 9-month forecast (grey lines) for the period from January 2012 until December 2016.

The skills assessment of this seasonal forecast was then extended to the other major oceanographic regions and the results were summarized in a publication titled "Assessing the skills of a seasonal forecast of chlorophyll in the global pelagic oceans" (Rousseaux et al., 2021). Chlorophyll concentration from the free-run were found to be significantly correlated to those from Suomi-NPP in all regions except the North Indian. Overall, the free-run was found to be able to simulate the right seasonal and interannual cycle but not always the right magnitude. The assimilation of ocean color data decreased uncertainties in all regions. This is important because

it means that the assimilation of ocean color data is improving the initial conditions used to the various seasonal forecast. We then assess the skills of 51 retrospective forecasts of chlorophyll concentration from February 2012 until December 2016 (Figure 4). The results showed significant Anomaly Correlation Coefficients (ACCs) for the majority of regions (11 out of the 12 regions for the 1-month lead forecast) including in the North and North Central Atlantic. The bias found in the system used to produce the seasonal forecast was found to impact directly the skills of the various forecasts and therefore suggest that a bias correction, potentially region-dependent, has the potential to considerably increase the skills of this global biogeochemical forecast. ACCs in both the North and North Central Atlantic ranged from 0.74 and 0.86 for all 9-month lead forecast and were all significant. While the chlorophyll concentration was underestimated in the North Atlantic (from -18.40% to -37.19%), it was overestimated in the North Central Atlantic (0.26% at lead month 3 up to 9.37% at lead month 9). The bias found in the system used to produce the seasonal forecast was found to impact directly the skills of the various forecasts and therefore suggest that a bias correction, potentially region-dependent, has the potential to considerably increase the skills of this global biogeochemical forecast. While further fine-tuning to the system is necessary, the system's skills show that such a biogeochemical forecasting system could be integrated in a fully coupled system, where the forecast of biogeochemistry can in turn affect other parameters, such as the temperature of the oceans. The system presented here has numerous applications once these improvements are made and could be beneficial to several societal applications.

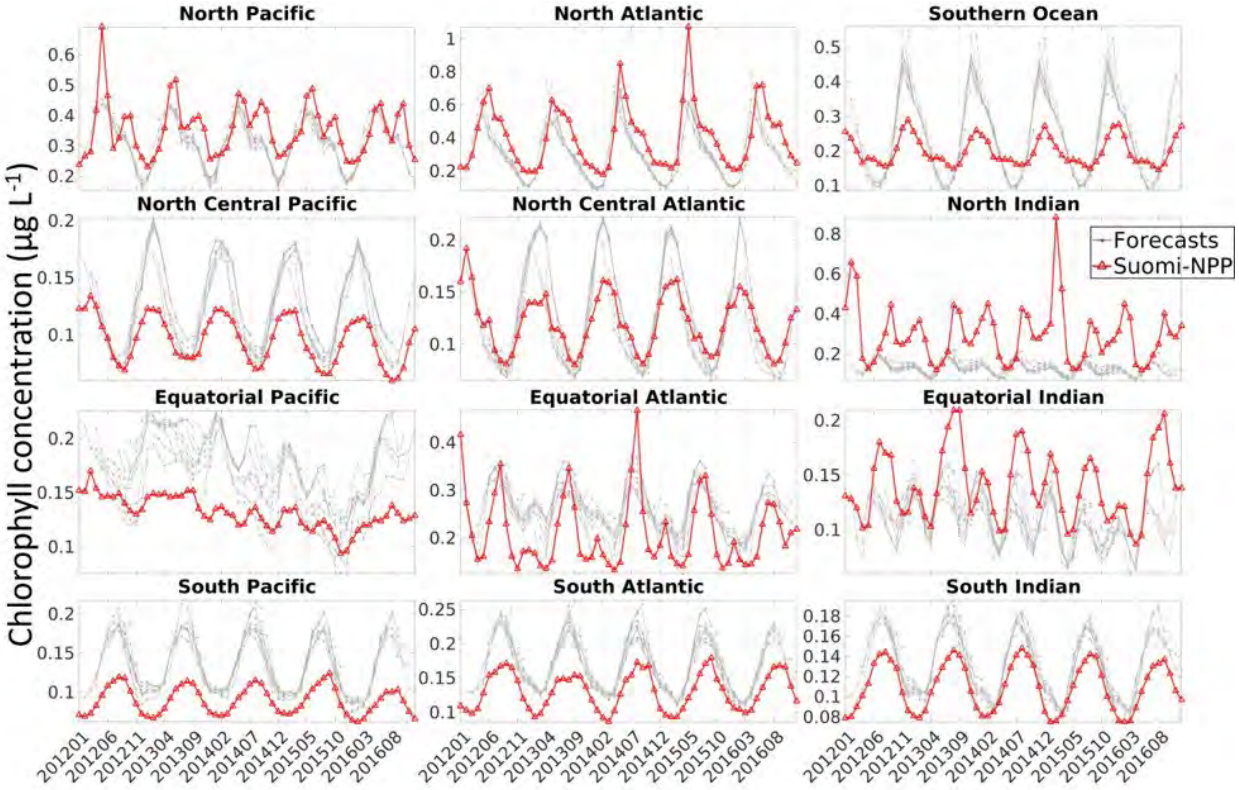

Figure 2: Chlorophyll concentration (µg L^{-1}) from the 51 different forecasts (grey lines), and Suomi-NPP chlorophyll (red triangle). Each of the 51 retrospective forecasts were run for a 9-month period. The first forecast started in February 2012 (initialized in January 2012) and the last forecast started in March 2016.

4. Dissemination of results

Publications:

- Arteaga, L. A. and Rousseaux C. 2022. “Impact of Pacific Ocean heatwaves on phytoplankton community composition.” Under review.
- Brewin, R. J., S. Sathyendranath, T. Platt, et al. 2021. "Sensing the ocean biological carbon pump from space: A review of capabilities, concepts, research gaps and future developments." *Earth-Science Reviews*, 103604 [10.1016/j.earscirev.2021.103604]
- Rousseaux C.S., Gregg W.W. & Ott L. 2021. Assessing the skills of a seasonal forecast of chlorophyll in the global pelagic oceans. Remote Sensing, 13(6), 1051; https://doi.org/10.3390/rs13061051
- Rousseaux C.S. & Gregg W.W. 2017. Forecasting Ocean Chlorophyll in the Equatorial Pacific. Frontiers in Marine Science , doi: 10.3389/fmars.2017.00236

Presentation:

- Arteaga L., and Rousseaux C. Impact of Pacific Ocean heatwaves on phytoplankton community composition. Remote oral presentation. Global Modeling and Assimilation Office Theme Meeting, Virtual, March 2022
- Arteaga L., and Rousseaux C. Impact of Pacific Ocean heatwaves on phytoplankton community composition. Remote oral presentation. European Space Agency (ESA) Ocean Carbon from Space Workshop, Virtual, February 2022.
- Rousseaux C.S., NOAA Ocean Color Coordinating Group (NOCCG) meeting, March 2021, Modeling global ocean biogeochemistry in support of field and satellite missions.
- Rousseaux C.S. “GMAO’s ocean biogeochemical model for planning NASA missions”, NASA GMAO research Theme Meeting. May 2019
- Rousseaux C.S. “Setting the seasonal context of export rates in the northeast Pacific using a biogeochemical model” EXPORTS Science Team meeting, May 2019.
- Rousseaux C.S. “Using a biogeochemical model in support of NASA missions” presented at NASA GMAO. May 2018.
- Rousseaux C.S. “Using an ocean biogeochemical model to support NASA’s EXPORTS field sampling mission”. NASA Global Modeling and Assimilation Office Core Review. May 2018
- Rousseaux C.S. “A modeling perspective on integrating satellite ocean color to derive carbon pools in the ocean”. USRA Board of Trustees Meeting, Columbia, MD, November 2016

5. References

Molod, A., Hackert, E., Vikhliaev, Y., Zhao, B., Barahona, D., Vernieres, G., Borovikov, A., Kovach, R.M., Marshak, J., Schubert, S., 2020. GEOS-S2S Version 2: The GMAO High-Resolution Coupled Model and Assimilation System for Seasonal Prediction. Journal of Geophysical Research: Atmospheres 125, e2019JD031767.

Rousseaux, C.S., Gregg, W.W., 2017. Forecasting Ocean Chlorophyll in the Equatorial Pacific. Frontiers in Marine Science 4. https://doi.org/10.3389/fmars.2017.00236

Rousseaux, C.S., Gregg, W.W., Ott, L., 2021. Assessing the Skills of a Seasonal Forecast of Chlorophyll in the Global Pelagic Oceans. Remote Sensing 13, 1051.

Siegel, D.A., Buesseler, K.O., Doney, S.C., Sailley, S.F., Behrenfeld, M.J., Boyd, P.W., 2014. Global assessment of ocean carbon export by combining satellite observations and food-web models. Global Biogeochemical Cycles 28, 181–196.

Annual Report: Data Mining Global Ocean Ecosystem & Carbon Cycling Observations for EXPORTS Planning & Synthesis

Principal Investigator: David A. Siegel – ERI / UCSB
Co-Investigator: Ken Buesseler – WHOI

Grant Number: NNX16AR49G

Period: August 25, 2018 to August 24, 2020

Project Goals and Objectives:

The biological carbon pump is thought to export ~10 Pg C each year from the surface ocean to ocean's interior largely in the form of settling organic particles. The monitoring and prediction of global carbon export and time scales for its sequestration remain important unknowns of the ocean's carbon cycle. To attack this problem, NASA is implementing the EXport Processes in the Ocean from RemoTe Sensing (EXPORTS) field campaign. The goal of EXPORTS is to gain a predictive understanding of the export and fates of global ocean net primary production (NPP). The EXPORTS Science Plan focuses on quantifying the pathways in which NPP is exported from the upper ocean and is sequestered at depth. The EXPORTS field campaign as planned will likely observe maybe eight distinct ecosystem / carbon cycling states; yet its plan is to answer its science questions by performing longitudinal analyses of observations made across a range of states. Unfortunately the statistical confidence in these results may be quite poor as only a small number of realizations may be afforded from the field program alone. The good news is that there are many sites where high quality ecosystem / carbon cycling observations are available from online repositories and literature accounts from previous and on-going research programs. Because of the available of these data, the "data mining" of available observations is an integral part of the EXPORTS Science Plan and likely critical to its success.

Here, we propose a pilot study to assess how to address the EXPORTS Science Questions by "data mining" previous observations. Specifically, our proposed objectives are to…

- Collect and collate available global ocean ecosystem and carbon cycling field observations useful for addressing the EXPORTS Science Questions,
- Construct EXPORTS data products and "wiring diagrams" from available data and distribute and publish them for their wide use, and
- Evaluate the use of the mined data products for assessing the EXPORTS Science Questions and developing advanced satellite algorithms and numerical models.

Although the geographic focus for the collection of useful data is global, an emphasis will be made for assembling data from the North Atlantic and Northeast Pacific sites that are the planned locations for the EXPORTS field campaign efforts. By completing the objectives of the proposed work, we will clearly contribute to the EXPORTS planning and risk reduction process conducted by the EXPORTS Science Team. In the following we will describe our progress made over the past year.

Research Activities:

Our data mining research worked along two parallel paths as was outlined in our proposal. The first path is the collection and use of global data sets for EXPORTS. This work couples to on-going research in our group on developing and validating novel satellite algorithms of ecosystem structure and carbon cycling. We worked on several questions relative to the EXPORTS. The first question was “Are more poorer quality biogeochemical observations more useful than much fewer higher quality observations?”. This was answered in Bisson et al. (2018) where we found that more poorer quality data did improve satellite export flux model performance. This assumption underlies the entire approach of the EXPORTS field campaign to develop a predictive understanding of the biological pump.

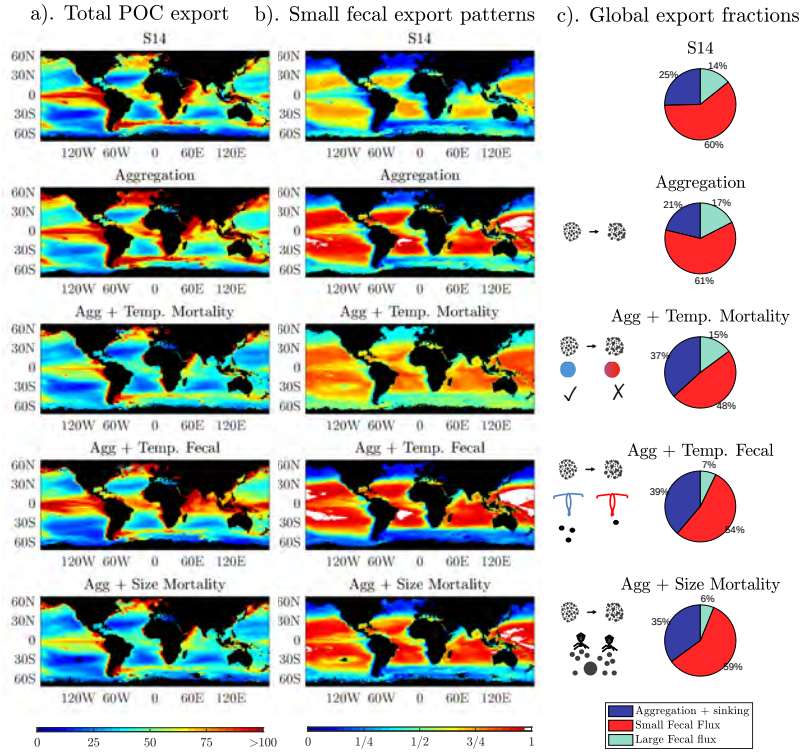

Figure 1: (A) Annually averaged total POC export (mg C m^{-2} d^{-1}). (B) Annually averaged contribution of small fecal flux to total POC export. (C) The fraction of annual average small fecal flux, large fecal flux, and aggregation and sinking flux to total flux for the 5 five models that incorporate phytoplankton size into their formulations. From Bisson et al. (2020).

Recently, we expanded the mechanisms included in the Siegel et al. (2014) satellite data driven POC export model to include the potential impacts of size-specific physical aggregation, size-specific and temperature-dependent zooplankton fecal pellet production, and size-specific and temperature-dependent non-grazing phytoplankton mortality (Bisson et al. 2020). We tested the different model configurations to determine if these processes improve the ability of the model to match the POC export observations from Bisson et al. (2018), and to assess the role of each process in controlling global POC export. We find that all model configurations predict that over 60% of the global POC export is from small zooplankton fecal pellets (Figure 1). All model

configurations predicted similar total POC export, and we find only small differences in the magnitude, timing, and geographical variations of total POC export. However, the fraction of total POC export due to sinking phytoplankton aggregates, and that due to the fecal pellets of large zooplankton, vary by more than a factor of two across the different model configurations. The POC export in all models is most sensitive to parameters controlling zooplankton fecal fluxes and non-grazing phytoplankton mortality. We compared zooplankton grazing rates predicted by the models to results of experimental data, and found that some models match the experimental grazing rates better than others, although data uncertainties remain large. More field measurements of bulk ecosystem rates (i.e., phytoplankton aggregation and zooplankton grazing), as well as explicit determinations of the proportion of fecal matter to phytoplankton aggregation, will help to better constrain mechanistic models of global POC export.

Another contribution supported by this award demonstrated the importance of metrics for assessing global sinking carbon export (Buesseler et al. 2020). Nearly all prior studies estimate sinking carbon export at a fixed depth fail because they do not consider the varying depth of light penetration, which ultimately controls production of sinking organic carbon and varies by location and season (Figure 2). The fixed depth approach introduces regional biases, and reduces global estimates of biological carbon pump fluxes by more than twofold. We advocate euphotic zone-based metrics to compare biological carbon pump efficiencies between sites which will lead to a better understanding of mechanisms that control carbon fluxes.

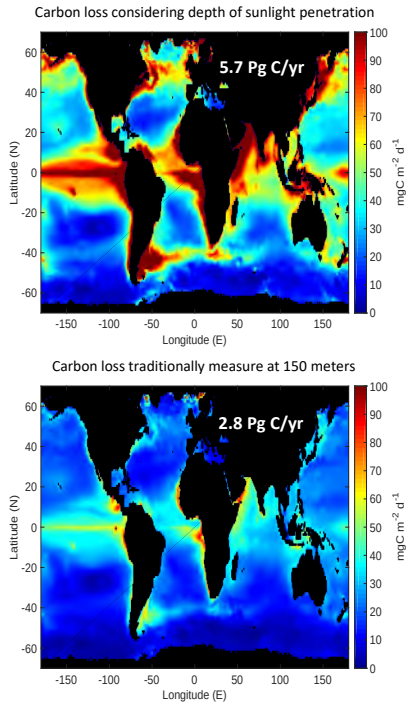

Figure 2: Comparison of the POC export fluxes from the satellite data-driven model of Siegel et al. (2014) evaluated at (upper) the depth of the 1% PAR isolume and lower) or at a depth of 150 m. From Buesseler et al. (2020).

Other global data synthesis studies we are conducting reviewing export pathways and fates for particle injection pumps (Boyd et al. 2019), modeling of the effects of zooplankton diel vertical

migration on carbon export and sequestration using satellite data (Archibald et al., 2019) and assessing the relative importance of export pathways (Nowicki et al. in prep.).

The second path for our data mining work is the construction of EXPORTS data products and "wiring diagrams" from well-studied sites – such as the Line P time series study, the Bermuda Atlantic Time Series (BATS), the Hawaii Ocean Time Series sites and the Porcupine Abyssal Plain (PAP) observatory. We have developed a database schema for an EXPORTS wiring diagram might look like and have started our initial populating of this schema using BATS and PAP data. This work is on-going. We have also focused on mining the Line P data set in support of the recent EXPORTS field program. Focus there is on the hydrographic, phytoplankton and zooplankton observations from the Canadian's three times a year survey to Station P site. These data have been provided to all EXPORTS PIs and were used extensively in planning for the field program. These data are also included in the logistics and operational overview paper from the 2018 Northeast Pacific EXPORTS field deployment (Siegel et al. in review). These data show a contrast from typical late-summer conditions for the 2018 EXPORTS field deployment with lower chlorophyll concentrations and deeper euphotic zone depths. Work is on-going assembling the same data for the PAP site, which will be location of the 2021 Northeast Atlantic EXPORTS field deployment.

Publications:

Archibald K., D.A. Siegel, and S.C. Doney, 2019, Modeling the impact of zooplankton diel vertical migration on the carbon export flux of the biological pump, *Global Biogeochemical Cycles*, **30**. https://doi.org/10.1029/2018GB005983.

Behrenfeld, M.J., Gaube, P., Della Penna, A., R. T. O'Malley, W.J. Burt, Y. Hu, P.S. Bontempi, D.K. Steinberg, E.S. Boss, D.A. Siegel, C.A. Hostetler, P.D. Tortell and S.C. Doney, 2019, Global satellite-observed daily vertical migrations of ocean animals. *Nature*, **576**, 257–261, https://doi.org/10.1038/s41586-019-1796-9.

Bisson, K.M., D.A. Siegel, T. DeVries, B.B. Cael and K.O. Buesseler, 2018, How data set characteristics influence ocean carbon export models. *Global Biogeochemical Cycles*, **32**. https://doi.org/10.1029/2018GB005934.

Bisson K, Siegel DA and DeVries T, 2020, Diagnosing mechanisms of ocean carbon export in a satellite-based food web model. *Frontiers in Marine Science*, **7:505**. doi: 10.3389/fmars.2020.00505.

Boyd, P.W., Claustre, H., Levy, M., Siegel, D.A. and Weber, T., 2019, Multi-faceted particle pumps drive carbon sequestration in the ocean. *Nature*, **568**, 327-335.

Buesseler, K.O., P.W. Boyd, E.E. Black, and D.A. Siegel, 2020, Metrics that matter for assessing the ocean biological carbon pump. *Proceedings of the National Academy of Sciences*, doi:10.1073/pnas.1918114117.

Cael B.B. and K. Bisson, 2018, Particle flux parameterizations: Quantitative and mechanistic similarities and differences. *Frontiers in Marine Science*, **5**, 395. doi: 10.3389/fmars.2018.00395.

Kramer, S. J., and D.A. Siegel, 2019, How can phytoplankton pigments be best used to characterize surface ocean phytoplankton groups for ocean color remote sensing algorithms?. *Journal of Geophysical Research: Oceans*, **124** doi:10.1029/2019JC015604.

Kramer, S.J., D.A. Siegel and J.R. Graff, 2020, Phytoplankton community composition determined from co-variability among phytoplankton pigments from the NAAMES field campaign. *Frontiers in Marine Science,* **7:215** doi: 10.3389/fmars.2020.00215.

Martin, A., P. Boyd, K. Buesseler, I. Cetinic, H, Claustre, S, Giering, S. Henson, X. Irigoien, I. Kriest, L. Memery, C. Robinson, G. Saba, R. Sanders, D. Siegel, M. Villa Alfageme and L. Guidi, 2020, The oceans' twilight zone must be studied now, before it is too late. *Nature,* **580**, 26-28.

Siegel, D.A., and many others, 2020, Overview of the EXport Processes in the Ocean from RemoTe Sensing (EXPORTS) Northeast Pacific Field Deployment. In review *Elementa*.

Presentations

Siegel, D.A., and I. Cetinić, 2018, The EXport Processes in the Ocean from RemoTe Sensing (EXPORTS) Northeast Pacific field campaign. Poster presented at the XXIV Ocean Optics Conference in Dubrovnik, Croatia, October 7-12, 2018.

Allen, J., and D. Siegel, 2018, Theoretical investigation of the use of the particulate backscattering spectrum to obtain the particle size distribution. Poster presented at the XXIV Ocean Optics Conference in Dubrovnik, Croatia, October 7-12, 2018.

Siegel, D.A., 2018, The biological carbon pump: how optical techniques can close the gaps. Town Hall Meeting convened at the XXIV Ocean Optics Conference in Dubrovnik, Croatia, October 7-12, 2018.

Hamme, R. and D. Siegel, 2018, Line P - EXPORTS Collaborations. Presented at the 2019 Line P Annual Meeting, Sydney, BC, April, 2018.

Kramer, S. J. and D. A. Siegel, 2019, Spatiotemporal distribution of five surface ocean phytoplankton communities determined from phytoplankton pigment composition on NAAMES 1-4. *Poster presentation at North Atlantic Aerosols and Marine Ecosystems Study (NAAMES) Science Team Meeting.* Washington, D.C. June 17, 2019.

Kramer, S. J. and D. A. Siegel, 2019, Phytoplankton community structure on NAAMES and EXPORTS determined from co-variability in phytoplankton pigment concentrations. *Poster presentation at EXport Processes in the Ocean from RemoTe Sensing (EXPORTS) Science Team Meeting. Williamsburg, VA.* May 8, 2019.

Please note that many other posters from this project were presented at this Williamsburg EXPORTS meeting and are not listed here.

Siegel, D.A., I. Cetinić and the EXPORTS Science Team, 2019, The EXPORTS Northeast Pacific Field Campaign. *Poster presentation at U.S. Ocean Carbon and Biogeochemistry.* Woods Hole, MA, June, 2019.

Siegel, D.A., I. Cetinić and the EXPORTS Science Team, 2019, Update on the EXPORTS Field Campaign. *Oral presentation at BIARRITZ Workshop.* Southampton, UK, July, 2019.

Siegel, D.A., 2019, Assessing mesopelagic ecological & biogeochemical processes by viewing from ~700 km above the Earth's surface. *Oral presentation at BIARRITZ Workshop.* Southampton, UK, July, 2019.

Siegel, D.A., 2020, Assessing mesopelagic ecological & biogeochemical processes by viewing from ~700 km above the Earth's surface. *Seminar for the Ocean Ecology Group at the NASA Goddard Space Flight Center.* Greenbelt, MD, February, 2020.

Kramer, SJ, D Siegel, (2020) Modeling Phytoplankton Pigments on Global to Local Scales Using Hyperspectral Optics. Presented at the Ocean Sciences Meeting, San Diego, CA, February 2020.

Buesseler, K., PW Boyd, S Henson, I Kriest, G Saba, D Siegel, and others, (2020). The Joint Exploration of the Twilight Zone Ocean Network (JETZON). Town Hall hosted at the Ocean Sciences Meeting, San Diego, CA, February 2020.

Nowicki, M.E., T. DeVries, D. Siegel, 2020, Quantifying global and regional carbon export and sequestration pathways with a data assimilation model of the biological pump. Presented at the Ocean Sciences Meeting, San Diego, CA, February 2020.

Siegel, D.A. and the EXPORTS Science Team, 2020, The EXport Processes in the Ocean from Remote Sensing (EXPORTS) Field Campaign: Results from the Northeast Pacific deployment and plans forward. Presented at the Ocean Sciences Meeting, San Diego, CA, February 2020.

Romanelli, E, SLC Giering, D Siegel, U Passow, 2020, Assessment of sinking particle size spectra from marine snow catcher deployments during EXPORTS. Presented at the Ocean Sciences Meeting, San Diego, CA, February 2020.

Siegel, D.A., 2020, Update on the EXport Processes in the Ocean from Remote Sensing (EXPORTS) Field Campaign. NASA Ocean Color Research Team (virtual) meeting, May 2020.